JOURNAL OF GEOPHYSICAL RESEARCH, VOL. 96, NO. D6, PAGES 10,809–10,845, JUNE 20, 1991

A Regional Model Study of the Ozone Budget in the Eastern United States

S. A. McKeen,[1] E.-Y. Hsie,[1] M. Trainer,[1] R. Tallamraju,[1] and S. C. Liu

Aeronomy Laboratory, Environmental Research Laboratories, National Oceanic and Atmospheric Administration, Boulder, Colorado

In order to better understand the photochemical and meteorological processes controlling regional scale air quality problems such as ozone formation, we have developed a three-dimensional Eulerian model and applied this model to a high-pressure period (July 4 to July 7, 1986) over the eastern United States. Meteorological and physical variables from a three-dimensional primitive-equation model are used to drive the transport parameters over a grid with 60x60 km^2 horizontal resolution, and 15 unequally spaced vertical layers extending from the ground to roughly 15 km. The treatment and incorporation of the dynamic model, the transport model, surface deposition, emission of anthropogenic and natural O_3 precursors, the chemical mechanism for 35 individual species, solar radiation and the numerical methods are discussed in detail. Model performance is tested by comparing model predicted O_3 concentrations with observations from the U.S. Environmental Protection Agency ozone-monitoring network. Although a significant correlation between model and observed O_3 is found, systematic discrepancies also exist and are discussed in relation to the basic model formulation, and variability in the observed O_3. Additionally, a comparison of time-averaged NO_x and anthropogenic nonmethane hydrocarbon (NMHC) concentrations to relatively long term observations provides a qualitative assessment of the model's ability to simulate certain aspects of these O_3 precursors from the few available observations. The model is used as a diagnostic tool to analyze various aspects of regional scale O_3 formation and the budgets of the primary O_3 precursors. Ozone formation over much of the continental model domain is shown to be NO_x limited. On the other hand, for midday NO_x levels greater than about 4 or 5 ppbv, O_3 formation is generally suppressed because of the low NMHC to NO_x ratios (1 to 7) that are characteristic of the emissions inventory. Regional-scale budget analyses show that very little NO_x or NMHC is transported to the free troposphere for the high-pressure conditions of this study and in the absence of a significant subgrid-scale vertical mixing process (i.e., efficient cumulus transport). We calculate a net turnover time of about 1.5 days for continental O_3 below 1800 m with in situ photochemical formation being balanced by photochemical loss and transport off the American continent. The results of this work are intended to serve as a baseline for further model development.

1. Introduction

Ozone is a key species in the tropospheric photochemistry. It is a prerequisite in the production of hydroxyl radicals [*Levy*, 1971], which control the chemical cycles of many reduced gases in the atmosphere [*Weinstock and Niki*, 1972; *Wofsy et al.*, 1972]. Without the presence of ozone, the amount of reduced gases in the troposphere would be substantially higher than their present concentrations. On the other hand, ozone is one of the major air pollutants that, in high concentration, can endanger health and damage plants [*National Academy of Sciences*, 1977; *Heck et al.*, 1982; *Reich and Amundson*, 1985]. In addition, because of its absorption of the infrared spectrum near 9.6 mm, ozone is an important greenhouse gas. Perturbation of tropospheric ozone, particularly in the upper troposphere, may have significant climatic effects [*Fishman et al.*, 1979*a*; *Wang and Sze*, 1980].

High concentrations of ozone are frequently observed over large rural areas in the industrial countries during the summer months, especially under high-pressure systems [*e.g. Cox et al.*, 1975; *Research Triangle Institute*, 1975; *Vukovich et al.*, 1977; *Guicherit and VanDop*, 1977]. Although there is a consensus that the high ozone concentrations are due primarily to anthropogenic activities [e.g., *Fehsenfeld et al.*, 1983], it is not clear quantitatively how much various sources contribute to the rural ozone. Potentially significant sources for rural ozone include photochemical production from anthropogenic and natural precursors and direct transport from the stratosphere. The precursors include NO_x, hydrocarbons, and CO. The emissions of these precursors are usually widely scattered. As a result, the distributions of the precursors display a high degree of variability over space and time [e.g., *Logan*, 1983; *Fehsenfeld et al.*, 1988]. Since ozone production depends strongly on the distributions of the precursors and the relationship between ozone production and concentrations of precursors is highly nonlinear [*Dodge*, 1977; *Hov and Derwent*, 1981; *Liu et al.*, 1987], it is necessary to include realistic transport processes to evaluate the budget and distribution of ozone.

There have been several three-dimensional modeling efforts to include adequate transport and photochemical processes in studying rural ozone buildup and other regional pollution problems such as acid deposition [*Lamb*, 1983; *Liu et al.*, 1984; *Chang et al.*, 1987]. With a three layer model, *Liu et al.* [1984] were able to get a reasonably good agreement between calculated O_3 concentrations and observed values of the Sulfate Regional Experiment (SURE) project in the eastern United States [*Mueller and Watson*, 1982]. However, comparisons of calculated and observed values of NO_2, NO, and SO_2 were not satisfactory. They attributed the discrepancy to the short lifetimes of these species and the limited spatial resolution of the model.

In order to study the photochemistry of rural ozone and transformation of acid precursors such as NO_x and SO_2, we have developed a three-dimensional regional air quality model. The model consists of two major components: the mesoscale meteorological module (MM4) and the air quality module. The general approach used in our model is similar to that of the regional acid deposition model (RADM) developed by the National Center for Atmospheric Research (NCAR) [*Chang et al.*, 1987].

[1]Also at Cooperative Institute for Research in Environmental Sciences, University of Colorado, Boulder.

Paper number 91JD00052.
0148-0227/91/91JD-00052$05.00

In the following sections, we first describe the structure of the model, the numerical methods, emission inventory, photochemical scheme and the boundary conditions assumed. We then present a model study of the rural ozone buildup during a high-pressure period (July 4 to 7, 1986) in the eastern United States. This period was chosen because the clear sky and stagnant conditions were conducive to photochemical production of O_3, providing an excellent opportunity to study the photochemistry and transport of O_3 and its precursors.

We will compare the O_3 levels calculated by the model to those observed by the U.S. Environmental Protection Agency (EPA) ozone network [*U.S. EPA*, 1987]. Comparison of the distributions of O_3 precursors calculated by the model, i.e., NO_x and nonmethane hydrocarbons (NMHC), to observed values can provide an important test of the photochemical and transport processes in the model. Unfortunately, there are few reliable measurements of NO_x and NMHC over the rural areas of the eastern United States. Measurements in urban centers are not useful for comparison with the model because of the coarse resolution (60×60 km^2). Finally, an analysis of midday photochemical O_3 formation and the regional-scale budgets of O_3 and its precursors are presented as illustrations of the resulting photochemical conditions determined by the air quality model and the most recent National Acid Precipitation Assessment Program (NAPAP) emissions inventory.

In addition, an extensive data base of O_3, NO_x, HNO_3, peroxyacetyl nitrate (PAN), natural and anthropogenic NMHC, and other related species was obtained at a rural site (Scotia, Pennsylvania) during this period. This allows a detailed examination of the photochemical processes that govern the relationships between O_3, its precursors, and other key photochemical species. A companion paper (M. Trainer et al., manuscript in preparation, 1991) will address this subject in detail. The present study will focus on the regional aspect of O_3 and its precursors.

2. Model Description

The model system (Figure 1) contains two major components: the dynamic and air quality models. The air quality model then consists of two components: a transport model and a photochemical model. Following *Chang et al.* [1987], the dynamic model is run off-line, and generates meteorological and physical variables that are used as input for the other 2 components. This section describes the treatment of various processes within each model component, and how the predictive equations are solved.

2.1. *The Dynamic Model*

2.1.1. *The Penn State/NCAR mesoscale model (MM4) system.* This dynamic model is a three-dimensional, hydrostatic, compressible, primitive-equation model [*Anthes et al.*, 1987]. The vertical coordinate of the model is the terrain-following sigma coordinate

$$\sigma = \frac{p - p_t}{p^*} \tag{1}$$

where $p^* = (p_s - p_t)$, p is the pressure at the σ level, p_s is surface pressure, and p_t is the pressure at the top of the model atmosphere (100 mbar). The prognostic and diagnostic variables of the dynamic model are listed in Table 1. The model domain is shown in Figures 2*a* through 2*c*, and covers the eastern part of the United States. There are 48 grid cells in the east-west direction and 36 in the north-south direction, corresponding to 60×60 km^2 grid resolution on a Lambert conformal map projection. The model has 15 vertical layers, and a Blackadar planetary boundary layer (PBL) parameterization [*Zhang and Anthes*, 1982] is used in the simulations. Half of the vertical layers are concentrated in the lowest 2 km of the model atmosphere in order to resolve the PBL (Table 2). The explicit moisture scheme of *Hsie et al.* [1984] is used to calculate the moisture cycle, which is necessary for cloud water and rainwater forecasts and the photolysis rate computations discussed in section 2.3.3. Results from the dynamic model are saved for incorporation into the chemical and transport models every 30 min.

TABLE 1. Meteorological Data Generated by the Dynamic Model

Variable	Definition
	Prognostic Variables
u	east-west component of velocity
v	north-south component of velocity
T	temperature
q_v	water vapor mixing ratio
q_c	cloud water mixing ratio
q_r	rain water mixing ratio
p^*	surface pressure minus 100 mbar
T_g	ground temperature
	Diagnostic Variables
$\dot{\sigma}$	vertical velocity in σ coordinate
K_H	horizontal diffusion coefficients
K_Z	vertical diffusion coefficients
m_z	mixing coefficients
R_T	total rainfall
h	PBL height
K_{PBL}	level of PBL
u^*	frictional velocity
H_o	sensible heat fluxes
E_o	Latent heat fluxes
Ancillary Data Common to Dynamic, Chemical and Transport Modules	
z	terrain height
L_u	land use categories
m_x	mapscale factor at concentration points
m_d	mapscale factor at velocity points
f	coriolis parameters
ϕ	latitude of the grid points
λ	longitude of the grid points

TABLE 2. Vertical Structure of the Three-Dimensional Model

Full σ Levels	Half σ Levels	Thickness,* m	Height,* m	Pressure,† mbar
0.0	0.05	4100	13840	145
0.1	0.15	2574	10681	235
0.2	0.25	1895	8538	325
0.3	0.35	1552	6833	415
0.4	0.45	1323	5406	505
0.5	0.55	1157	4172	595
0.6	0.65	1033	3081	685
0.7	0.74	754	2193	766
0.78	0.81	531	1555	829
0.84	0.865	422	1080	878
0.89	0.91	325	707	919
0.93	0.945	237	426	950
0.96	0.97	155	230	973
0.98	0.985	77	115	986
0.99	0.995	76	38	995
1.0				

*Based on U.S. Standard Atmosphere (1976).
†Assumed surface pressure of 1000 mbar.

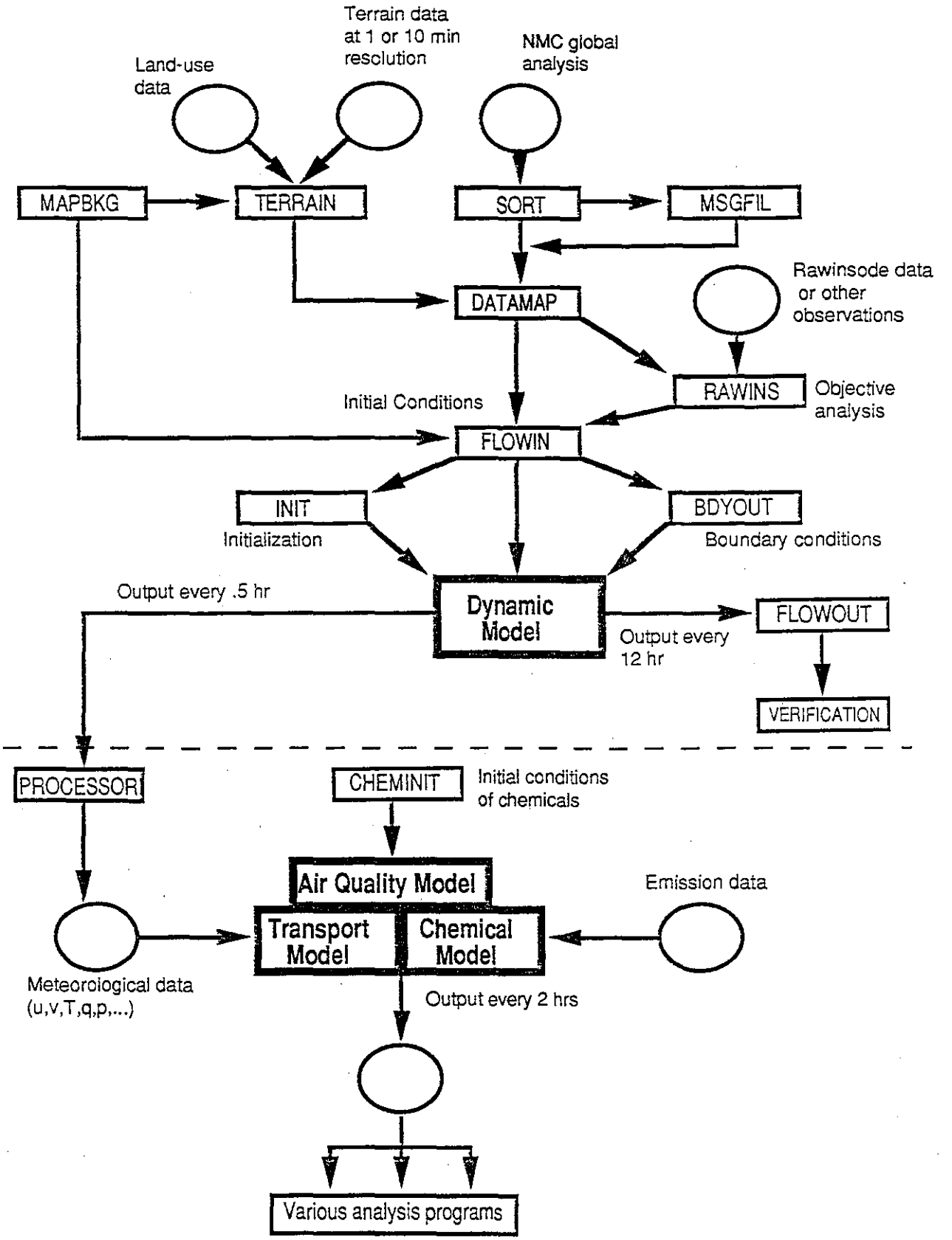

Fig. 1. Schematic structure of the model system. Major modules are heavily outlined.

2.1.2. *Synoptic discussion and model simulation.* We have chosen a particular 4-day period (July 4-7, 1986) to correspond with a field experiment conducted by the NOAA Aeronomy Laboratory at Scotia, Pennsylvania, for which high (>100 ppbv) O_3 concentrations were observed. The initial and boundary conditions were interpolated from National Meteorological Center (NMC) analysis with a successive correction technique and enhanced with rawinsonde data.

The synoptic scale conditions for the model initial time (00 UT, July 4, 1986) are dominated by a high-pressure system (1019 mbar) centered in western Pennsylvania, which moves slowly toward the south-southeast. The main areas of precipitation are associated with a cold front from a low-pressure system in the Atlantic Ocean, which passes the eastern seaboard on the previous few days, and extends through the Florida peninsula. Another low-pressure system is located in the southern Canada and Dakota areas to the west of the model domain. The low-pressure system over Canada eventually intensifies (center pressure reaching 985 mbar at 12 UT, July 6, 1986) and moves toward the north-northeast. The major precipitating areas in the simulation period are around the fronts associated with this developing low and located to the north of Pennsylvania, as well as on the southern rim of the high-pressure system which brings moist air from the Atlantic into the Carolina region. During the simulation period, the eastern United States is either dominated by the high-pressure system or located in the warm sector of the low-pressure system in Canada. On the last day (July 7, 1986), a short wave passes through the east coast, but no significant weather is associated with this wave. At the end of the simulation period (00 UT, July 8, 1986) the frontal system extends from the northeastern United States, through the Great Lakes, Wisconsin, and Missouri toward the Texas panhandle. The southeastern United States is still controlled by the high-pressure system just off the east coast.

Figures 2*a* and 2*b* show the simulated and observed wind fields, respectively, for the sixth model layer above the surface (σ=0.865 or ~880 mbar) at 00 UT, July 7, 1986. The model simulates the weather pattern very well. Both figures show anticyclonic flow within the domain and a smaller anticyclonic feature in the northwest corner at this level. The most obvious discrepancies between the wind fields occur when the observed winds are light and variable. Thus the predicted center of the large-scale anticyclone is about 180 km northwest of that inferred from the observations, and smaller-scale features (i.e., cyclonic curvature over Alabama and Georgia and imbedded anticyclonic curvature over central Kentucky) are absent in the model-predicted winds. Figure 2*c* shows the cloud optical depths predicted at the model surface averaged from 9 a.m. to 5 p.m. EST (1400 to 2200 UT) on July 6, 1986, along with the position of the surface warm and cold fronts from the NMC analysis associated with the Canadian low pressure system at 2100 UT. Details on how the optical depths are determined will be discussed in the photolysis and radiation section (section 2.3.3). However, Figure 2*c* illustrates the coincidence between the observed frontal locations and the model-predicted cloudiness associated with the synoptic features just described.

The reason that the model simulation for this period is carried out only 4 days is related to the synoptic situation, to the focus of our study on photochemical O_3 formation in the lowest 2 or 3 km of the troposphere, and to the lifetimes of the key species important to O_3 photochemistry in this altitude range. For this

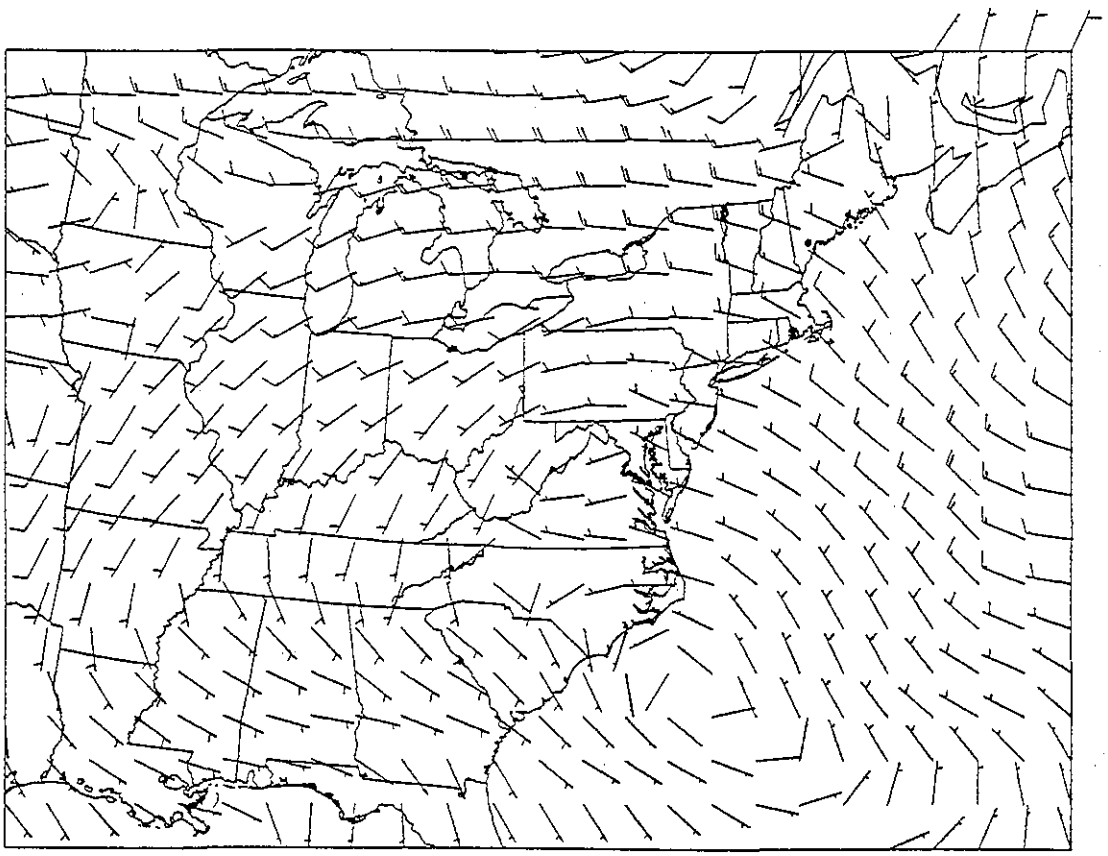

Fig. 2*a*. The model-predicted horizontal wind field at the tenth model level (average pressure = 880 mbar), at 1200 UT, July 6 1986. Small increments are 5 m s^{-1}, large increments are 10 m s^{-1}.

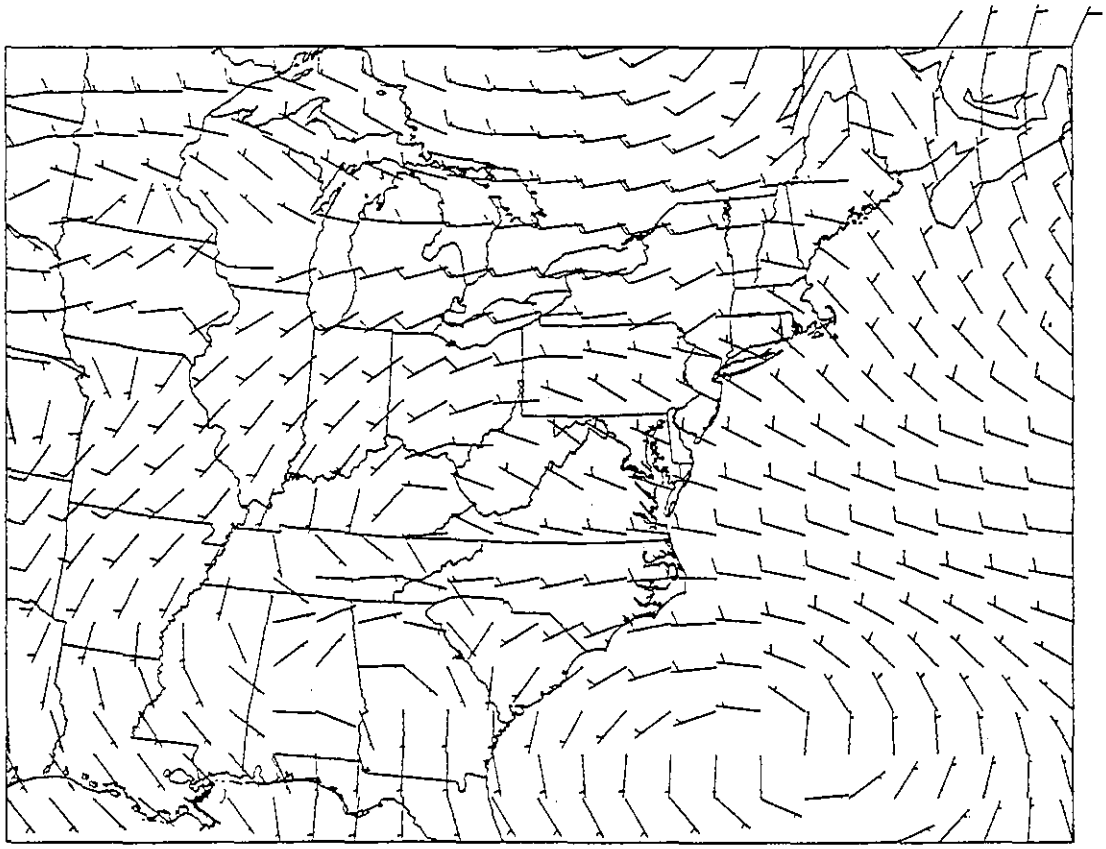

Fig. 2b. The horizontal wind field at about 880 mbar at 1200 UT July 6, 1986, derived from interpolation of the NWS radiosonde observations.

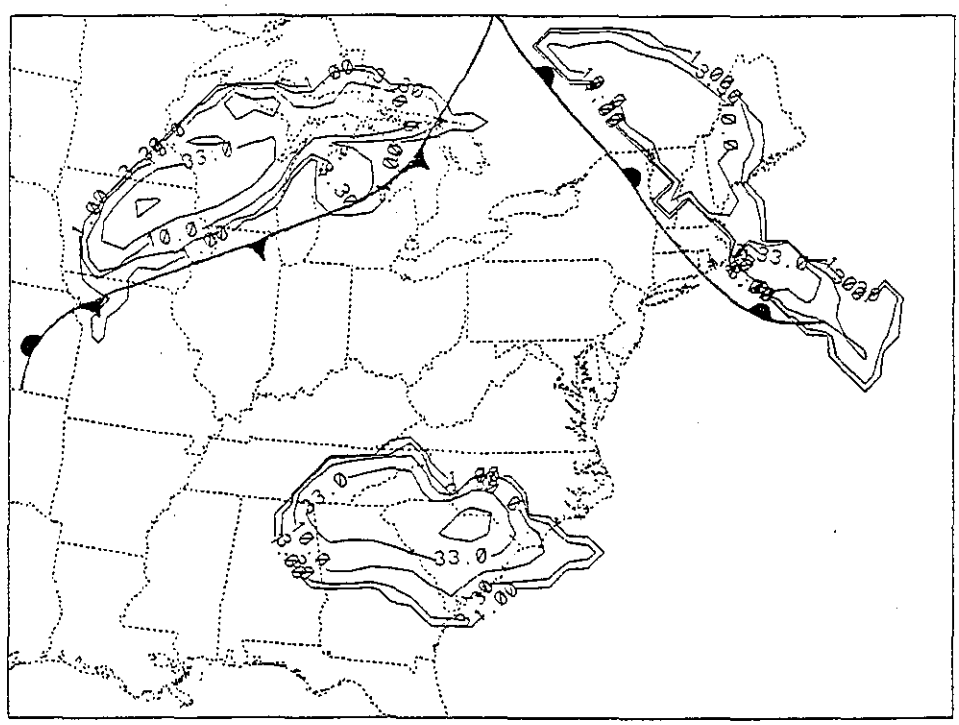

Fig. 2c. Model derived cloud optical depths integrated from the surface level to 15 km and averaged from 1400 to 2200 UT July 6, 1986. Also shown are the observed frontal locations as given in the synoptic NMC analysis for 2100 UT July 6, 1986.

meteorological situation, the center of the high pressure system moves out of the majority of the model domain on July 7, 1986 with a surface low-pressure trough extending down the entire eastern seaboard through Georgia and Alabama. Further model calculation is equivalent to starting the simulation over with a new air mass defined by the boundary conditions and is therefore not relevant to the primary focus of this study, i.e., O_3 formation under a single well-defined high-pressure system. In order to minimize the influence of initial conditions, the model should be run over a period of time that is longer than the photochemical lifetimes of the key species. As is shown in the O_3 budget section of this paper, the photochemical lifetimes of ozone and its major precursors averaged over the lower 2 km are all less than 3 days. Our simulations therefore span a long enough time to allow regional O_3 to build up photochemically.

2.2. *The Transport Model*

In sigma coordinates, the continuity equation for a chemically reactive species becomes [*Haltiner*, 1971]

$$\frac{\partial p^*\chi}{\partial t} = -\frac{\partial p^*\dot{\sigma}\chi}{\partial \sigma} - m^2\nabla_\sigma \frac{p^*\bar{v}\chi}{m} + \frac{\partial p^*\chi}{\partial t}\Big|_{\text{subgrid}} + p^*(P - L\chi) \quad (2)$$

where χ is the species mixing ratio, P and L are mixing ratio production and loss terms due to chemistry, $\bar{v}$ is the horizontal wind speed in sigma coordinates, m is the map-scale factor and ∇_σ is the rectilinear horizontal gradient operator on constant σ surfaces. The species that are transported, and the formulation of the chemical production and loss terms are discussed in the following section. In addition to the wind field, the MM4 model also provides the coefficients associated with subgrid-scale mixing. These variables include horizontal and vertical diffusion coefficients and Blackadar planetary boundary layer mixing parameters [*Blackadar*, 1979], all updated at half-hour intervals. The treatment of transport and numerical integration is very similar to that of *Chang et al.* [1987], except in the description of convective transport within the active PBL. The horizontal and vertical diffusion tendency terms are expressed as

$$\frac{\partial p^*\chi}{\partial t}\Big|_{\substack{\text{horizontal}\\ \text{diffusion}}} = m^2 p^* \nabla_\sigma \frac{K_H \nabla_\sigma \chi}{m} \quad (3)$$

$$\frac{\partial p^*\chi}{\partial t}\Big|_{\substack{\text{vertical}\\ \text{diffusion}}} = \frac{p^*\partial}{\rho\,\partial z}\left(\rho K_z \frac{\partial \chi}{\partial z}\right) \quad (4)$$

where ∇_σ is the horizontal gradient operator on constant sigma surfaces and ρ is the air density. Horizontal diffusion coefficients (K_H) are calculated according to wind shear derived in the dynamic model [*Smagorinsky et al.*, 1965]. Although horizontal diffusion is considered, for reasons to be discussed with regard to numerical integration, the diffusion coefficients derived in this manner are usually small in comparison with the numerical diffusion inherent in the advection scheme.

A mixing scheme [*Blackadar*, 1979; *Zhang and Anthes*, 1982] is used to compute the tendency term within the PBL during free convection:

$$\frac{\partial p^*\chi}{\partial t}\Big|_{\substack{\text{PBL}\\ \text{mixing}}} = p^* m_z(\chi_s - \chi) \quad (5)$$

where χ_s is the mixing ratio at the lowest model level. The tendency at the lowest model layer is calculated from mass conservation. The mixing parameter m_z, as determined by MM4, averages around 2×10^{-3} s^{-1}, and the tendency term of equation (5) usually dominates all other transport terms within the active PBL. Although the average peak height for continental areas at 5 p.m. is roughly 1.4 km, maximum PBL heights as high as 2 km over relatively dry, cloud-free regions are predicted by MM4. PBL heights as low as 70 m are predicted over the ocean, with a diurnal average of ~ 200 m. The PBL height is depressed significantly by the presence of clouds and is assumed to be zero at night over land.

2.2.1. *Numerical methods.* The transport tendency due to advection is calculated according to the iterated upstream finite difference advection algorithm of *Smolarkiewicz* [1983, 1984] with one corrective step and cross terms included. This algorithm is positive definite, mass conserving (CDC Cyber 205 machine accuracy of ~1 part in 10^{12}, single precision), and computationally inexpensive but possesses the undesirable characteristic of appreciable numerical diffusion due to inaccuracies in the numerical approximations of spatial and temporal gradients [*Brost et al.*, 1988]. We have previously analyzed this numerical scheme and quantified the numerical diffusion associated with horizontal advection for real meteorological situations. Numerical diffusion is directly related to wind speed and direction, as well as to the magnitude of the concentration gradient. For our meteorological case, we estimate an average horizontal diffusion coefficient (due to numerical diffusion) of ~2×10^5 m^2-s^{-1} below 3 km, increasing to ~7×10^5 m^2-s^{-1} at 10.5 km in the limiting case of extremely sharp gradients. These values are at least a factor of 10 greater than horizontal diffusion coefficients derived from observations of point sources [*Gifford*, 1982] and on the average are also about a factor of 4 larger than the coefficients derived according to wind shear [*Smagorinsky et al.*, 1965]. The numerical diffusion introduced by the advection algorithm certainly introduces a degree of uncertainty in the predicted distribution of O_3 and its precursors, particularly from strong point sources. However, since horizontal diffusion is typically of secondary importance at higher altitudes because of higher wind velocities and boundary condition dependence [*Brost*, 1988] and is of secondary importance below ~3 km because of the dominance of vertical mixing [*Brost et al.*, 1988], numerical diffusion introduced by the advection algorithm is probably secondary to other uncertainties in the meteorological and chemical variables. This same conclusion has also been drawn by others who have used or tested the same algorithm [eg., *Ko et al.*, 1985; *Rood*, 1987] for stratospheric conditions. In relation to the comparison of observed and model-predicted O_3, we present evidence suggesting that uncertainties in parameterizing vertical exchange by cloud transport are a limiting factor in the model's ability to reproduce observed O_3.

The sum of advection, diffusion, and mixing tendency terms comprise the net transport tendency, which is calculated with a 150-s time step. The tendencies due to vertical diffusion in equation (4) (above the PBL and in stable regimes) are calculated explicitly with the 150-s time step, or sufficient subiterations to ensure numerical stability. Similarly, the tendencies due to mixing (equation 5) are explicitly calculated for a 150-s time step using subiterations that ensure better than 10% accuracy in comparison to exact analytical solutions of equation (5).

2.2.2. *Treatment of deposition.* A flux boundary condition for species known to undergo significant surface deposition is included in the model. The flux to the surface is the product of the concentration at the first level ($\rho\chi$) and the deposition velocity at the surface (v_d). Following the formulation of *Wesley and Hicks* [1977], the inverse of the deposition velocity is the resistance to deposition, and is the sum of the aerodynamic resistance (r_a) and the surface resistance (r_s). The surface resistances are assumed to be invariant with time, and adopted values are listed in Table 3 for those species that are deposited.

TABLE 3. Reciprocal Surface Resistances for Transported Species That Are Deposited

Species	Reciprocal Surface Resistance, cm s^{-1}
O_3*	0.5
NO_2	0.4
HNO_3	10.0
H_2O_2	0.5
CH_3OOH	0.5
CH_2O	0.3
CH_3CHO	0.3
PAN	0.3
SO_2	0.3
PPN	0.3
MEK	0.3
RCHO	0.3

*O_3 deposition velocity reduced to 0.1 cm s^{-1} over water surfaces.

The original formula from *Wesely and Hicks* [1977] is valid in the lowest few meters of the boundary layer. We use the same formula to compute the aerodynamic resistance, and assume that this value (r_{as}) is valid for a thin layer from ground up to 1 m:

$$r_{as} = \frac{1}{ku^*}\left(\ln\frac{z}{z_0} + 2.6 - \phi_c\right) \quad (6)$$

where z is height (taken to be 1 m), z_0 is the roughness length (dependent on land use category, Table 4), k is von Karman's constant (0.4) and u^* is the friction velocity. The nondimensional concentration stratification function ϕ_c can be assumed to be equal to the thermal stratification function ϕ_h and is calculated according to *Businger et al.* [1971] by

Neutral conditions

$$\phi_h = 0.74$$

Stable conditions

$$\phi_h = 0.74 + 4.7\left(\frac{z}{L}\right)$$

Unstable conditions

$$\phi_h = 0.74\left(1. - \frac{9z}{L}\right)^{-1/2}$$

L is the Monin-Obukhov length, given by

$$L = -\frac{Tu^{*3}}{kg\overline{w'T'}}$$

where $\overline{w'T'}$ is the surface heat flux, g is acceleration due to gravity and T is temperature.

TABLE 4. Roughness Lengths for Different Land Use Categories

Land Use Category	Roughness Length z_0, cm
Urban land	100
Agriculture	15
Range-grassland	12
Deciduous forest	100
Coniferous forest	100
Mixed wetland + forest	90
Water	0.00001
Marsh	20
Desert	10
Tundra	10
Permanent ice	5
Tropical forest	150
Savannah	15

The aerodynamic resistance for the rest of the lowest model layer is computed by

$$r_{at} = \int_{1m}^{z_1} \frac{dz}{K_z}$$

where z_1 is the height of the lowest model layer. So the total aerodynamic resistance r_a is the sum of r_{as} and r_{at}. By definition of the vertical diffusion coefficient in the surface layer,

$$K_z = \frac{ku^*z}{\phi_h}$$

the aerodynamic resistance for the upper layer r_{at} can be computed as

Neutral conditions

$$r_{at} = .74\frac{\ln(z_1)}{ku^*}$$

Stable Conditions

$$r_{at} = .74\frac{\ln(z_1)}{ku^*} + 4.7\frac{(z_1 - 1)}{Lku^*}$$

Unstable conditions

$$r_{at} = \frac{.74}{ku^*}\left[\ln(z_1) - \ln\left\{\frac{1+(1-9z_1/L)^{1/2}}{1+(1-9/L)^{1/2}}\right\}\right]$$

Table 4 gives the roughness lengths for each land use category specified within the MM4 model [*Anthes et al.*, 1987], used in calculating equation (6).

2.3. *Treatment of Chemistry*

The chemical species and reactions considered in this study are essentially those of *Trainer et al.* [1987*a*]. The species considered are listed in Table 5, along with the solution method for determining the concentration. Those species that are transported have appreciably long chemical lifetimes, and the tendency due to transport for these species is calculated as discussed in the

TABLE 5. Chemical Species Considered, and Method of Determination

Determination Method	Species
Species that undergo transport and chemical integration	O_x[a], NO_x[b], HNO_3, H_2O_2, CH_3OOH, CO, isoprene + α-pinene, CH_2O, CH_3CHO, PAN[c], higher-alkanes (>C_4), SO_2, butanes, ethene, higher-alkenes (>C_2), PPN[d], MEK[e], RCHO[f]
Species determined only by chemical integration	OH, HO_2, ΣRO_2, $NO_3 + N_2O_5$, HO_2NO_2, $NO + NO_2$
Species determined by equilibrium conditions	O^1D, O_3, NO, NO_2, NO_3, N_2O_5, HONO, individual RO_2, CH_2OO, CH_3CHOO
Species held at fixed mixing ratio	H_2 (500 ppbv), CH_4 (1.64 ppmv)

[a] $O_3 + NO_2 + 2NO_3 + 3N_2O_5 + HO_2NO_2$.
[b] $NO + NO_2 + NO_3 + 2N_2O_5 + HO_2NO_2 + HONO$.
[c] $CH_3COO_2NO_2$.
[d] $C_2H_5COO_2NO_2$.
[e] Methylethylketone.
[f] C_2H_5CHO.
[g] $CH_3COO_2 + CH_3O_2 + C_4H_9O_2 + C_2H_4OHO_2 + C_3H_6OHO_2 + C_2H_5COO_2 + C_2H_4O_2COCH_3 + C_2H_5O_2$.

preceding section. Species calculated with the quasi-steady state approximation (QSSA) [*Hesstvedt et al.*, 1978] have chemical lifetimes short enough that transport has little effect on their distributions but long enough that photochemical equilibrium may not be achieved within the 150-s time step. O^1D, the ratio of NO to NO_2, and the Creigee intermediates are assumed to be controlled by photochemical equilibrium. For computational efficiency, use is made of species grouping [*Liu*, 1977].

Only gas phase photochemistry is considered within the model formalism. Although aqueous phase chemistry is necessary for model applications related to acid deposition [*Chang et al.*, 1987], our emphasis in this study is on photochemical oxidant formation. A recent publication by *Lelieveld and Crutzen* [1990] has addressed the importance of cloud chemistry to global models of O_3 and related precursors. Although this study shows that aqueous chemistry can lead to reductions in net O_3 formation between 1.5 and 3 km for summer northern hemisphere mid-latitude conditions with NO_x levels typical of anthropogenic influence, these reductions become significant only over time scales longer than the 4 day period simulated in our model. With a typical air mass cycling frequency of ~3 hours in cloud, and 16 hours in cloud free regions assumed in their study, and the additional inclusion of N_2O_5 loss to clouds, the authors find a net O_3 formation decrease of ~1.5 ppbv d^{-1} averaged over daytime. Such changes would have only a minor impact on our predicted O_3 below 2 km over the 4-day period. Furthermore, our model does include N_2O_5 loss (to aerosols), which accounts for a significant fraction of the net O_3 formation decrease in the Lelieveld and Crutzen study. The choice of a high-pressure system for our simulations additionally minimizes the fraction of the model domain expected to be influenced by clouds.

2.3.1. *Anthropogenic and natural emissions inventory.* The most recent NAPAP inventory for 1985 [*U.S. EPA*, 1989] is utilized for anthropogenic NO_x and NMHC emissions. Summertime, weekday conditions were assumed throughout the 4-day simulation, with values being updated hourly. Although the 4-day period was a weekend, we did not use the weekend emission data because it was a July 4 long weekend. There is uncertainty in how this holiday condition would fit into the given emission classification of typical weekday, Saturday, or Sunday. Average NO_x

TABLE 6. NAPAP Emission Inventory (Averages) for U.S. Land Area Within the Model Domain

Species	Total Emission[a]	Area Emission	Point Emission	Mobile Fraction[b]	Lumped Species
NO	17.9	9.2	8.67	0.683	
NO_2	0.826	0.495	0.331	0.669	
CO	81.9	73.1	8.79	0.754	
VOC[c]	158.0	140.0	17.6	0.620	
SO_2	18.0	1.28	16.8	0.265	
Alkane(0.25-0.5)[d]	1.19	1.12	0.067	0.649	butane
Other(0.25-0.5)	1.02	0.92	0.096	0.000	butane
Alkane(0.5-1)	1.26	1.17	0.088	0.624	higher-alkanes
Alkane(1-2)	1.18	1.04	0.140	0.440	higher-alkanes
Alkane(>2)	0.133	0.124	0.009	0.293	higher-alkanes
Other(0.5-1)	0.888	0.817	0.071	0.008	higher-alkanes
Other(>1)	0.238	0.201	0.036	0.038	higher-alkanes
Alkane/Aromatic	0.108	0.086	0.023	0.199	higher-alkanes
Aromatic(<2)	0.758	0.616	0.142	0.394	higher-alkanes
Aromatic(>2)	0.808	0.734	0.074	0.569	higher-alkanes
Ethene	1.26	1.16	0.103	0.454	ethene
Propene	0.162	0.132	0.030	0.141	propene
Primary alkene	0.223	0.206	0.016	0.448	propene
Internal alkene	0.518	0.499	0.018	0.654	propene
Prim/Int alkene	0.097	0.091	0.006	0.039	propene
CH_2O	0.439	0.366	0.073	0.338	CH_2O
Higher aldehyde	0.158	0.138	0.020	0.205	CH_3CHO
CH_4[e]	5.04	4.46	0.585	0.467	
Ethane	0.410	0.348	0.062	0.452	
Propane	0.413	0.364	0.048	0.323	
Benzenes	0.272	0.218	0.054	0.035	
Phenol/cresol	0.031	0.174	0.132	0.000	
Styrenes	0.092	0.076	0.016	0.000	
Acetone	0.114	0.080	0.034	0.000	
Higher ketone	0.115	0.074	0.041	0.000	
Organic acids	0.048	0.040	0.009	0.000	
Acetylene	0.330	0.278	0.052	0.469	
Haloalkenes	0.145	0.134	0.011	0.000	
Unreactive	0.170	0.140	0.030	0.000	
Other(<0.25)	0.178	0.123	0.055	0.000	
Unidentified	0.397	0.383	0.013	0.857	
Unassigned	0.232	0.202	0.030	0.008	
NH_3	2.61	2.03	0.572	0.156	

[a]All emissions (except VOC) are in units of 10^{14} molecule m^{-2} s^{-1}.
[b]Mobile fraction refers to the fraction of area emissions due to mobile sources (i.e., automobiles).
[c]VOC emissions are in nanogram m^{-2} s^{-1}.
[d]Numbers in parentheses refer to NAPAP OH reactivity classes in units of 10^4 ppm^{-1} min^{-1}.
[e]Emissions of species from CH_4 to NH_3 are not included in the model.

emissions for a typical Saturday and Sunday are only ~10% and 20% below typical weekday emissions, while average NMHC emissions are reduced 24% and 35% [*U.S. EPA*, 1989]. Since uncertainties in the emissions of these species, regardless of the day-of-week classification, are much higher than these changes, and more traffic is expected for a holiday weekend than a typical weekend, we have chosen to adopt the weekday emissions scenario. Table 6 gives the diurnal averages of the various NAPAP emission classes over the continental region of the model domain, as well as the partitioning of these sources into the species used within the model. The NAPAP inventory is divided between emissions from height-resolved individual stacks or point sources (~34,000 individual points within the study area), and mobile or nonmobile area sources averaged over 1/4° longitude by 1/6° latitude (~20×20 km^2) grids. Mobile area sources represent emissions due to all forms of motorized vehicles, while the nonmobile area sources are emissions from all other anthropogenic sources, as well as ground level industrial sources that emit less than 5 tons per year of total hydrocarbon (THC) or NO_x, and industrial stacks that emit less than 100 tons per year of THC or NO_x. As is evident from Table 6, mobile area emissions account for a significant fraction of the anthropogenic alkanes and alkenes and for ~35% of the total NO_x. The point sources dominate SO_2 emissions and comprise 48% of the total NO_x but contribute little to the NMHC emissions. The spatial distribution of the diurnally averaged point plus area emissions for NO_x and butane averaged over the model grid size of 60×60 km^2 are shown in Figures 3*a* and 3*b*, respectively. Seventy percent of the butane emissions are from mobile sources, which is reflected in the congruence of high emissions and populated urban centers in Figure 3*b*. The pattern of NO_x emissions exhibits influence from both of the area and point source categories, as is shown in Figure 3a. Large emissions associated with coal-fired electricity-generating facilities account for a significant fraction of the NO_x emitted throughout the Ohio River valley.

The natural emissions of isoprene and α-pinene are based on the most recent EPA data for land use and forest type. The EPA land use data is in terms of land area per 1/6° latitude by 1/4° longitude grid for each vegetative type. The emissions from deciduous and coniferous forests are derived according to *Lamb et al.* [1987]. Following this procedure, each forest type is divided into four vegetative categories. These include high isoprene, low isoprene, deciduous with no isoprene, and coniferous emitters. The vegetation biomass factors of *Lamb et al.* [1987] (units of kilograms per hectare) are used to convert hectares of forest type into kilograms of biomass for each vegetative category and for each model grid. Emission factors relating individual NMHC to the four vegetative categories (units of μg g^{-1} h^{-1}) for the forested areas, and emission factors relating NMHC amounts to crop type (μg m^{-2} hr^{-1}) are those used by EPA for compiling natural NMHC inventories (T. E. Pierce, Atmospheric Sciences Modeling Division, personal communication, 1989). Besides isoprene and

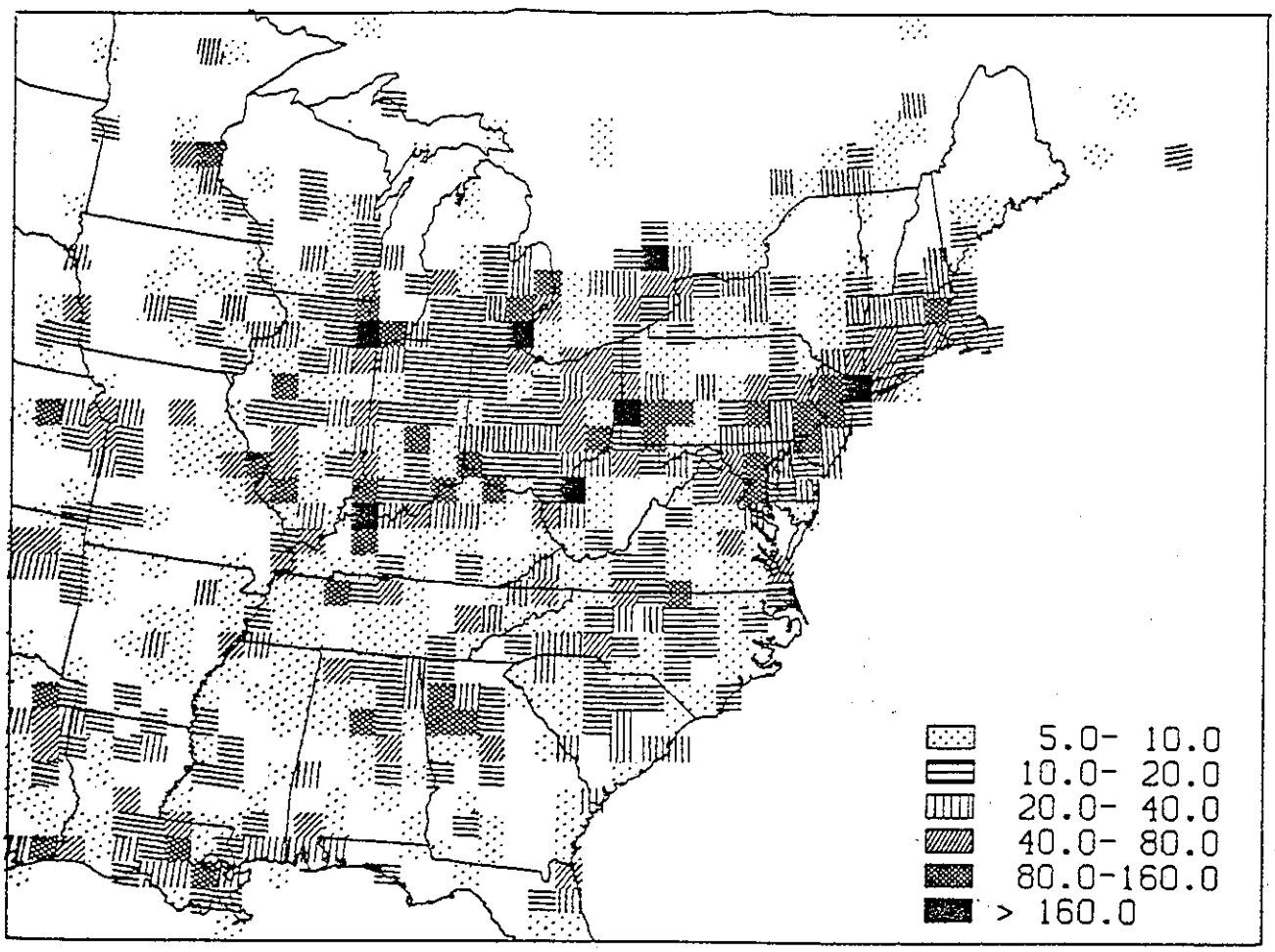

Fig. 3*a*. Diurnally averaged NO_x emissions for a summertime weekday, from the NAPAP 1985 (version 5.2) emission inventory with the 60×60 km model resolution. Both area and point sources are included. Emissions are in units of 10^{14} molecule m^{-2} s^{-1}.

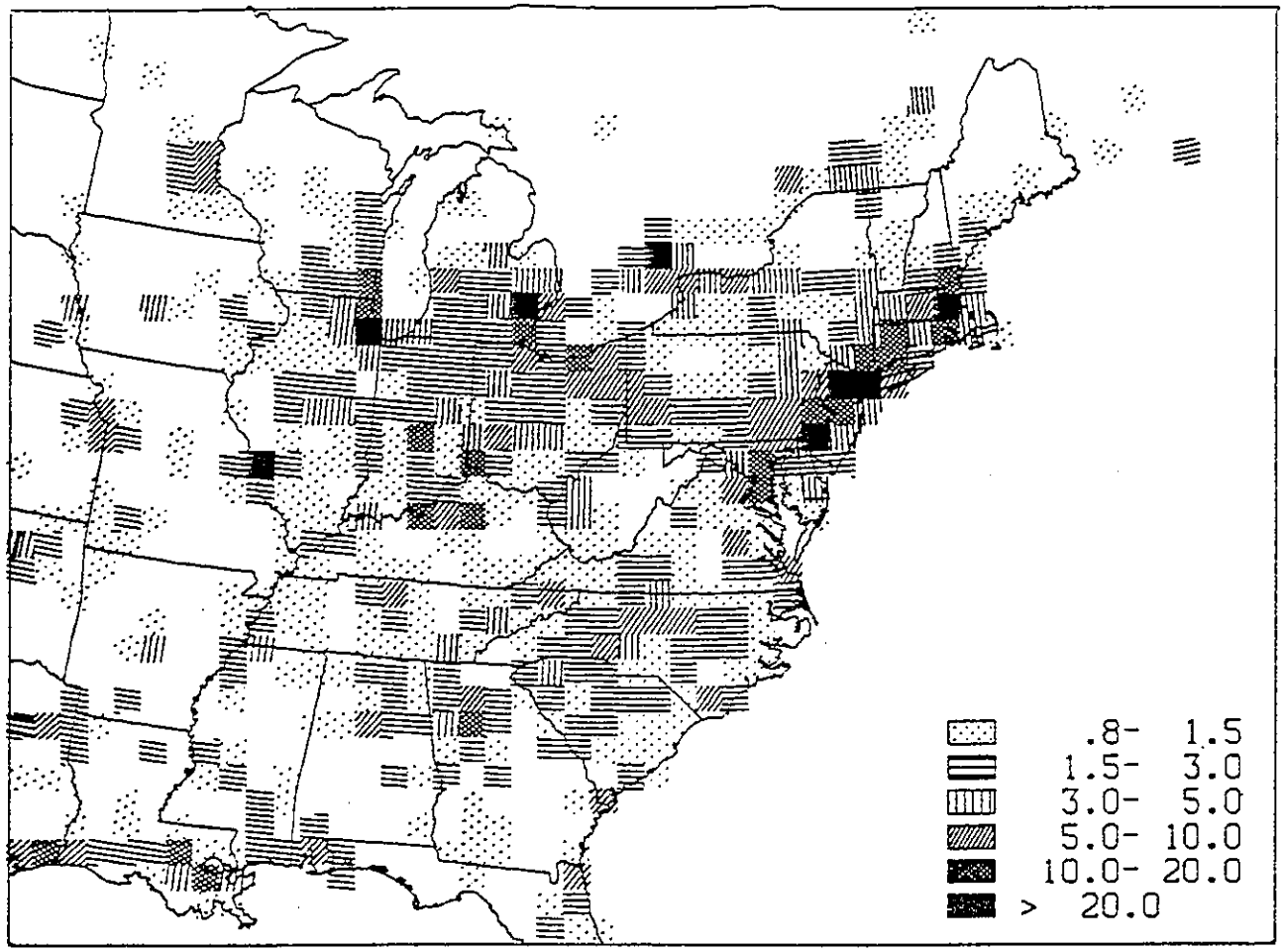

Fig. 3*b*. Diurnally averaged butane emissions for a summertime weekday, from the NAPAP 1985 (version 5.2) emission inventory with the 60×60 km model resolution. Both area and point sources are included. Emissions are in units of 10^{14} molecule m^{-2} s^{-1}.

α-pinene, the EPA data also account for monoterpenes other than α-pinene, and an unknown component that is assumed to be unreactive. The different forest type and crop categories, individual NMHC fractions, and fractional area coverage are shown in Table 7 for 30°C conditions. These data are not corrected for cloudiness or canopy effects but clearly indicate the predominance of deciduous forests as the main isoprene source. Averaged over the model domain, α-pinene emissions are mostly emitted by coniferous forests, but deciduous forests and corn crops also make significant contributions. The temperature dependence of isoprene and α-pinene emissions are also taken from *Lamb et al.* [1987]. The light intensity dependence of the isoprene emissions and canopy correction terms to account for the reduction of light by foliage are those of *Jacob and Wofsy* [1988].

The inclusion of natural NO_x emissions within the model is based upon the NO flux measurements of *Williams et al.* [1987, 1988]. Because of the observed strong dependence of the NO emissions on soil nitrate and soil moisture, which are two quantities not treated within the model, we have simply assigned a natural NO emission of 1.2×10^{14} molecules m^{-2}-s^{-1} to all grids over land. Although this assignment will overpredict natural NO emissions in forested areas, and underpredict fertilized crop areas [*Williams et al.*, 1988], it is representative of grasslands and pasture, which comprise a large fraction of the relatively sparsely populated western portion of our model domain. Since the assigned value is less than 5% of the average anthropogenic NO_x emission (see Table 6), the influence of the natural emissions is generally negligible.

Emissions from both natural and anthropogenic sources are incorporated into the model as grid averaged production terms within the chemical module. Anthropogenic point sources are partitioned vertically according to stack height, while all other emissions take place in the bottom layer.

2.3.2. *The chemical mechanism.* A standard reaction scheme for CH_4, CO, H_2O, O_3, and NO_x chemistry used in our calculations has been discussed by *Liu et al.* [1980]. Reaction rates for this scheme have been updated to *Jet Propulsion Laboratory* (JPL) [1987]. A complete list of reactions and their rates is presented in Table 8.

Also listed in Table 8 are the reaction mechanisms and rate constants of the NMHC. Since explicit treatment of the NMHC in the three-dimensional model is prohibitively expensive in terms of computer resources, lumping techniques are needed to simplify the organic chemistry [e.g., *Dodge*, 1977; *Atkinson et al.*, 1982; *Lurmann et al.*, 1986; *Stockwell*, 1986; *Gery et al.*, 1989]. The chemical mechanisms for the anthropogenic NMHC and isoprene in this study are based on the study of *Atkinson et al.* [1982], with the updated modifications recommended by *Lurmann et al.* [1986]. However, unlike the Lurmann et al. mechanism, we include an alkane class (higher alkane) that represents $\geq C_4$ alkanes other than butane, similar to the original Atkinson et al. scheme. This chemical mechanism is like the RADM mechanism [*Stockwell*,

TABLE 7. Total Hydrocarbon Emission Rates and NMHC Fractions at 30°C, and Land Surface Fractions for Different Vegetative Types

Vegetation Type	Emission $\mu g\ m^{-2}\ hr^{-1}$	Monoterpene Fraction	α-Pinene Fraction	Isoprene Fraction	Unknown Fraction	Fraction of Area[d]
Oak forest[a]	4256.2	0.028	0.026	0.731	0.215	0.1529
Deciduous[b]	3356.3	0.058	0.052	0.627	0.262	0.2056
Coniferous[c]	3106.3	0.235	0.206	0.24	0.320	0.1513
Alfalfa	37.9	0.1	0.1	0.5	0.3	0.0151
Sorghum	39.4	0.25	0.25	0.2	0.3	0.0043
Hay	189.0	0.25	0.25	0.2	0.3	0.0384
Soybean	22.2	0.0	0.0	1.0	0.0	0.0629
Corn	3542.0	0.1	0.1	0.0	0.8	0.0739
Potatoes	48.1	0.25	0.25	0.0	0.5	0.0016
Tobacco	294.0	0.1	0.1	0.0	0.8	0.0010
Wheat	30.0	0.1	0.1	0.5	0.3	0.0173
Cotton	37.9	0.25	0.25	0.2	0.3	0.0036
Rye	37.9	0.25	0.25	0.2	0.3	0.0002
Rice	510.0	0.25	0.25	0.2	0.3	0.0021
Peanuts	510.0	0.25	0.25	0.2	0.3	0.0011
Barley	37.9	0.25	0.25	0.2	0.3	0.0025
Oats	37.9	0.25	0.25	0.2	0.3	0.0196
Range+Scrub	189.0	0.25	0.25	0.2	0.3	0.0035
Grass	281.0	0.25	0.25	0.2	0.3	0.1542
Urban grass	281.0	0.25	0.25	0.2	0.3	0.0086
Other crops	37.9	0.25	0.25	0.2	0.3	0.0237
Water						0.0570

[a]Oak, deciduous, and coniferous forest type data were calculated using the weight factors for the four vegetative categories of *Lamb et al.* [1987] and the NMHC species emission factors for these categories from the EPA (T. E. Pierce, private communication, 1989).
[b]Deciduous refers to deciduous forest canopy other than oak.
[c]Coniferous refers to coniferous forest canopy.
[d]Fraction of area refers to the fraction of land area.

1986], in that species are grouped according to OH reactivity. Thus the 1985 NAPAP emissions inventory, designed for RADM applications, is directly applicable. The assignment of 1985 emissions classification into the lumped NMHC adopted here is shown in the last column of Table 6. The NAPAP emission inventory (Table 6) provides only limited information on the composition of the NMHC, so a detailed classification is not warranted. Furthermore, because the emphasis of our study is on the rural atmosphere, the extremely reactive NMHC such as higher aromatics and higher alkenes are lumped into less reactive NMHC groups as described below. The dominant species within each of the NAPAP lumped categories are enumerated in Table 9.

For the butane class within the model, it can be seen from Table 6 that the other alkane(0.25-0.5 OH reactivity) class, which is dominated by ethyl alcohol, accounts for nearly 50% of the emissions. The OH reaction rate assigned to the model higher-alkane class is taken to be that of hexane, or nearly 1×10^4 ppm^{-1} min^{-1}, which corresponds to the emission weighted OH reaction rate of the alkane classes above C4 (Table 6). The aromatic(<2.0) class is dominated by toluene emissions which also have a similar OH reaction rate [*Atkinson*, 1985]. Assigning the aromatic(>2.0) NAPAP class to the higher-alkane model class certainly underestimates the net reactivity close to emission sources, but the high reactivity of these species implies that concentrations will be generally quite low and unimportant as primary precursors to O_3 formation in rural areas. There are, however, several intermediate carbonyls and organic nitrates generated in the oxidation of the species within the aromatic classes [*Atkinson*, 1985; *Calvert and Madronich*, 1987] that are inherently neglected within the lumped species approach. Since the intermediate ketone of the higher-alkane class is assumed to be methylethylketone [*Lurmann et al.*, 1986], which has a longer lifetime than the carbonyls generated by the aromatics, the O_3 formation potential is relatively more diffuse for the fraction emitted as aromatics. We have performed tests with the three-dimensional model that have the reactivity of the higher-alkane class increased by a factor of 4. While O_3 close to urban areas is sensitive to this modification, regionally averaged O_3 is only influenced by a few percent. Thus the results of this study pertaining to rural O_3 formation are not particularly sensitive to the loss of reactivity inherent in our lumping approach.

For the model propene class, the NAPAP primary alkenes are dominated by butene emissions, which have an OH reaction rate only 20% higher than propene. However, the internal alkene class consists of species that are 2 to 3 times more reactive than propene. Consistent with the mechanism of *Lurmann et al.* [1986], these highly reactive alkenes have been lumped into the propene class. Similar to the arguments for reactive aromatics, these species are not expected to contribute significantly outside of urban areas. Although simplifications necessary in deriving a manageable set of reactions to describe the oxidation of anthropogenic NMHC inherently introduce a degree of uncertainty, we believe that the essential features concerning their role in rural O_3 formation are captured by the mechanism.

The isoprene oxidation mechanisms of *Killus and Whitten* [1984] or *Lloyd et al.* [1983] are restrictively complex for direct inclusion into three-dimensional calculations. As a consequence, we keep the reaction rate constants of isoprene but assume the products of propene oxidation with OH and O_3 as surrogate products for the equivalent isoprene reactions in a manner consistent with the condensed version of *Lurmann et al.* [1986].

The applicability of the propene surrogate mechanism was tested by using the one-dimensional photochemical model of *Trainer et al.* [1987a] to compare calculations with the condensed version against the full mechanism of *Lloyd et al.* [1983]. For

TABLE 8. Reactions in the Three-Dimensional Model

Number	Reaction	Rate	Notes*
(QK1)	$O^1D + [M] \rightarrow O^3P + [M]$	2.87^{-11}	
(8)	$O^1D + H_2O \rightarrow OH + OH$	2.2^{-10}	
(11)	$O^1D + CH_4 \rightarrow OH + CH_3$	1.4^{-10}·1.1	
(12)	$OH + CH_4 \rightarrow H_2O + CH_3$	$2.3^{-12}e^{-1700/T}$	
(13)	$O^1D + H_2 \rightarrow OH + H$	1.0^{-10}	
(13b)	$OH + H_2 \rightarrow H_2O + H$	$5.5^{-12}e^{-2000/T}$	
(17a)	$OH + CO \rightarrow H + CO_2$	$1.5^{-13}(1.+.6p_{atm})$	
(18)	$OH + HO_2 \rightarrow H_2O + O_2$	$4.6^{-11}e^{230/T}$	
(19)	$OH + O_3 \rightarrow HO_2 + O_2$	$1.6^{-12}e^{-940/T}$	
(21)	$O_3 + HO_2 \rightarrow OH + 2O_2$	$1.1^{-14}e^{-500/T}$	
(22)	$HO_2 + HO_2 \rightarrow H_2O_2 + O_2$	$2.3^{-13}e^{600/T} + 1.7^{-33}[M]e^{1000/T} \times(1.+1.4^{-12}e^{2200/T}[H_2O])$	
(23)	$OH + H_2O_2 \rightarrow HO_2 + H_2O$	$3.3^{-12}e^{-200/T}$	
(24)	$HO_2 + NO \rightarrow OH + NO_2$	$3.7^{-12}e^{240/T}$	
(26)	$O_3 + NO \rightarrow NO_2 + O_2$	$2.0^{-12}e^{-1400/T}$	
(29)	$OH + HNO_3 \rightarrow H_2O + NO_3$	$k_0+[k_3[M]/(1+k_3[M]/k_2)]$	k of *JPL* [1987]
(30)	$OH + NO_2 \rightarrow HNO_3$	Troe expression	
(41)	$NO + NO_3 \rightarrow 2NO_2$	$1.7^{-11}e^{150/T}$	
(43)	$O_3 + NO_2 \rightarrow NO_3 + O_2$	$1.4^{-13}e^{-2500/T}$	
(44)	$NO_2 + NO_3 \rightarrow N_2O_5$	Troe expression	
(45)	$N_2O_5 \rightarrow NO_2 + NO_3$	$R44/(1.1^{-27}e^{11200/T})$	
(46)	$NO_3 + NO_3 \rightarrow 2NO_2 + O_2$	$8.5^{-13}e^{-2450/T}$	*Cantrell et al.* [1985]
(47)	$HO_2 + NO_3 \rightarrow 0.6(OH + NO_2) + 0.4HNO_3$	$2.3^{-12}e^{170/T}$	*Hall et al.* [1988]
(50)	$CH_2O + NO_3 \rightarrow HNO_3 + HO_2 + CO$	6.0^{-16}	
(51)	NO_3 + isoprene → organic nitrate	$3.0^{-12}e^{-450/T}$	*Dlugokencky and Howard* [1989]
(52)	$NO_3 + C_3H_6 \rightarrow$ organic nitrate	4.0^{-15}	Recommended rate and products of *Lurmann et al.* [1986]
(53)	$NO_3 + CH_3CHO \rightarrow CH_3COO_2 + HNO_3$	$1.4^{-12}e^{-1900/T}$	
(63)	$HO_2 + CH_3O_2 \rightarrow CH_3OOH + O_2$	$7.7^{-14}e^{1300/T}$	
(64)	$CH_3O_2 + CH_3O_2 \rightarrow 2HO_2 + 2CH_2O + O_2$	$1.9^{-13}e^{220/T}$	
(65)	$CH_3OOH + OH \rightarrow 0.56(CH_3O_2 + H_2O) + 0.44(OH + CH_2O)$	1.0^{-11}	
(66)	$CH_3O_2 + NO \rightarrow NO_2 + CH_2O + HO_2$	$4.2^{-12}e^{180/T}$	
(68)	$OH + CH_2O \rightarrow H_2O + CO + HO_2$	1.0^{-11}	
(71)	$HO + NO \rightarrow HONO$	Troe expression	
(72)	$NO + NO_2 + H_2O \rightarrow 2HONO$	6.0^{-37}	*Atkinson and Lloyd* [1984]
(73)	$N_2O_5 + H_2O \rightarrow 2HNO_3$	1.0^{-30}	
(C71)	$HO_2 + NO_2 \rightarrow HO_2NO_2$	Troe expression	
(C74)	$HO_2NO_2 \rightarrow HO_2 + NO_2$	$RC71\times4.76^{26}e^{-10900/T}$	
(C73)	$HO_2NO_2 + OH \rightarrow NO_2 + H_2O + O_2$	$1.3^{-12}e^{380/T}$	
(75)	$OH + SO_2 \rightarrow SO_4^= + HO_2$	Troe expression	
(76)	$NO_2 + NO_3 \rightarrow NO + NO_2 + O_2$	$2.5^{-14}e^{-1230/T}$	*Atkinson and Lloyd* [1984]
(77)	$CH_3O_2 + CH_3COO_2 \rightarrow CH_3CO_2 + HO_2 + CH_2O + CO_2$	1.0^{-11}	*Moortgat et al.* [1989a]
(78)	$CH_3CO_2 + CH_3COO_2 \rightarrow 2CH_3O_2 + O_2 + CO_2$	2.5^{-12}	*Moortgat et al.* [1989a]
(79)	OH + PAN → products	$1.23^{-12}e^{-651/T}$	*Wallington et al.* [1984]
(80)	$OH + CH_3CHO \rightarrow CH_3COO_2 + H_2O$	$6.9^{-12}e^{250/T}$	
(81)	$NO_2 + CH_3COO_2 + [M] \rightarrow PAN + [M]$	4.7^{-12}	*Atkinson and Lloyd* [1984]
(82)	$PAN \rightarrow CH_3COO_2 + NO_2$	$2.0^{16}e^{-13543/T}$	*Atkinson and Lloyd* [1984]
(83)	$NO + CH_3COO_2 \rightarrow CH_3O_2 + NO_2 + CO_2$	$4.2^{-12}e^{180/T}$ (R66)	
(84)	OH + higher-alkanes → $BUTO_2$	$2.0^{-11}e^{-360/T}$	Recommended rate and products of *Lurmann et al.* [1986]
(85)	$NO + C_2H_5O_2 \rightarrow CH_3CHO + NO_2 + HO_2$	$4.2^{-12}e^{180/T}$ (R66)	
(88)	$OH + C_4H_{10} \rightarrow BUTO_2$	$1.68^{-11}e^{-559/T}$	Recommended rate and products of *Lurmann et al.* [1986]
(89)	$NO + BUTO_2 \rightarrow 0.9NO_2 + 0.1(RCHO$ + org. nit.) $+0.3(C_2H_5O_2 + CH_3CHO) + 0.6HO_2 + 0.47MEK$	$4.2^{-12}e^{180/T}$ (R66)	
(90)	$OH + C_2H_4 \rightarrow ETHYO_2$	Troe expression	
(91)	$NO + ETHYO_2 \rightarrow 2CH_2O + NO_2 + HO_2$	$4.2^{-12}e^{180/T}$ (R66)	
(92)	$OH + C_3H_6 \rightarrow PRPYO_2$	$4.1^{-12}e^{544/T}$	Recommended rate from *Atkinson et al.* [1979]
(93)	$NO + PRPYO_2 \rightarrow CH_3CHO + CH_2O + NO_2 + HO_2$	$4.2^{-12}e^{180/T}$ (R66)	
(94)	$O_3 + C_2H_4 \rightarrow CH_2O + 0.4CH_2OO + 0.12HO_2 + 0.42CO + .06CH_4 + 0.21H_2O + 0.18CO_2 + H_2$	$1.2^{-14}e^{-2633/T}$	Recommended rate and products of *Lurmann et al.* [1986]
(95)	$O_3 + C_3H_6 \rightarrow 0.52CH_2O + 0.2(CH_2OO + CH_3CHOO) + 0.10H + 0.21CH_3O_2 + 0.5CH_3CHO + 0.33CO + 0.23HO_2$	$1.3^{-14}e^{-2105/T}$	Recommended rate and products of *Lurmann et al.* [1986]
(97)	$NO + CH_2OO \rightarrow NO_2 + CH_2O$	7.0^{-12}	Recommended rate and products of *Lurmann et al.* [1986]
(98)	$NO_2 + CH_2OO \rightarrow NO_3 + CH_2O$	7.0^{-13}	Recommended rate and products of *Lurmann et al.* [1986]
(99)	$SO_2 + CH_2OO \rightarrow SO_4^= + CH_2O$	7.0^{-14}	Recommended rate and products of *Lurmann et al.* [1986]
(100)	$CH_2OO + CH_2O \rightarrow$ products	1.4^{-14}	Recommended rate and products of *Lurmann et al.* [1986]
(101)	$CH_2OO + H_2O \rightarrow CHOOH + H_2O$	4.0^{-18}	Recommended rate and products of *Lurmann et al.* [1986]

TABLE 8. (continued)

Number	Reaction	Rate	Notes*
(102)	$NO + CH_3CHOO \rightarrow NO_2 + CH_3CHO$	7.0^{-12}	Recommended rate and products of *Lurmann et al.* [1986]
(103)	$NO_2 + CH_3CHOO \rightarrow NO_3 + CH_3CHO$	7.0^{-13}	Recommended rate and products of *Lurmann et al.* [1986]
(104)	$SO_2 + CH_3CHOO \rightarrow SO_4^{=} + CH_3CHO$	7.0^{-14}	Recommended rate and products of *Lurmann et al.* [1986]
(105)	$CH_3CHOO + CH_2O \rightarrow$ products	1.4^{-14}	Recommended rate and products of *Lurmann et al.* [1986]
(106)	$CH_3CHOO + H_2O \rightarrow$ products	4.0^{-18}	Recommended rate and products of *Lurmann et al.* [1986]
(109)	$HO_2 + RO_2^a \rightarrow CH_3OOH$	3.0^{-12}	The rate is that suggested by *Lurmann et al.* [1986].
(109b)	$HO_2 + CH_3COO_2 \rightarrow 0.75CH_3OOH + 0.25(CH_3OOH + O_3)$	3.0^{-12}	Products from *Moortgat et al.* [1989*b*]. The rate is that suggested by *Lurmann et al.* [1986].[b]
(110)	$OH + RCHO \rightarrow RCOO_2$[c]	$9.0^{-12}e^{250/T}$	Recommended rate and products of *Lurmann et al.* [1986]
(111)	$NO_2 + RCOO_2 + [M] \rightarrow PPN + [M]$	4.77^{-12} (R81)	The rate is that suggested by *Lurmann et al.* [1986].
(112)	$PPN \rightarrow RCOO_2 + NO_2$	$2.0^{-16}e^{13543/T}$ (R82)	Recommended rate and products of *Lurmann et al.* [1986]
(113)	$NO + RCOO_2 \rightarrow NO_2 + C_2H_5O_2$	$4.2^{-12}e^{180/T}$ (R66)	Recommended rate and products of *Lurmann et al.* [1986]
(114)	$OH + MEK \rightarrow XO_2$	$1.8^{-11}e^{-890/T}$	Recommended rate and products of *Lurmann et al.* [1986]
(115)	$NO + XO_2 \rightarrow NO_2 + CH_3CHO + CH_3COO_2$	$4.2^{-12}e^{180/T}$ (R66)	
(141)	$OH + isoprene \rightarrow PRPYO_2$	$1.5^{-11}e^{500/T}$	Recommended rate and products of *Lurmann et al.* [1986]
(143)	$O_3 +$ isoprene $\rightarrow$ same as O_3+propene (R95)	$7.0^{-15}e^{-1900/T}$	Recommended rate and products of *Lurmann et al.* [1986]
(144)	$N_2O_5 +$ aerosol $H_2O \rightarrow 2HNO_3$	surface area + humidity dependence[d]	

Photolysis Reactions in the Three-Dimensional Model

(PO3)	$O_3 + h\nu \rightarrow O^3P + O_2$	
(PO3D)	$O_3 + h\nu \rightarrow O^1D + O_2$	
(PH2O2)	$H_2O_2 + h\nu \rightarrow OH + OH$	
(PNO2)	$NO_2 + h\nu + O_2 \rightarrow NO + O_2$	
(PHNO3)	$HNO_3 + h\nu \rightarrow NO_2 + OH$	
(PHO)	$CH_2O + h\nu + 2O_2 \rightarrow CO + 2HO_2$	
(PH2)	$CH_2O + h\nu \rightarrow CO + H_2$	
(PNO3)	$NO_3 + h\nu \rightarrow 0.89(NO_2 + O) + 0.11(NO + O_2)$	
(PN2O5)	$N_2O_5 + h\nu \rightarrow NO_2 + NO_3$	
(PHNO2)	$HONO + h\nu \rightarrow NO + HO$	
(PPOX)	$HO_2NO_2 + h\nu \rightarrow NO_2 + HO_2$	
(PCH3CH)	$CH_3CHO + h\nu \rightarrow CH_3O_2 + HO_2 + CO$	
(PCOH)	$CH_3OOH + h\nu \rightarrow CH_2O + OH + HO_2$	
(PMEK)	$MEK + h\nu \rightarrow CH_3COO_2 + C_2H_5O_2$	same as (PHO) (*Carter et al.*, [1979])
(PALD)	$RCHO + h\nu \rightarrow HO_2 + C_2H_5O_2 + CO$	same as (PCH3CH) (*Carter et al.*, [1979])

*Unless otherwise stated, reaction rates or photolysis cross sections and reaction products are from *JPL* [1987].

[a] RO_2 stands for the individual RO_2 species listed in Table 5, with the exception of CH_3O_2 and CH_3COO_2.

[b] The actual product of the dominant branch is $CH_3CO(OOH)$, which is lumped in the mechanism with CH_3OOH.

[c] $RCOO_2$ stands for the peroxy propionyl radical $C_2H_5COO_2$.

[d] The aerosol surface area at the lowest three layers is taken to be 1×10^{-6} cm^2 cm^{-3} according to average continental background conditions [*Whitby*, 1978]. The aerosol surface area is assumed to decrease linearly with height to a value of 1×10^{-8} at the top of tropopause [*Turco et al.*, 1981]. The sticking coefficient is assumed to be 0.05 for relative humidities above 40%, and 0.0 below, according to *Mozurkewich and Calvert* [1988].

hydrocarbon and NO_x conditions typical of a rural site in the eastern United States, minor differences were found between the two mechanisms in terms of OH, RO_2s, O_3, and O_3 production rates (Trainer, unpublished results, 1989), justifying the use of the simplified mechanism for a reasonable range of conditions. The reaction products of terpene oxidation are less well known [*Lloyd et al.*, 1983]. Here we treat the oxidation of the terpenes like that of isoprene. Averaged over the model domain, terpene emissions account for ~30% of the natural NMHC emissions during daylight hours, when NMHC has an influence on O_3 formation. The primary terpene, α-pinene, has an OH reaction rate that is about half that of isoprene. However, more recent natural NMHC emissions estimates (B. Lamb, private communication, 1989) suggest that the isoprene emissions used in this study could be underestimated by a factor of 2 or more. Additionally, isoprene emissions for the grid containing Scotia, Pennsylvania, would have to be at least a factor OF 4 larger than those used in this study to be consistent with observed isoprene levels [*Trainer et al.*, 1987*b*, manuscript in preparation, 1991]. Therefore uncertainties within the emission rates of isoprene dominate any uncertainties associated with the treatment of the oxidation mechanism or reactivity of the terpenes.

TABLE 9. Dominant Species Within NAPAP Lumped Categories [*U.S. EPA*, 1989]

Category	Dominant Species
Alkanes (0.25-0.5)	*n*-butane, iso-butane, 2,2-dimethylbutane
Alkanes (0.5-1.0)	isopentane, *n*-pentane, hexane, pentane isomers, 2,2,4-trimethylpentane, 2-methylpentane
Alkanes (1.0-2.0)	cyclohexane, heptane, C-7 cycloparaffins, methycyclopentane, 2,4-dimethylhexane, octane
Alkanes (>2.0)	*n*-pentadecane, 2-methyldecane, *n*-dodecane
Alkane/aromatic mix	naphtha, mineral spirits
Primary alkenes	butene, 1-pentene, 1-hexene, methyl methacrylate
Internal alkenes	1,3-butadiene, 2-methyl-2-butene, trans-2-pentene
Primary/Internal alkenes	isomers of pentene, C-10 olefins, C-5 olefins
Aromatics (<2.0)	toluene, ethylbenzene, *n*-propylbenzene
Aromatics (>2.0)	*o*-xylene, *p*-xylene, 1,2,4-trimethylbenzene
Others (0.25-0.5)	ethyl alcohol, dimethyl ether, isopropyl acetate
Others (0.5-1.0)	isopropyl alcohol, *n*-butyl acetate, *n*-propyl acetate
Others (>1.0)	glycol ether, propylene glycol, butyl-cellosolve

Numbers in parentheses refer to the OH reaction rate in units of 10^4 ppm^{-1} min^{-1}, and the individual species are ordered according to the contribution by weight.

In keeping with the *Lurmann et al.* [1986] mechanism, organic nitrates are formed from the higher-alkane RO_2 - NO reaction and the NO_3 reactions with propene and isoprene. Within the mechanism, organic nitrates are assumed to be a sink for NO_x with no mechanism for return to reactive nitrogen. *Buhr et al.* [1990] have reported a 1 to 2% NO_y contribution due to C_2 to C_5 alkyl nitrates at the Scotia site, which are expected to have lifetimes greater than 5 days [*Roberts*, 1990; *Atherton and Penner*, 1990]. However, organic nitrates with lifetimes much shorter than a few days certainly exist [*Roberts*, 1990] and may contribute to the 15% of the unaccounted reactive nitrogen observed at the Scotia site [*Buhr et al.*, 1990] as well as other locations [*Fahey et al.*, 1986]. The incomplete treatment of organic nitrates introduces additional uncertainty into the chemical mechanism, particularly with respect to the influence of such species on NO_x and related O_3 formation in rural regions that are influenced by long distance transport from urban activity. However, since the mechanisms and products associated with the removal of many organic nitrates, as well as their relative contribution, are still unknown, this simplistic treatment is somewhat justified.

2.3.3. *The treatment of radiation and photolysis.* Solar radiation and the influence of clouds are considered within the parameterizations of isoprene flux and the photolysis reactions listed in Table 8. The explicit moisture scheme of *Hsie et al.* [1984] allows the cloud water mixing ratios to be determined at each model grid. Following the approach of *Chang et al.* [1987], assuming a mean cloud drop size (10 μm) allows a determination of the optical depth and energy transmission coefficient for each layer. The species dependent correction to the clear sky photodissociation rates are also used from that study to parameterize below-cloud or above-cloud conditions. Multiple cloud levels are treated by assuming a random distribution of cloudiness within each cell, and applying probability fractions to above- or below-cloud conditions based on the percent cloud cover at each grid above and below a given layer. The percentage cloud cover at each layer is parameterized in terms of the relative humidity according to *Geleyn* [1981]. Thus each layer contains a fraction that is clear, a fraction below, and a fraction above cloud, from which the species dependent photolysis corrections of *Chang et al.* [1987] are applied proportionally. Cloudiness influences on the isoprene emissions is estimated by assuming that the spectrally integrated actinic flux is proportional to the NO_3 photolysis rate.

Clear sky photolysis rates are determined by the multiple scattering routine of *Anderson and Meier* [1979] and updated every 30 min. Wavelength dependent photon fluxes, Rayleigh scattering coefficients, and O_3 photodissociation cross sections from *World Meteorological Organization* (WMO) and NASA [1985] are used in the calculations. The stratospheric O_3 distribution [*Dütsch*, 1978] and the temperature profile [*Louis*, 1974] for summertime at 40° N are used as ambient conditions (total O_3 column = 310 Dobson units (DU)). Scattering due to aerosols is also included, with an assumed visual range of 25 km, and appropriate corrections made to the isotropic scattering formalism [*Anderson et al.*, 1980]. The ground albedo is taken to be 0.05, and photolysis rates are calculated for assumed surface elevations of 0, 1 and 3 km for interpolation within the model domain according to orography.

2.4. *Computational Procedure*

Because of limitations on the available core memory of the computer, the time integration of the transport and chemical processes must be calculated independently over the three-dimensional domain. The technique and justification for employing the "time splitting" of chemical and transport operators has been described by *McRae et al.* [1982]. Following this approach, the time integration of equation (1) is performed in the following steps. The chemical production and loss terms are calculated first. The transported and short lived species are integrated over a 150-s time step by the chemical operator. The resulting fields of transported variables are then integrated for a 150-s time step by the transport operator to yield values for an assumed net time step of 150 s. Although consecutive operations of chemistry and then transport are not symmetric with the numerical schemes employed, the resulting fields of chemical species calculated with the order of the operations reversed are essentially identical after several hours of integration.

The tendency due to chemistry is calculated using a modified form of the quasi-steady state approximation (QSSA) method, which has been shown to yield maximum deviations from exact solutions of 1-2% for time steps of 30 s [*Hesstvedt et al.*, 1978]. With our modifications and a time step of 150 s we estimate maximum deviations of <8%, occurring near sunrise or sunset. During other times of the day, predicted concentrations are insensitive to time step sizes less than 150 s.

3. Results of the Model Study

The primary focus of this study deals with the regional aspects of O_3 formation over the eastern United States for a particular 4-day summer time period. We first present the model-predicted O_3 fields, and compare those to available observations taken at various locations within the model domain. We then compare the limited sets of summertime NO_x and NMHC observations with those predicted by the model to confirm that regional variations of the O_3 precursors are also adequately simulated. The model is then used as a diagnostic tool to examine the budgets of O_3 and its precursors for this particular time period within and above the PBL. In contrast to the regional scale aspects of O_3 presented in this work, a companion paper (Trainer et al., manuscript in preparation, 1991) will focus on a comparison of model results with an intensive field study conducted at Scotia, Pennsylvania, during June and July 1986.

3.1. *Comparison of Model and Observed Ozone on a Regional Scale*

The U.S. EPA has organized and operated a network of monitoring stations, originally named SAROAD (Storage and Retrieval of Air Quality Data) but now termed AIRS (Aeronometric Information Retrieval Systems) that dates back to the early 1970s. Measurements of O_3, NO_x, SO_2, NMHC, and other chemical species are available for nearly 200 sites with up to hourly resolution [*U.S. EPA*, 1987]. Since there are questions about the accuracy of the NO_x measurements [*Fehsenfeld et al.*, 1987], and since most of the NO_x and NMHC measurements are confined to urban areas, we focus solely on a comparison with the ozone network which is relatively densely spaced throughout the eastern United States.

As was mentioned previously, the model-derived O_3 at nighttime is an average of the lowest 78 m and is not representative of surface concentrations that are controlled by surface deposition and reduced vertical mixing during the nocturnal inversion. Furthermore, the photochemical formation of O_3 is correlated with solar insolation, so afternoon O_3 concentrations generally reflect the net photochemistry occurring throughout the daylight period. We therefore restrict our

comparison to afternoon conditions and compare O_3 mixing ratios averaged from 1 to 5 p.m. EST for the last 3 days of model simulation. In using the AIRS ozone network data, caution must also be taken in making comparisons since the model predicts grid averaged quantities, and there is some concern about how representative a particular measurement is for a larger area [*Schere*, 1988]. Also, measurements taken in or near urban areas, which comprise a significant fraction of the total data, may be seriously influenced by local chemistry such as titration effects by locally emitted NO. Realizing these limitations to the observed data, we have eliminated all measurements classified by AIRS as "city center" but kept all "suburban" and "rural" data regardless of distance from urban centers. Also, a station was eliminated from the observed data set if any of the 1 p.m. to 5 p.m. hourly-averaged values were missing. These are the only filters applied to the observational data.

The main reason for choosing the particular time period of July 4 to July 7, 1986, is because the synoptic conditions show a clear anticyclonic system that favors the photochemical production of O_3. A low-pressure system had just passed through the eastern seaboard on July 3, 1986, essentially displacing any previously formed O_3 as the front moved northeastward over the Atlantic. The observed maximum O_3 values for July 3, 1986, were all less than 60 ppb throughout the domain with no organized spatial structure. On July 4, 1986, O_3 values began to rise as a center of high pressure began to build over the eastern Ohio River valley. At 0000 UT, July 4, 1986, the model calculations begin with an imposed O_3 initial condition of 30 ppbv throughout the domain. Figure 4 shows the initial conditions, as well as the continental area 1-5 p.m. EST averaged O_3 predicted by the model for the 4 different days of the model simulation. Most of the O_3 increase occurs in the first 44 hours of model start-up. During the final 36 hours of simulation, the average O_3 does not change, but significant horizontal variations arise from the changing synoptic weather conditions.

Plates 1*a* through 1*d* show the observed and calculated 1 to 5 p.m. EST average O_3 mixing ratios for the last 2 days of the model simulation (July 6 and 7, 1986). It should be noted that the depiction of the observed O_3 fields in Plates 1*a* and 1*c* have some interpolated regions in southern Canada and over bodies of water, particularly the Atlantic Ocean where there are no observations. Locations of the observations are noted in these figures by dark blue crosses (suburban measurement sites) and circles (rural sites). The model O_3 fields shown in Plates 1*b* and 1*d* comprise all of the calculated points, including the oceanic values. For the observed O_3 distributions in Plates 1*a* and 1*c*, isolated stations can influence local gradients as well as the regional pattern. It is therefore necessary to keep in mind that visual comparison should be done over general regions, and with regard to the number of stations influencing the contours of the observed data.

In the region where the boundary influence is minimal (roughly eight or nine grid cells away from model borders), several important features are reproduced fairly well. For example the southern extent of the contours from the main body of high O_3 are fairly well simulated east of Illinois and north of Alabama on days 3 and 4. Agreement between the position (Chesapeake Bay to southern New Jersey, southern Connecticut) and magnitude of the highest O_3 values (>100 ppbv) is also apparent on these days. Both model and observations show a tendency for a southern migration of the ozone maximum from the Long Island region to the Chesapeake Bay area from day 3 to day 4. The movement of the cold front associated with the low-pressure system located along the northern border is the most obvious feature borne out in both the observations and model; however, local differences are

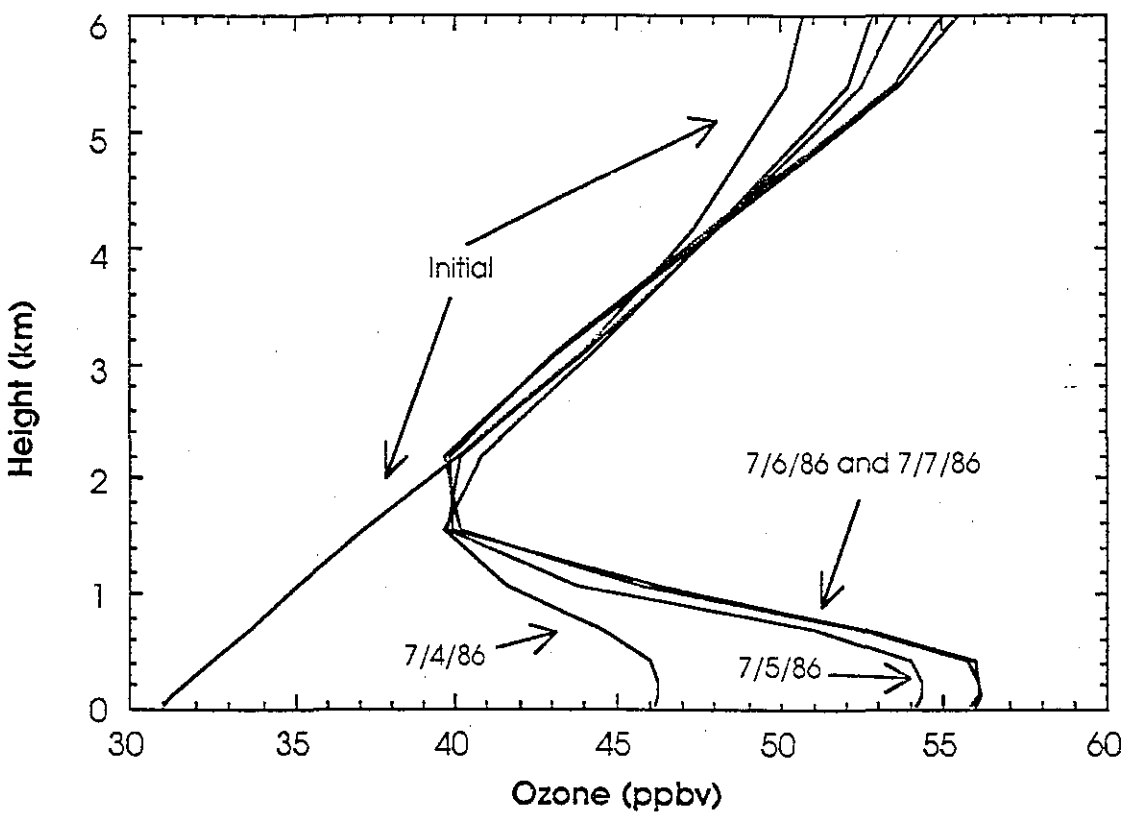

Fig. 4. The vertical distribution of the initial O_3 and 1-5 p.m. EST, continental area averaged O_3 for the 4 days of model simulation.

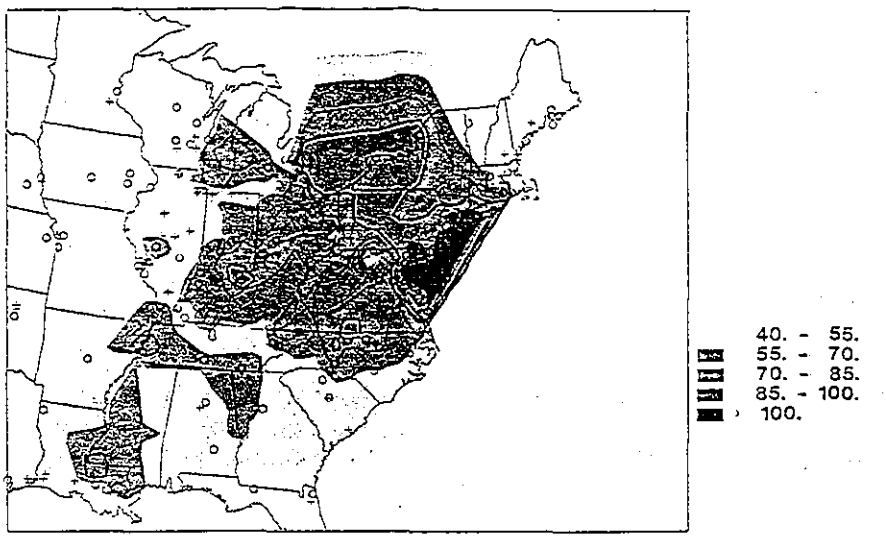

Plate 1*a*. The 1-5 p.m. EST average observed O_3 for July 6, 1986. Locations of the observing stations are shown by crosses (suburban locations) and circles (rural locations). Units of O_3 are in parts per billion by volume. Interpolated regions over Canada and the Atlantic Ocean or with sparse observations should be ignored.

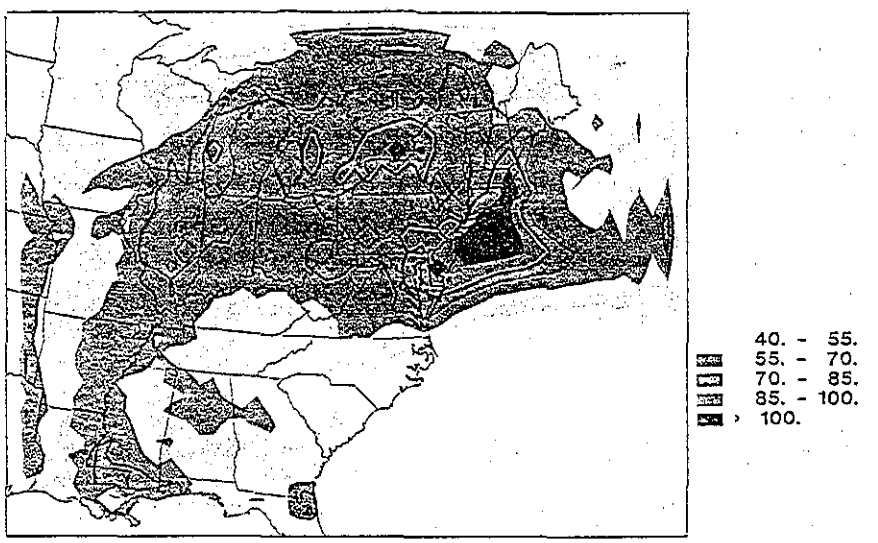

Plate 1*b*. Model-predicted 1-5 p.m. average O_3 for July 6, 1986, and the lowest model layer.

apparent due to uncertainties in predicting the exact location of the frontal edge. The influence of the front appears to be somewhat farther south over New York, Vermont, and New Hampshire, while the model shows an influence at the eastern edge of the cold front on day 4 that advects air with high O_3 values northward directly over Maine. The one region strongly influenced by coastal inflow (the Carolinas, Georgia, and Alabama) that is characterized by relatively low O_3 is also well simulated for both days.

When one examines the regions of O_3 overprediction and underprediction, certain aspects of the comparison become more obvious. Figures 5*a* and 5*b* show the overprediction and underprediction, respectively, for the July 6, 1986, data depicted in Plates 1*a* and 1*b*. O_3 is significantly overpredicted by the model along the eastern seaboard north of Long Island and also over a broad region extending from the Kansas-Nebraska border through Illinois and Wisconsin into eastern Michigan. Coastal locations along the southern model border are also consistently overpredicted. Regions of significant underprediction are south of Long Island and east of the Mississippi river, and most pronounced along the Ohio River valley and throughout North Carolina. The O_3 overpredictions and underpredictions for July 7, 1986, are very similar to those shown in Figures 5*a* and 5*b*, with the exception of the eastern Wisconsin and southern Lake Michigan sites changing to slightly underpredicted, and an increase in the overprediction for most sites in eastern Michigan, Ohio, and northern New York.

Several factors are undoubtedly contributing to the patterns of model overprediction and underprediction noted above. The inability of the dynamical model to correctly predict certain meteorological features, such as the exact position of the front along the northern U.S. boundary, may explain part of the discrepancies. A tongue of enhanced O_3 was observed to extend into the Carolinas on day 4, but the model predicts only a slight southwestward enhancement. This is a region where model and observed winds show significant differences. Referring to Figures

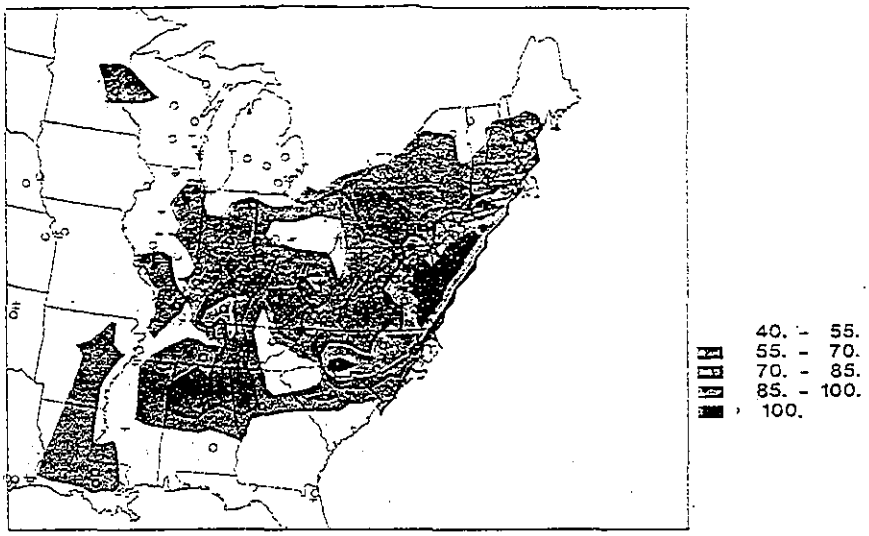

Plate 1c. The 1-5 p.m. EST average observed O_3 for July 7, 1986. Locations of the observing stations are shown by crosses (suburban locations) and circles (rural locations). Units of O_3 are in parts per billion by volume. Interpolated regions over Canada and the Atlantic Ocean or with sparse observations should be ignored.

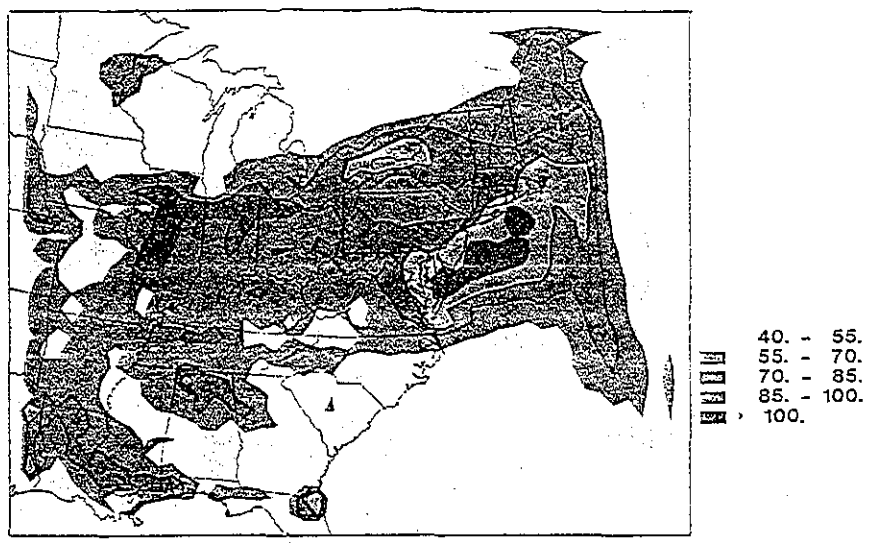

Plate 1d. Model-predicted 1-5 p.m. average O_3 for July 7, 1986, and the lowest model layer.

2*a* and 2*b*, the 880 mbar observed winds at 0000 UT July 7, 1986, show a northwesterly component over West Virginia, and a westerly component over the areas of highest O_3 in North Carolina, suggesting that the Ohio River valley is an upwind source of pollutants in this region. The model predicts southerly or southeasterly flow over much of North Carolina, with southwesterly flow over West Virginia that forces air from the Ohio River valley northward over Chesapeake Bay.

A significant underprediction also exists along the highly populated eastern seaboard south of Long Island that cannot be attributed to discrepancies in the predicted wind field. As will be discussed later, with regard to the budget and photochemical generation of O_3, this is a region where the NAPAP emissions inventory underpredicts observed NMHC to NO_x ratios by nearly a factor of 4. We have performed a calculation with anthropogenic NMHC increased uniformly by a factor of 4 to test the sensitivity of O_3 to this uncertainty. For these conditions, the model overpredicts all but two points in this region, but also adds to the overprediction at lower observed O_3. Nonetheless, the model underprediction in the urbanized eastern seaboard could certainly be explained by an underestimation in the anthropogenic NMHC emissions in this region. Alternatively, since highly reactive aromatic and alkene species are lumped into less reactive categories within the chemical mechanism, there is a possibility that part of the underprediction is related to model's treatment of these species. However, as the preceding discussion demonstrates, discrepancies between observed NMHC to NO_x ratios for urban areas and those derived with the emissions inventory preclude our ability to attribute the O_3 underestimation to possible deficiencies in the chemical mechanism.

Another factor contributing to the model discrepancies, possibly related to the two main regions of overprediction, is the absence of vertical transport from subgrid-scale cumulus convection within the model formalism. A comparison of Figure 5*a* with Figure 2*c* shows that much of the overprediction in the midwest is coincident with or ahead of the cloudiness and cold front in the

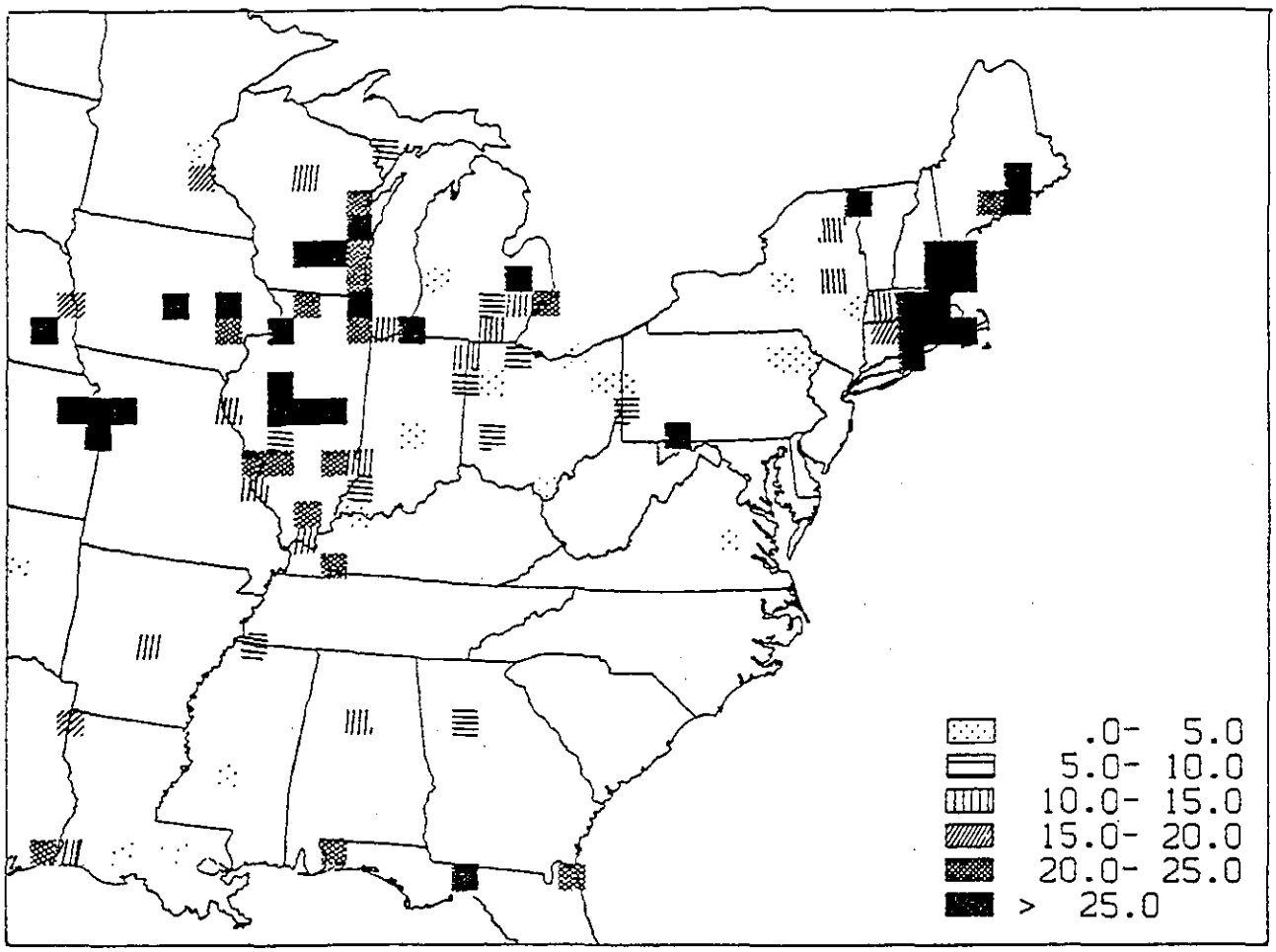

Fig. 5*a*. Model-predicted minus observed 1-5 p.m. averaged O_3 for July 6, 1986 (ppbv).

northwest portion of the model domain. Similarly, the region of overprediction north of Long Island coincides with the warm front and associated cloudiness in the northeast United States and southeastern Canada. The main regions of overprediction for July 7, 1986, also coincide with predicted areas of cloudiness. Although we have relied on the premise that convective cumulus transport should be minimal under high-pressure systems, the coincidence of cloudiness and O_3 overprediction suggests that neglecting this transport process may compromise the ability of the model to accurately predict O_3, particularly along the frontal boundaries of the high-pressure system. It should be noted that all sites in Illinois overpredict O_3, while from Figure 2*c* Illinois should be well southward of the cold front. However, NMC radar summaries, surface analysis and visible satellite images for July 6, 1986, show that cloudiness extended from western Arkansas and Texas through the western two thirds of Missouri and northward to middle Minnesota, patchy clouds were present over much of eastern Arkansas and southeastern Missouri, and rain occurred over the northern half of Illinois between 1900 and 2300 UT. The dynamic model inherently underpredicts the cloudiness along the western border owing to the formulation of the boundary conditions, which is one possible factor contributing to the higher than observed O_3 values along the western border in Plates 1*b* and 1*d*. Another factor that significantly influences the western portion of the model is the predicted PBL heights from the dynamic model. Because of uncertainties in specifying the PBL height at the borders, it was simply fixed at 100 m on all boundaries. This underestimation for the western boundary propagates four or five grid cells into the domain and has the tendency to concentrate O_3 in the lowest layer by suppressing vertical exchange. The dynamic model also predicts very shallow PBL depths (<300 m) over most of Illinois and northwest Indiana, extending northeastward through Michigan between 1900 and 2300 UT on July 6, 1986, which is largely responsible for the high (>70 ppb) surface O_3 values shown in Plate 1*b* for this region. Since the observations indicate that significant cumulus activity developed throughout Illinois before and during this same time period, the model undoubtedly underpredicts the vertical exchange that occurred. Obviously, further model simulations that include reliable parameterizations of the convective cumulus transport process are necessary to assess its impact. The O_3 overprediction along the southern coast is quite possibly due to the model's inability to accurately predict the PBL height and resolve the local land-sea air circulation for coastal locations. These features, as well as other subtleties of the meteorological situation, are not expected to be reproduced precisely by the dynamical portion of the model.

Additional factors could also contribute to the model discrepancies. As was mentioned earlier, we have used average weekday emission rates, while July 4-7, 1986, was a holiday weekend. Although differences in NO_x and NMHC emissions between a typical summer weekday and a Sunday are only ~20% on the average, a July 4 weekend may not be typical of any classification. However, preliminary calculations with decreased

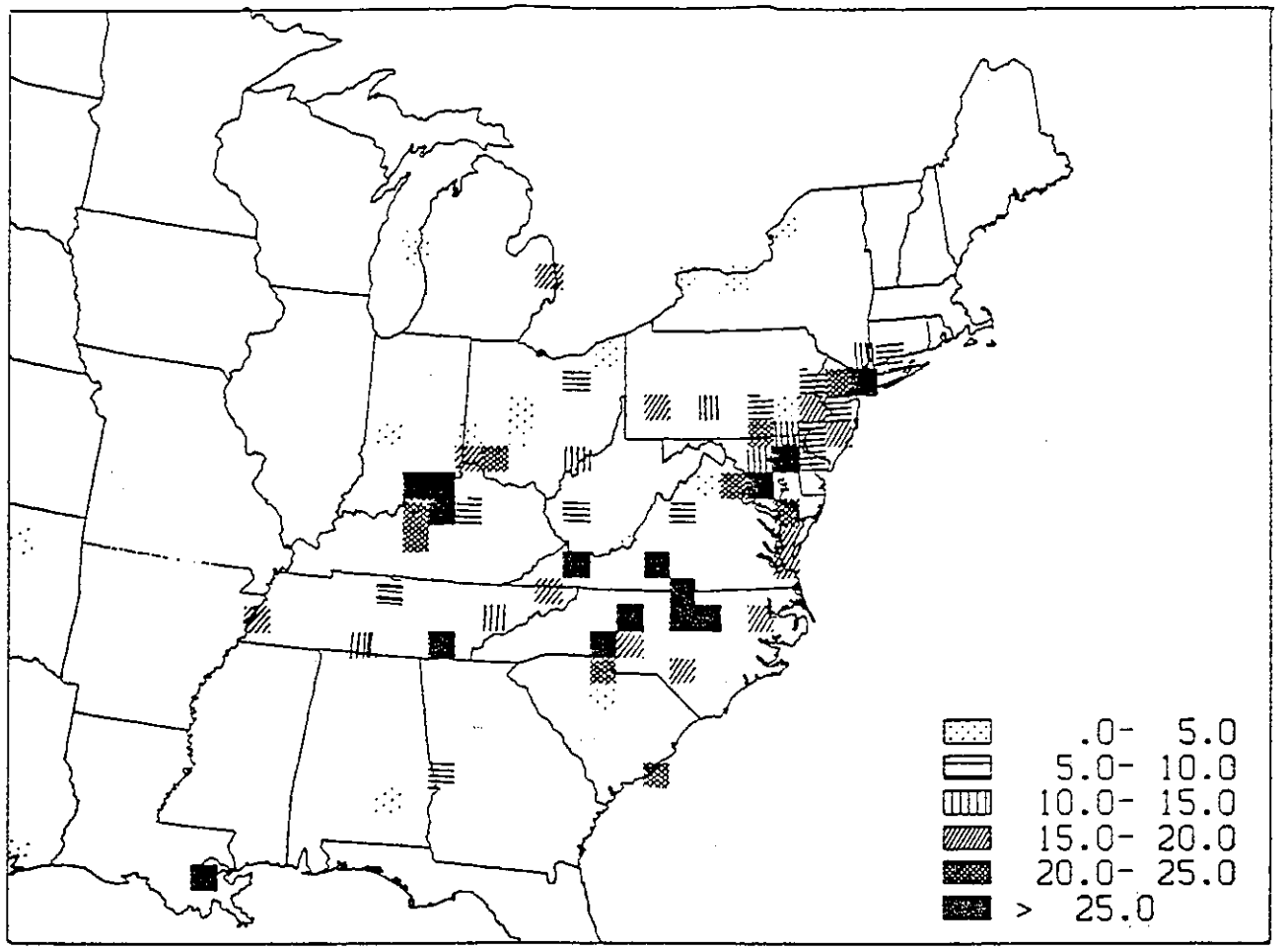

Fig. 5b. Observed minus model-predicted 1-5 p.m. averaged O_3 for July 6, 1986 (ppbv).

anthropogenic emissions in NO_x and NMHC indicate that a significant decrease in the model predicted O_3 for the western half of the model domain requires more than a 50% reduction in both these precursors. The possibility of clean air O_3 overproduction cannot be excluded. *Parrish et al.* [1986] and *Perner et al.* [1987] have suggested that photochemical models in general may inherently overpredict peroxy radical and OH concentrations. *Sillman et al.* [1990] have also shown that regional scale models can overpredict O_3 owing to a combination of low model resolution and nonlinearities in the O_3 production [*Liu et al.*, 1987]. An investigation of this possible influence with a higher resolution, nested model domain is planned for future work. Other factors, such as the influence of boundary conditions, the relatively high numerical diffusion associated with the Smolarkiewicz advection scheme, and the parameterization of vertical transport (particularly at night) could also be affecting the results. Further refinements and sensitivity studies related to these aspects of the model are also anticipated.

In order to obtain information on the reliability of the model O_3 predictions, simple statistical analysis of matching data as well as variations in the observed data need to be considered. For point by point comparisons, we assume a single measurement occurring within a grid cell is representative of the grid cell, and two or more measurements occurring within a model grid cell are averaged. Figures 6*a* through 6*c* illustrate the point by point comparison of model versus observed O_3 averaged from 1 to 5 p.m. EST for July 5, 6, and 7, with exact correspondence denoted by the dashed line. Both the model and observations show a marked increase in the number of points exceeding 85 or 90 ppbv from day 2 to day 3. The model shows a distinct tendency to overpredict at low observed O_3 and underpredict at the high end on all three days of the simulation. Table 10 gives the correlation coefficients, and other statistical relationships in relation to Figures 6*a* to 6*c*. With the large number of comparable points (~155) the correlations between model and observations (0.54 to 0.58) are significant above the 99.9% confidence level on all 3 days. Although there is little difference between the observed and modeled O_3 mean values on day 2, a 3- to 4-ppb difference is apparent on days 3 and 4. When one looks at the fraction of points predicted accurately within specific limits, the model performance appears to be best on day 2, which is probably an artifact of the model O_3 bias evident in the mean values. However, nearly 50% of the comparisons are within 15 ppbv or 25% on the last 2 days of simulation.

The general characteristics of model performance shown in Figures 6*a* through 6*c* and the statistical quantities given in Table 10 can be compared with two previous three-dimensional studies of O_3 in the northeastern United States. An analysis of calculated versus observed O_3 for the summertime northeast United States by *Liu et al.* [1984] resulted in a correlation coefficient of 0.7. However, only nine stations were compared over an 8-day period, and data for all hours of the day were considered. The four-level model used in the study incorporated a height varying surface layer, so a portion of the stated correlation arises from adequately

simulating the nighttime inversion, when O_3 concentrations are small at the surface. Analogous to our results shown in Figure 6, the Liu et al. simulations tend to overestimate O_3 when observed O_3 is low, and underestimate O_3 when observed O_3 is high [*Morris et al.*, 1988]. The authors attribute the overprediction to the fact that the O_3 monitoring sites used in the comparison were close to forests, and the model was unable to account for the high deposition rates during night. Overprediction was also noted during daylight hours under cloudy or rainy skies at individual sites. Underpredictions for high O_3 observations were attributed to comparing large volume averages obtained by the model with point measurements within subgrid-scale ozone plumes that the

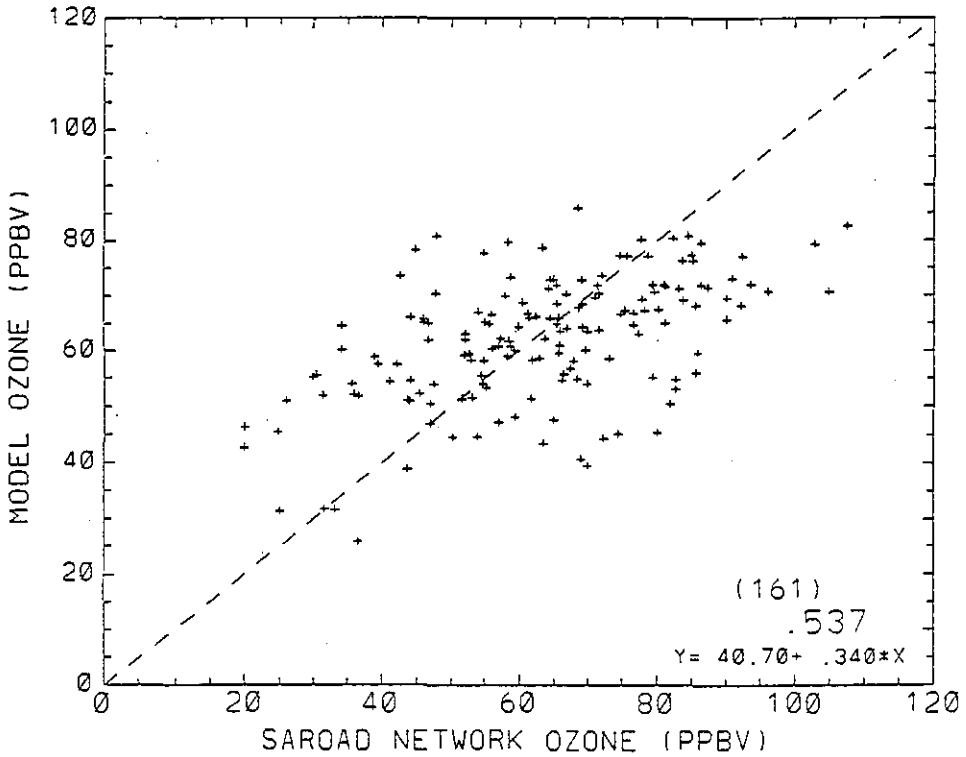

Fig. 6*a*. Scatter plot of model-predicted versus observed O_3 averaged from 1 to 5 p.m. EST on July 5 1986.

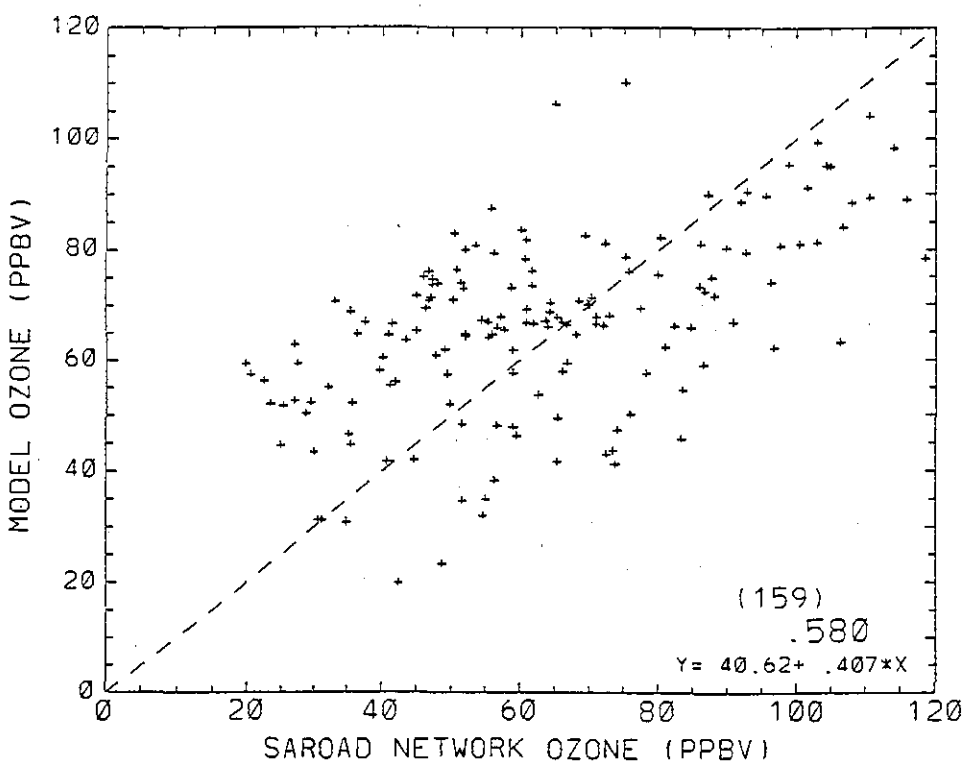

Fig. 6*b*. Scatter plot of model-predicted versus observed O_3 averaged from 1 to 5 p.m. EST on July 6, 1986.

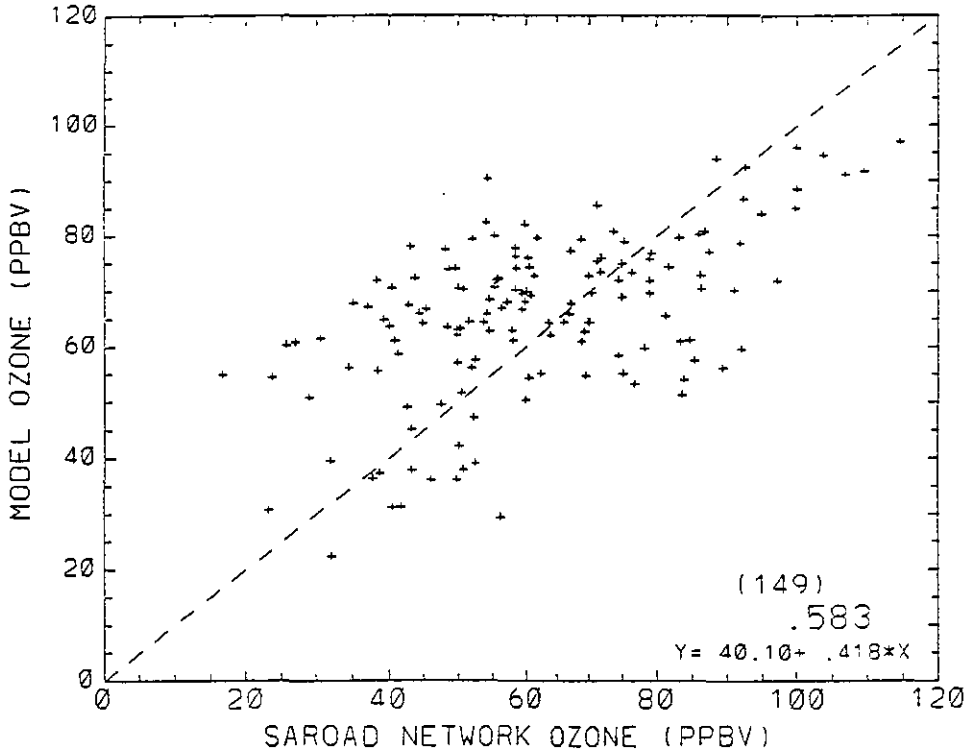

Fig. 6c. Scatter plot of model-predicted versus observed O_3 averaged from 1 to 5 p.m. EST on July 7, 1986.

model cannot resolve. The same pattern of overprediction and underprediction has been observed with the EPA/NOAA regional oxidant model (ROM) [*Lamb*, 1988; *Schere and Wayland*, 1989], which also simulates northeast U.S. summertime ozone, but with a 20×20 km^2 grid and four vertical layers. By analyzing the statistical distribution of observed and model O_3 for locations near urban sources, remote sites, and intermediate sites, the authors note that underprediction of high O_3 is characteristic of those locations near urban sources, due to the inability of the model to simulate subgrid-scale urban plumes. Although overprediction for low O_3 is characteristic of all three site classifications, it is most pronounced for the remote locations. The authors attribute this to uncertainties in specifying the boundary conditions of O_3.

Although a correlation coefficient of 0.58 is significant, it implies the model can only explain a limited amount (~34%) of the variation in the observed data. This becomes quite apparent when one examines the variation in the observed data itself. Figure 7 shows the absolute difference between calculated and observed 1-5 p.m. average O_3 versus the range of observed values (observed O_3 maximum minus the observed O_3 minimum) for the corresponding grid cell for day 4. The range of observations include all of the hourly O_3 observations over the 4-hour period and all stations (if more than one) within a model grid. The various numbers indicate the number of AIRS sites within each grid cell. The median range in hourly averaged observed O_3 is 21 ppb, but in extreme cases, the range can exceed 50 ppb over a 60×60 km^2 area and 4-hour time period. Apparently, the observational data set can be seriously influenced by subgrid-scale processes such as the proximity and relative location to urban areas, topographic characteristics of the site, and other factors the model is unable to resolve. Although Figure 7 does not provide information on the origins of the observed variability, some qualitative inferences can be drawn. Model grids containing only one station generally have a smaller range than grids with two or more stations, which suggests that in general the spatial variability within a 60×60 km^2 grid may influence the total variability more than the temporal variability. However, there are several grids with only one monitoring station that have a range between 40 and 60 ppbv, so isolated instances of high temporal variability can sometimes occur. Figure 7 also shows that the more monitoring stations within a given model grid, the better the model predicts 1-5 p.m. average O_3. Therefore because of the variability in the observations, a moderate correlation coefficient of 0.58 is probably as good as can be expected. The fact that an equivalent and significant correlation exists for the last 3 days of simulation suggests that some general aspects of the model, such as the meteorology and the location and magnitude of the O_3 source regions, roughly correspond to the actual situation.

TABLE 10. Calculated and Observed Ozone Statistics

	July 5, 1986	July 6, 1986	July 7, 1986
Number of Comparison Points	161	159	149
Calculated mean O_3	62.2 ± 11.3	66.6 ± 16.7	66.1 ± 14.8
Observed mean O_3	63.1 ± 17.9	63.7 ± 23.8	62.4 ± 20.6
Correlation Coefficient	0.54 ± 0.05	0.58 ± 0.05	0.58 ± 0.05
Fraction predicted better than 15 ppb	0.66	0.49	0.58
Fraction predicted better than 20%	0.63	0.45	0.48
Fraction predicted better than 25 ppb	0.87	0.74	0.83
Fraction predicted better than 33%	0.77	0.60	0.72

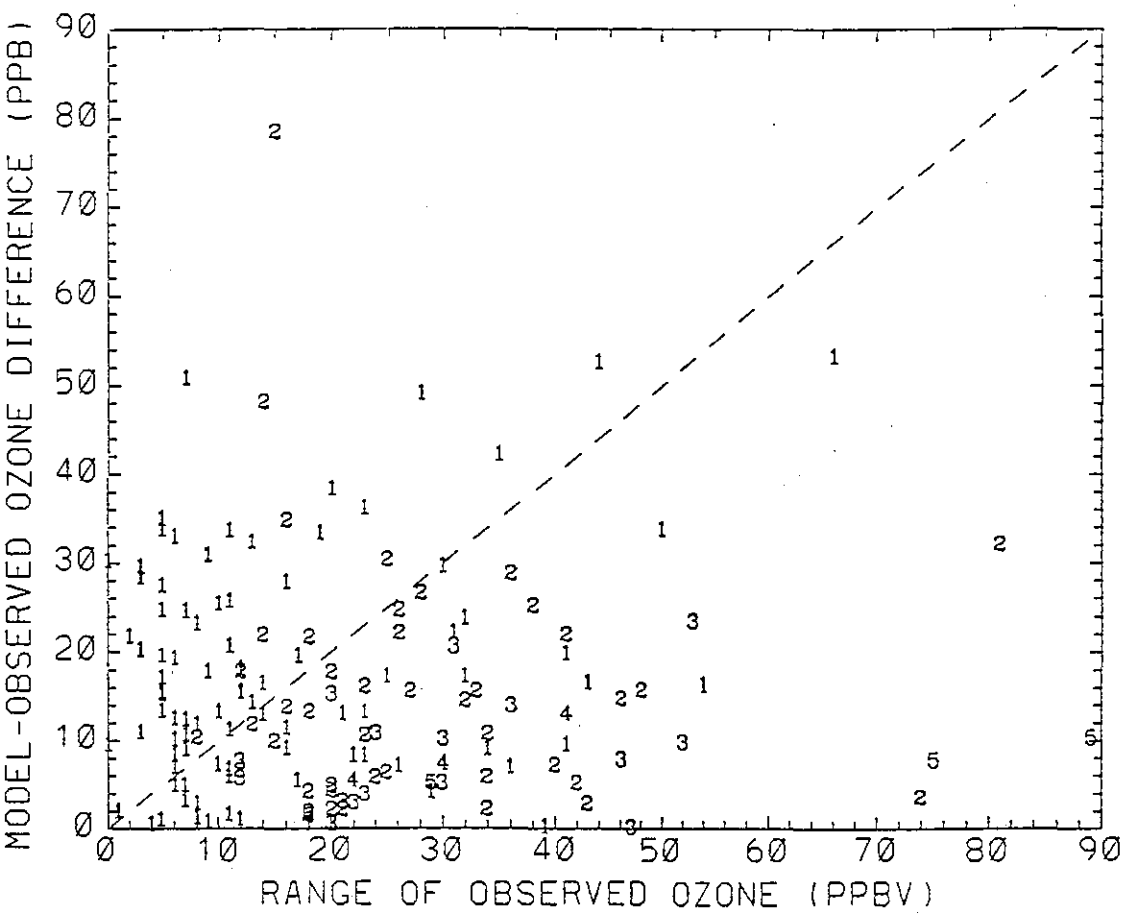

Fig. 7. Scatter plot of the difference between model-predicted and observed O_3 averages from 1 to 5 p.m. EST on July 7, 1986, versus the range of hourly observations over that 4-hour period, and over all observing locations within a model 60×60 km grid. Numbers indicate the number of locations within the 60×60 km model grid used in the analysis.

3.2. *Distributions of Ozone Precursors*

Since the O_3 distribution and the photochemical O_3 production depend critically on the distributions of O_3 precursors, namely NO_x and NMHC [e.g., *Fehsenfeld et al.*, 1983], it is important to correctly model their distributions. Comparison of the model calculated distributions of the precursors to observed values is also an important test for the photochemical and transport processes in the model. We compare calculated values with measurements when it is possible. Unfortunately, measurements of NO_x and NMHCs in the rural areas in the eastern United States are scarce [*Fehsenfeld et al.*, 1988; *Greenberg and Zimmerman*, 1984]. On the other hand, measurements in the urban and suburban areas are of limited use for comparison with our model because of the coarse resolution in the model.

The distribution of NO_x is particularly important because O_3 production is usually NO_x limited outside highly polluted areas [*Fishman et al.*, 1979*b*; *Logan et al.*, 1981; *Liu et al.* 1987]. Plate 2 shows the lowest layer NO_x distribution averaged from 9 a.m. to 5 p.m. EST for July 6, 1986. Mixing ratios correlate highly with the emissions shown in Figure 3*a*, with regional maxima along the eastern seaboard and the Ohio River valley. Summaries of rural NO_x measurements made to date are given by *Altshuller* [1986] and *Fehsenfeld et al.* [1988], and a synopsis of NO_x measurements taken during SURE is given by *Logan* [1989]. There are several ground-based NO_x measurement programs that coincide with the time of year and region of the model scenario, from which we can examine monthly to seasonally averaged NO_x observations and compare with the model-predicted NO_x as a check on qualitative agreement. As was pointed out by *Fehsenfeld et al.* [1987, 1988], the hot molybdenum and ferrous sulfate converters used to convert NO_2 to NO in nearly all the observations are not specific to NO_2, making the measurements subject to interferences from PAN, *n*-propylnitrate, HNO_3 (in the case of molybdenum converters) and other nitrogen-containing species. Therefore most measurements used in the comparison are probably representative of NO_x+PAN rather than NO_x. Also, because of the strong diurnal dependence of NO_x [*Fehsenfeld et al.*, 1988; *Logan*, 1989] due to changes in the PBL height and photochemical reactions, only afternoon averages are compared.

Table 11 summarizes published 1-5 p.m. EST averaged observed NO_x with model-calculated NO_x and NO_x + PAN averages of the corresponding grid averaged over the last 3 days of simulation. Of the 13 points compared, only 3 show good agreement (better than 25%), while 2 seriously overpredict, and 8 underpredict the observed average NO_x. Although the NO_x observations are highly variable (1σ standard deviations of 60 to 90% of the mean values), the model overpredictions and nearly half of the underpredictions are significant. Clearly, there are difficulties with comparing averages of a 3-day period with monthly or seasonal averages, but most of the model-derived NO_x + PAN values have little day to day variation. The Indian River, Delaware, site is close to the Atlantic coast and can be expected to be influenced meteorologically by occasional on-shore flow. Within the model, the corresponding grid is influenced by

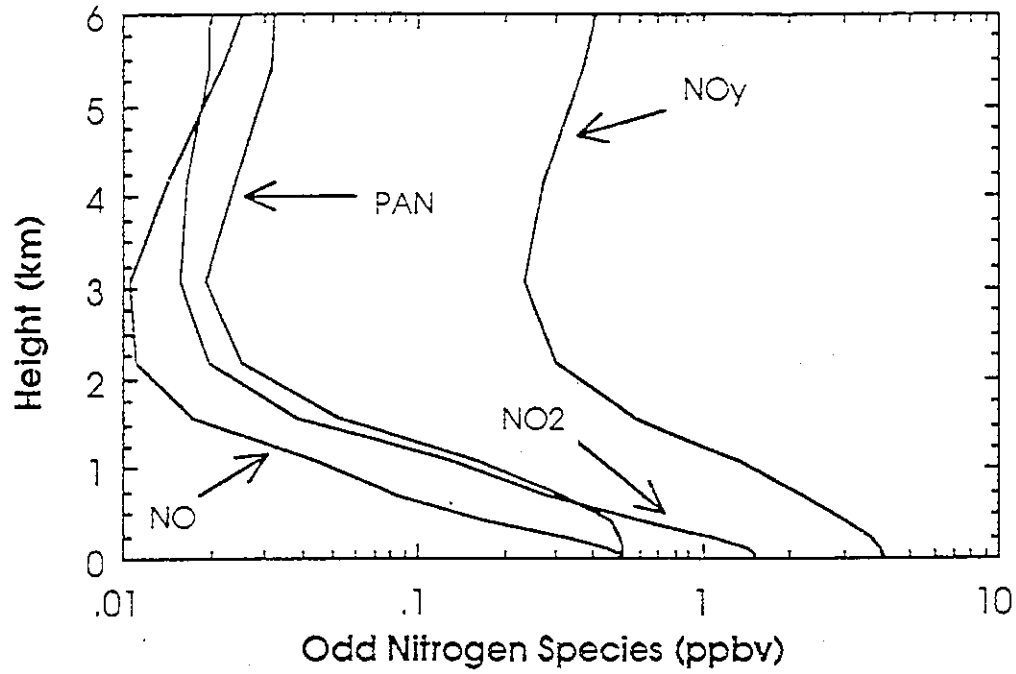

Fig. 8. The vertical profiles of nitrogen compounds and O_3 averaged from 9 a.m. to 5 p.m. EST on July 7, 1989, and also averaged over the continental region of the model domain.

predominantly westerly and northwesterly flow over the 4-day period, and as a consequence, one of the overpredicted sites. The observed value at the Fort Wayne, Indiana, site seems spuriously low, since the summer average NO_x observations of an extremely remote site (40 km WNW of Pierre, South Dakota) with a similar instrument are a factor of 2 higher [*N. A. Kelly et al.*, 1984]. The eight sites for which NO_x+PAN is underpredicted can simplistically be explained by local NO_x sources not resolvable by the model. However, the six locations most seriously underpredicted are from the SURE study, in which the measurements are additionally biased by a 2-ppbv detection limit [*Logan*, 1989], and possible HNO_3 interferences from the molybdenum NO_2 converters [*Winer et al.*, 1974]. The one measuring program operational during July of 1986 at Scotia, Pennsylvania, shows very good agreement for NO_x and about a 50% underprediction for PAN (Trainer et al., manuscript in preparation, 1991). The average NO_x+PAN underprediction, excluding the Scotia and the two overpredicted comparisons, is 54%. Considering the limitations of most of the observed data, and the nature of the comparison, this difference would still fall within the expected uncertainty limits. Obviously, a sufficiently dense and reliable rural NO_x data set, coincident with the period of model simulation, is necessary to reduce the uncertainty in such a comparison.

TABLE 11. Comparison Between Modeled and Observed NO_x

Site	Latitude, Longitude	Observation Dates	Observed[a] NO_x	Model[a] NO_x+PAN	Model[a] NO_x
Montague, Mass.[b]	42.55, 72.55	Aug. 1, 1977, to Dec. 31, 1979	2.75	2.28	1.28
Scranton, Pa.[b]	41.38, 75.67	Aug. 1, 1977, to Dec. 31, 1979	6.05	1.80	0.92
Indian River, Del.[b]	38.67, 75.25	Aug. 1, 1977, to Dec. 31, 1979	2.08	5.21	3.27
Duncan Falls, Ohio[b]	39.83, 81.83	Aug. 1, 1977, to Dec. 31, 1979	3.85	2.02	1.16
Rockport, Ind.[b]	37.92, 87.05	Aug. 1, 1977, to Dec. 31, 1979	8.97	5.2	4.49
Giles County, Tenn.[b]	35.21, 87.03	Aug. 1, 1977, to Dec. 31, 1979	5.33	1.42	0.58
Fort Wayne, Ind.[b]	41.08, 85.17	Aug. 1, 1977, to Dec. 31, 1979	0.49	1.39	0.59
Research Triangle Park, N. C.[b]	35.87, 79.10	Aug. 1, 1977, to Dec. 31, 1979	7.00	1.56	0.72
Lewisburg, W.Va.[b]	37.78, 80.45	Aug. 1, 1977, to Dec. 31, 1979	3.48	1.08	0.73
Whiteface Mt., N.Y.[c]	44.38, 73.85	July 1, 1982, to July 29, 1982	1.24	1.46	0.72
Shenandoah Natl. Park, Va.[d]	38.67, 78.47	July 14, 1980, to Aug. 15, 1980	1.98	1.14	0.41
Abbeville, La.[d]	29.97, 92.13	Aug. 5, 1979, to Sep. 11, 1979	2.96	1.47	1.37
Scotia, Pa.[e]	40.78, 77.95	June 25, 1986, to July 26, 1986	1.18[f]	2.20	1.29

[a]All NO_x and PAN values are in ppbv and are 1 to 5 p.m. EST averages over the time period of observations. Because of the probability of PAN interference in all measurements except at the Scotia, Pennsylvania, site [*Fehsenfeld et al.*, 1988], the observations should be compared to the model NO_x and PAN.

[b]SURE study, *Mueller and Hidy* [1983]. Only the July averages given by *Logan* [1989] are presented here.

[c]*T. J. Kelly et al.* [1984]. Whiteface Mountain is ~1.5 km above sea level, and the model terrain elevation is 440 m. Model values at the model surface are given. At ~1.5 km above sea level, model values of NO_x and NO_x+PAN are 0.12 and 0.36 ppbv, respectively.

[d]*N. A. Kelly et al.* [1984].

[e]*Fehsenfeld et al.* [1988].

[f]The Scotia site observations are strictly NO_x. The observed NO_x + PAN at Scotia, Pennsylvania, was 2.13 ppbv.

The land area averaged vertical profiles for odd nitrogen compounds NO, NO_2, NO_y, and PAN are shown in Figure 8. Height profile measurements of NO_x are essential for evaluating the vertical transport processes and NO_x within the model. Unfortunately, there are only limited observations of the vertical distribution of NO_x over the eastern United States available in the open literature. Vertical profiles of NO_x made during the SURE study [*Blumenthal et al.*, 1984] were measured with instruments having too high a detection limit (~1 ppbv) to be of use in comparison and are only published as annually averaged values. NO_y from two flights between Columbus, Ohio, and Saranac Lake, New York [*Boatman et al.*, 1990], show decreasing mixing ratios with height, reaching 1 ppbv between 800 and 700 mbar with values between 1.5 and 8 ppbv within the PBL. Averaged from 37° to 42° latitude and 76° to 84° longitude, the model-derived NO_y reaches 1 ppb at 2 km or ~780 mbar, with PBL averages of about 5 ppb. These values are in fair agreement with the Boatman et al. observations. The few flights over the western continental United States measuring NO_2 and NO with reliable instruments through the Global Tropospheric Experiment (GTE) [*McNeal et al.*, 1983; *Beck et al.*, 1987] are specific to particular synoptic conditions, as are the model-predicted NO_x profiles. Below about 2.5 km, the NO_y profile in Figure 8 is qualitatively consistent with continental GTE measurements (G. Hübler et al., Airborne measurements of total reactive odd nitrogen (NO_y), submitted to *Journal of Geophysical Research*, 1990) and the midwest observations of *Pickering et al.* [1988], decreasing a factor of 4.5 between 1 and 2.5 km, with a minimum observed at about 2.5 km altitude. A C-shaped NO profile for air masses of continental origin with a minimum occurring above 2 km is also commonly observed [*Drummond et al.*, 1988].

In terms of the partitioning of the NO_y species, Figure 8 shows that NO_x accounts for about 15% of the NO_y at 1 km and decreases to about 8% above 3 km. This is somewhat lower that the mean of 15% for continental air masses over the southwestern United States obtained from CITE measurements between 1 and 5 km altitude (G. Hübler et al., manuscript in preparation, 1991). However, the model does not include heterogeneous loss of HNO_3, which could influence this quantity at these altitudes. At the surface, NO_x, PAN, and HNO_3 account for 50, 10, and 38%, respectively, of the NO_y when averaged from 9 a.m. to 5 p.m. and over the continental regions of the model domain. In comparison, the median fractions of *Fehsenfeld et al.* [1988] (Scotia, Pennsylvania, summer 1986) give 38, 21, and 24% for the same species averaged over the same time period. The PAN to NO_x ratio is strongly influenced by temperature, which diminishes the usefulness of a comparison with average model conditions (it has already been shown, in the NO_x comparison study, that for the model grid box containing Scotia, average NO_x agrees very well). However, the model average PAN÷NO_x fraction of NO_y is exactly the median fraction sum of PAN and NO_x that is observed. Additionally, within the observations the sum of the median fractions does not equal the median of the fraction sums, and the larger than observed HNO_3 to NO_y fraction may be indicative that the neglect of HNO_3 removal processes in the model could be influencing these ratios near the surface as well.

To see qualitatively how representative the model is for regional-scale NMHC concentrations, we compare summertime rural measurements averaged over a few weeks or a month to averages from the corresponding model grid in a manner similar to the NO_x comparison. The studies of *Sexton and Westberg* [1984], *Singh et al.* [1981] and *Seila et al.* [1984] report individual NMHC concentrations within our model domain and qualify as both rural and long-term (>3 weeks). The study of *Sexton and Westberg* [1984] includes NMHC measurements taken near Belfast, Maine, and Robinson, Illinois, averaged from 6 to 9 a.m. However, at the Belfast site, aromatics were not measured, and only a limited number of alkanes were reported. *Singh et al.* [1981] report limited summertime alkane and alkene measurements taken at the Lawrenceville, Illinois, site of *Westberg et al.* [1975] and the Elkton, Missouri, site of *Rasmussen et al.* [1977]. The rural North Carolina study of *Seila et al.* [1984] is the most complete in terms of the number of individual NMHC considered. However, only annual averages are reported, although no annual variation in the total NMHC was observed. The five rural measurement sites of this study were located at ridge and mountain tops well above the surrounding terrain. For this reason, we compare model-derived quantities at the lowest model level with the three sites having the lowest elevation (Linville Gorge, Rich Mountain, and Deer Park) and bear in mind that the observed values represent lower limits to what is representative at lower elevations. Two of these sites (Rich Mountain and Deer Park) are within one 60×60 km^2 grid, are very similar, and exhibit nearly identical NMHC concentrations, so values for these two sites are averaged for the comparison.

Because of the species lumping within the model formulation, a comparison between observed and model-calculated NMHC is practical only if one also considers the OH reactivity of each NMHC. The species distribution of the observed anthropogenic NMHC are therefore lumped into the equivalent model species using

$$\sum_i \mathrm{NMHC}_i \cdot k_{\mathrm{NMHC}_i\text{-OH}} \tag{7}$$

where the $NMHC_i$ are the individual NMHC species observed, and k refers to the reaction rate of each hydrocarbon with OH. The choice of this reaction weighted quantity allows a comparison of the O_3 production potential from the initial products of the anthropogenic NMHC, since the rates of all RO_2-NO reactions are equivalent (see Table 8).

Table 12 gives the comparison of OH reactivity weighted lumped NMHC species for the 6 rural sites just mentioned. At all sites except Belfast, Maine, the model roughly equals or underpredicts reactivity weighted NMHC. Within the model, the grid representing the Belfast site is directly under the influence of continental sources because of persistent westerly flow, while one would anticipate, for average summer conditions, relatively lower concentrations due to its coastal location and the formation of a local sea-breeze circulation. Moreover, iso-pentane and *n*-pentane were the only species measured at this site that fall into the high-alkane class of lumped species. The North Carolina sites are in excellent agreement with model-predicted total reactivity weighted NMHC. However, this agreement is fortuitous, since the comparison is with annually averaged quantities, and all of the measurement sites were on ridge and mountain tops, which introduces ambiguity in what model level should be used in the comparison. Nonetheless, the partitioning between the individual lumped species is reproduced quite well by the model in this region. The two Illinois sites and the Missouri site suggest that the total NMHC predicted by the model is a factor of 2 to 3 too low in comparison to these observations, the most significant difference occurring in the higher alkenes. However, a quantitative comparison is hard to justify when one considers the scatter in the observed data (1σ standard deviations of 125%,

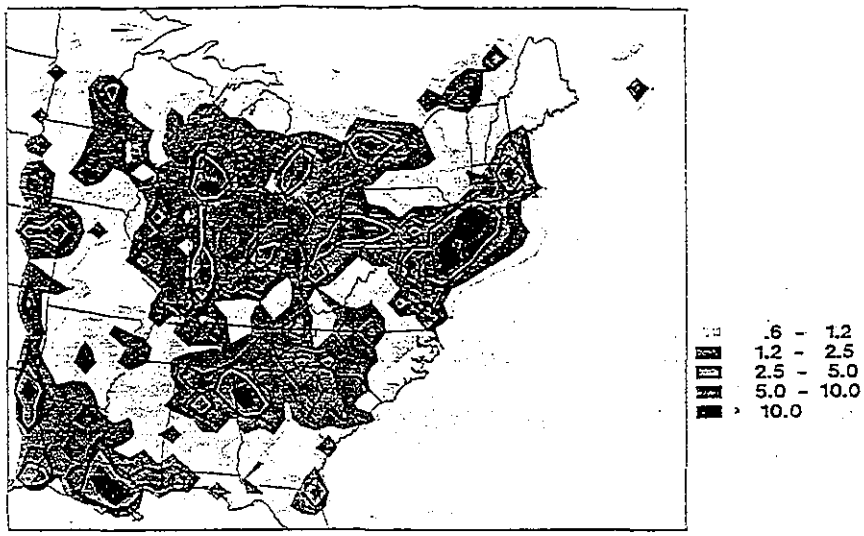

Plate 2. The 9 a.m. to 5 p.m. EST average NO_x for the lowest model layer on July 6, 1986 (ppbv).

135%, and 68% of the mean concentrations for propene, ethene, and *i*-butane, respectively, in the Sexton and Westberg study). The scatter in the model-predicted concentrations over the 3 days of averaging (day to day variations <50% of the mean for any lumped species at these three sites) is somewhat less but still adds to the uncertainty. We conclude that the partitioning between the lumped anthropogenic NMHC species within the model, particularly with respect to the reactivity weighting relevant to O_3 formation, is reasonably consistent with the few available rural observations. It should also be noted that reactivity-weighted anthropogenic NMHC measurements taken during the model simulation period at the Scotia site show good agreement with those predicted by the model for that location (Trainer et al., manuscript in preparation, 1991). Similar to the case for NO_x, information on the height distribution of NMHC is very scarce. The only comparable observations over the eastern United States are unpublished by the investigators. However, they have been cited by *Fishman et al.* [1985]. Neither the gradients or magnitudes are consistent with the three-dimensional model results averaged over the same area as the Persistent Elevated Pollution Episode/Northeast Regional Oxidant Study (PEPE/NEROS) study region. Aircraft measurements from Westberg [*Altshuller*, 1989] are all above the PBL and do not include vertical gradients, just bulk upwind values over Birmingham, Atlanta, Philadelphia, and New York. Therefore we must defer assessment of our vertical NMHC profiles until appropriate observations become available.

The average mixing ratios of isoprene (+ α-pinene) from 9 a.m. to 5 p.m. calculated for the surface level (centered at 37 m) on day 3 are shown in Plate 3. The values range from about 0.05 ppbv to 1 ppbv except over the areas affected by oceanic air. The calculated concentration of isoprene should be regarded as the sum of all natural NMHC normalized to the reaction rate constant of

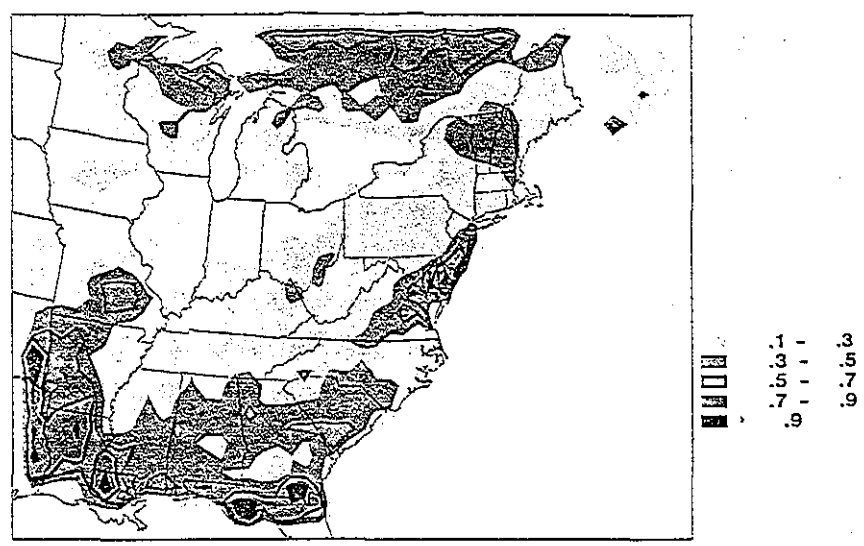

Plate 3. The 9 a.m. to 5 p.m. EST average isoprene distribution for the lowest model layer on July 6, 1986 (ppbv).

TABLE 12. Comparison Between Modeled and Observed NMHC with Weighting According to OH Reactivity

Site	ΣButane[a]	ΣHigh Alkane	Ethene	ΣHigh Alkene	Total
Belfast, Maine[b]	1.6/3.5[c]	>1.8/ 12.4[d]	6.7/ 2.8	>4.2/ 3.0	>19.7/ 21.6[d]
Robinson, Ill.[b]	6.9/3.1	17.6/ 14.8	6.7/ 3.3	16.6/ 7.4	54.0/ 28.5
Elkton, Mo.[e]	3.2/1.3	>4.0/ 5.1	6.7/ 1.7	8.5/ 2.6	>25.4/ 10.7
Lawrenceville, Ill.[e]	12.6/5.6	>12.9/ 19.7	16.8/ 4.7	25.4/ 9.9	>72.4/ 39.9
Linville Gorge, N. C.[f]	1.2/2.7	10.5/ 13.5	2.7/ 2.7	8.4/ 6.4	26.5/ 25.3
Rich Mountain, N. C.[f]	1.4/2.6	10.7/ 12.2	4.7/ 2.8	6.2/ 6.4	26.7/ 23.9

[a]Observed values are derived by weighting individual species concentrations with the OH reaction rates at 298° K, and summing over the model lumped NMHC classes. The OH reaction rates are taken from *JPL* [1987] and *Atkinson* [1985]. Calculated values are based on model concentrations averaged from 7 to 9 a.m. EST from July 5, 1986, to July 7, 1986, and weighted with OH reaction rates used in the model (see Table 8).

[b]*Sexton and Westberg* [1984]. The Belfast, Maine, measurements were from June to July 1975, and the Robinson, Illinois, measurements were from June to July 1977. Both sets are 6 to 9 a.m. averages.

[c]All entries are in the form: (derived from observations)/(model derived). All values are in units of ppb (cm^3 $molecule^{-1}$ s^{-1})$\times 10^{-12}$.

[d]Aromatic compounds were not measured for sites containing the ">" symbol in these columns.

[e]*Singh et al.* [1981]. The Lawrenceville, Illinois, measurements occurred in June 1974 and were originally published by *Westberg et al.* [1975]. The Elkton, Missouri, measurements occurred in August-September 1975 [*Rasmussen et al.*, 1977].

[f]*Seila et al.* [1984]. All measurements occurred between September 1981 and October 1982, and all values are annual averages. The Rich Mountain values are a composite average of the Rich Mountain and Deer Park observations. All sites from this study are at least 300 m above the terrain surface of the model.

isoprene. Because of the high reactivity of isoprene with OH, its distribution has large spatial and temporal variabilities [*Hov*, 1983; *Trainer et al.*, 1987b]. Also, vertical transport processes have a dominating influence on surface concentrations, as will be shown in connection with the budget analysis of the ozone precursors. The coastal locations and the region around Louisiana with high isoprene are associated with shallow PBL heights. Regions of cloudiness (Figure 2*c*) also have low PBL heights, a decrease in the photolytic production of OH, and hence enhancements of isoprene associated with high cloud optical depths. This is most obvious in the South Carolina-northern Georgia area and the Vermont-New Hampshire region extending north and west into Canada, where isoprene-emitting forests are also located.

Isoprene emission rates depend strongly on temperature, and most of the isoprene observations were made at the surface near source areas that are substantially below the altitude of the lowest level of our model. A large altitude gradient in isoprene therefore compounds the difficulty of comparison [*Trainer et al.*, 1987a]. Figure 9*a* gives the height distributions of isoprene and the reactivity-weighted sum of the primary anthropogenic NMHC for July 6, 1986, averaged over the daytime (9 a.m. to 5 p.m. EST) and over land area. The mixing ratio of isoprene decreasing by a factor of ~20 from the lowest layer to the top of PBL (~1.4 km), while the reactivity-weighted anthropogenic NMHC have a much smaller gradient and dominate the natural NMHC in terms of RO_2 formation potential above 500 m. At the surface, where O_3

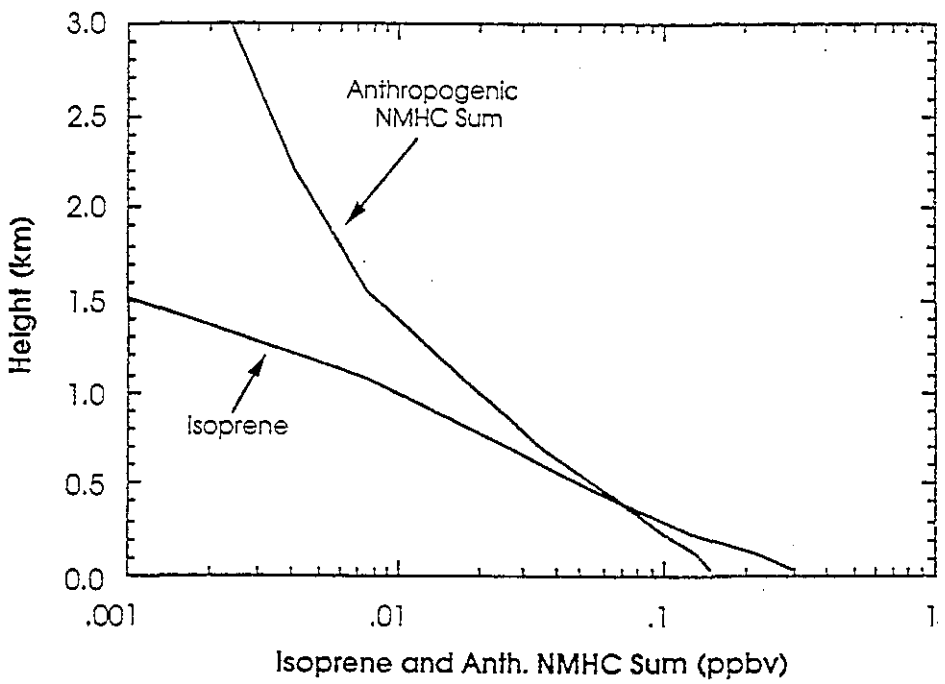

Fig. 9*a*. Vertical profiles of the 9 a.m. - 5 p.m. EST average isoprene and OH reaction weighted anthropogenic NMHC (equation (7)) on July 7, 1986, also averaged over the continental region of the model domain.

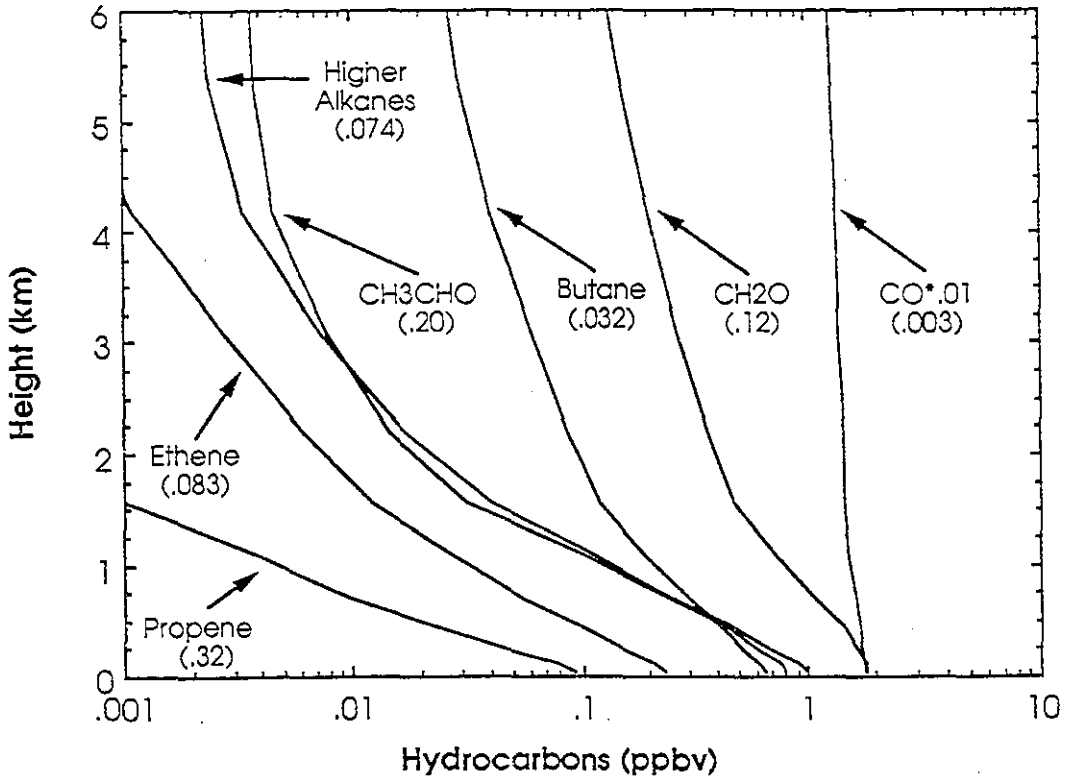

Fig. 9*b*. Vertical profiles of individual anthropogenic NMHC as well as CO and the aldehydes average from 9 a.m. - 5 p.m. EST and over the continental region of the model domain. Numbers in parentheses are the relative reaction rates of each NMHC with OH, normalized to the isoprene-OH reaction rate.

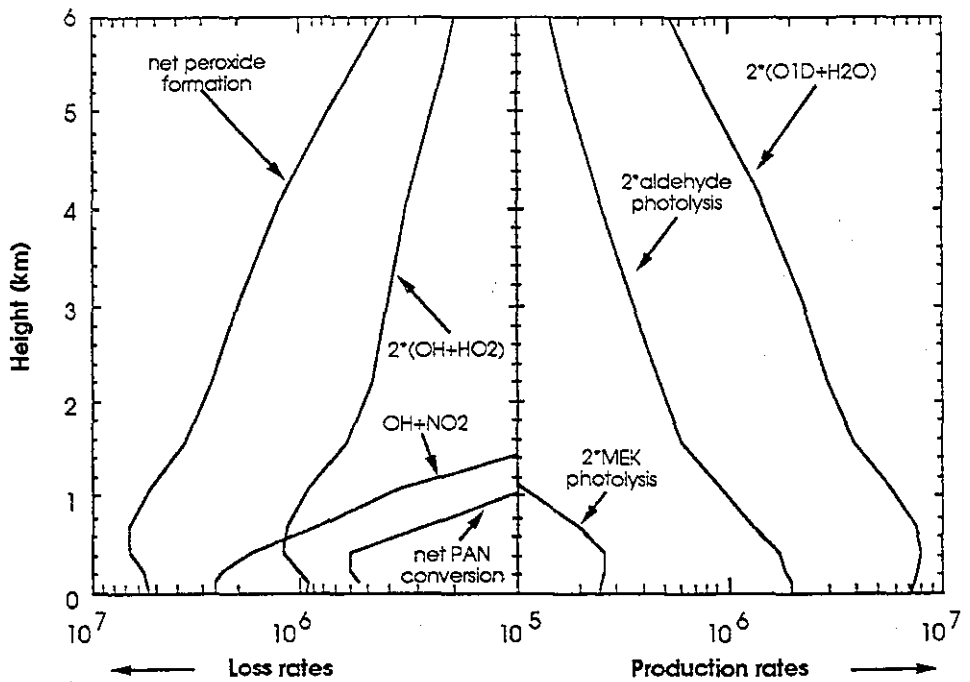

Fig. 9*c*. Vertical profiles of the rates of individual reactions most important in the loss or production of HO_x+RO_2. The rates are averaged from 9 a.m. to 5 p.m. and over the continental region of the model domain. All units are in molecule cm^{-3} s^{-1}.

production is a maximum, the natural NMHC contribute on the average nearly twice as much as the anthropogenic NMHC to the available NMHC oxidation products.

Figure 9*b* gives the vertical distribution of the four lumped NMHC species used in the model, along with CO for the last day of model simulation. The aldehydes CH_2O and CH_3CHO are also shown for completeness. Below 3 km, the regionally averaged concentrations of these species are in steady state after the third day. The reactivity of each hydrocarbon or aldehyde normalized to the isoprene-OH reaction rate is also given in Figure 9*b*, from which it can be seen that the magnitude of the vertical gradients for the primary NMHC are proportional to the OH reactivity.

From Figures 9*a* and 9*b* it can be seen that at the surface, CO accounts for 41%, isoprene for 21% and the aldehydes for 28% of the OH conversion to HO_2 or RO_2 on the average. Above 1 km, CO dominates the conversion processes. The higher alkanes constitute the largest anthropogenic RO_2 source near the surface, and butanes dominate at higher altitudes.

In terms of O_3 photochemical production, the product of the relative OH reaction rates and the mixing ratios in Figure 9*b* gives the relative importance each NMHC contributes to peroxy radical formation from the primary NMHC oxidation step. However, one must also consider that the aldehydes as well as ketones are the products of primary and secondary NMHC oxidation steps. Additionally, since the reactions of NO with the organic peroxy radicals have HO_2 or RO_2 as products, more than one O_3 molecule can be produced for every NMHC molecule oxidized by OH. From a more fundamental point of view, the sum of OH, HO_2, and RO_2 is directly proportional to O_3 production [*Kleinman*, 1986; *Trainer et al.*, 1987a], in which case the primary NMHC oxidation steps simply convert HO_x to RO_2. Figure 9*c* shows the 9 a.m.-5 p.m. (EST), and continental area average vertical distributions of the main production and loss terms for the sum of HO_x and RO_2. The net losses (the loss minus the production due to reactions that return HO_x and RO_2) due to PAN and peroxide formation are shown to illustrate the net effect of these processes. The O^1D+H_2O reaction accounts for a majority of the production throughout the lower troposphere, although formaldehyde photolysis accounts for about 20% throughout the lower 6 km. The $OH+NO_2$ reaction ((R29) in Table 8) is an important loss for the sum of HO_x and RO_2 at the surface but falls off quickly with altitude as NO_x decreases. The recombination reactions of HO_2 with itself and RO_2 to form peroxides are important throughout the lowest 6 km. On the average, net PAN formation contributes little to the radical loss, with an average maximum influence of about 9% at 200 m.

3.3. *The Budget and Photochemical Generation of Ozone*

In this section, factors influencing O_3 production at the surface and throughout the PBL on a regional basis are examined, along with simple budget studies above and within the PBL of O_3 and its precursors.

The horizontal variations in the diurnally averaged (day 3) net O_x production are shown for both the lowest layer and the 0-1800 m average in Plates 4*a* and 4*b*. One striking feature in both figures is that the variability of net O_3 formation is relatively small (less than a factor of 4) over large regions of the continent. One can conclude that O_3 formation over rural areas represents a significant fraction of the total O_3 being produced. Due to elevated NO_x sources from power plants, a relatively high rate of O_3 formation along the Ohio River valley is evident in 0-1800 m average, but is absent in the 0-80 m layer. Similar to the case for the isoprene distributions, the regions of cloudiness shown in Figure 2*c* have suppressed O_3 formation near the surface. There is some indication in Plate 4*a*, particularly along the western edge of the cloudy region in the southeastern United States, that O_3 formation is enhanced just outside the cloudy region, where relatively high NO_x levels caused by the reduced photochemistry beneath the cloud (see also Plate 2) are being advected into the cloud-free regions. Also in Plate 4*a*, isolated regions near the southern and southwest border appear to act as strong source areas that influence local O_3 formation. While enhanced O_3 formation is expected in these strong source regions, difficulties in predicting the PBL height near borders and coastal locations do not allow us to have confidence in our predictions for these regions.

If one compares the NO_x distribution in Plate 2 to the net O_3 formation in Plate 4*a*, the regions of highest net O_3 formation are generally adjacent to urban locations with strong NO_x sources. The influence of the Boston-Washington corridor extends into the Atlantic and slightly southward into eastern Virginia, consistent with the air flow depicted in Figures 2*a* and 2*b*. The general pattern of net O_3 formation maximums associated with strong urban sources is also apparent in Plate 4*b*. However, Plate 4*b* shows that averaged over the lowest 1800 m, the net O_3 production is more extensive through the Ohio and Pennsylvania region than is evident in just the surface plot. This corresponds to the center of the high-pressure region where PBL heights are a maximum and is therefore the region where O_3 precursors have the highest potential for influencing the column below 1800 m.

Averaging over the continental domain and from 0 to 1800 m, 85% of the net O_3 formation occurs between 9 a.m. and 5 p.m., EST. A majority of the O_3 photochemically lost over the diurnal cycle (60%) also occurs during this time. Therefore the diurnal averages in net O_3 formation are dominated by the photochemistry occurring during this 8-hour period. Net photochemical loss is observed during the nighttime hours between 9 p.m. and 5 a.m., largely due to the formation of NO_3 and N_2O_5 from the O_3 reaction with NO_2 and the subsequent loss of N_2O_5 to aerosols and NO_3 reactions with naturally emitted NMHC to form organic nitrates. However, the total O_3 photochemically lost during this 8-hour period is only 18% of the total O_3 lost over the diurnal cycle.

In order to understand photochemically the behavior of O_3 formation with respect to ambient NO_x levels, we examine the net O_3 formation rates at a particular time. Figure 10*a* shows a scatter diagram of the net O_x production at 1 p.m. EST on the fouth day for the lowest model layer as a function of NO_x concentration. Only data with no overhead cloudiness are considered. The different symbols correspond to the levels of (natural plus anthropogenic) NMHC mixing ratios with the anthropogenic NMHC weighted by OH reactivity, and normalized to that of isoprene (equation (7)). It can be seen from Figure 10*a* that net photochemical O_3 production generally increases as NO_x increases from 0.1 to ~2 ppbv. Although there are relatively few points with NO_x values > 4 ppbv, there is a general trend for net O_3 production to decrease with increasing NO_x above this value, with the magnitude related to the amount of precursor NMHCs. For NO_x less than 1 ppbv, much of the scatter in Figure 10*a* is due to scatter in the O_3 loss term, while above 1 ppbv the O_3 production term dominates the net photochemistry and accounts for a majority of the scatter. As was discussed by *Trainer et al.* [1987*a*,*b*] at NO_x levels less than ~1 ppb, O_3 production is limited by NO_x availability, while at higher NO_x levels, O_3 production is quite sensitive to the ambient NMHC to NO_x ratio. The large scatter in the NO_x range 3-10 ppb for a particular range of NMHC shows that factors other than total NMHC also influence production. To a good approximation the net O_3 production is simply the sum of the reactions:

(R24) $\quad NO + RO_2 \rightarrow NO_2 + OH$

(R66,R83,R85,R89, R91,R93,R113,R115) $\quad NO + RO_2 \rightarrow NO_2 + \text{products}$

An analysis of individual terms at $NO_x \approx 7$ ppbv shows that a large part of the variation can be explained by differences in the HO_x production sequence:

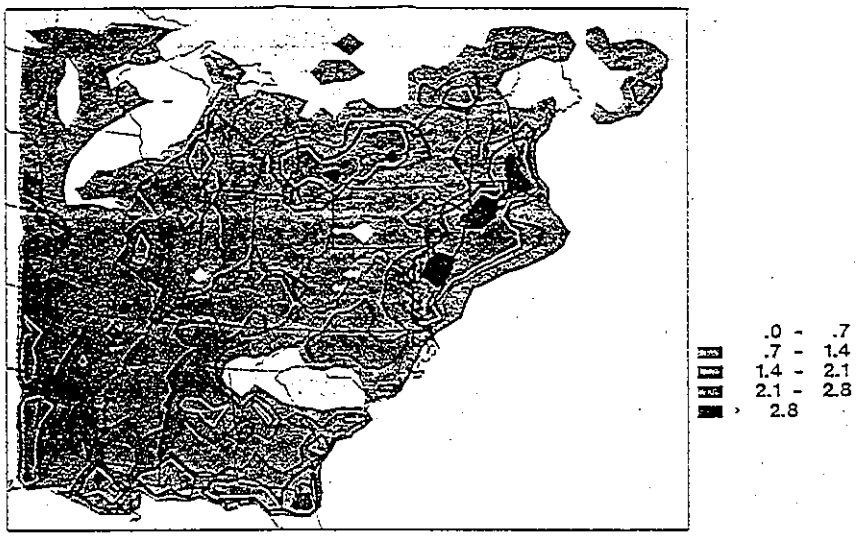

Plate 4*a*. The net O_3 production minus loss (units of ppbv h^{-1}) diurnally averaged from 1200 UT, July 6, 1986, to 1200 UT, July 7, 1986, for the lowest model level (~37 m).

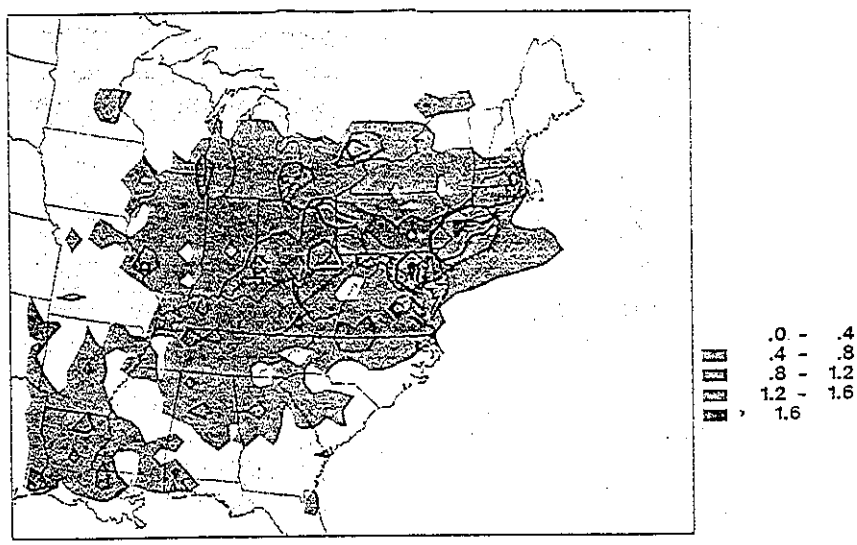

Plate 4*b*. The net O_3 production minus loss (units of ppbv h^{-1}) diurnally averaged from 1200 UT, July 6, 1986, to 1200 UT, July 7, 1986, and also averaged over the lowest seven model layers (~1800 m above the surface).

(PO3D) $$O_3 + h\nu \rightarrow O^1D + O_2$$

(R8) $$O^1D + H_2O \rightarrow OH + OH$$

with (R8) varying by more than a factor of 2 between humid southern sites, and relatively dry northern sites with equivalent NO_x, O_3, and NMHC levels. The formation rate for the sum of RO_2 and HO_x is also influenced by variations in formaldehyde levels and its subsequent photolysis to yield HO_2 (PHO in Table 8). Since formaldehyde production is significantly influenced by RO_2 abundance, and since isoprene oxidation is the fastest path to RO_2 formation, the ratio of isoprene to anthropogenic NMHC contributes to the variation for a given total NMHC amount. Variations in ketone and higher aldehyde abundances make additional minor contributions to the scatter. For the midday conditions within the model, PAN and NO_x are essentially in equilibrium, so the net PAN formation accounts for less than 0.5 ppb h^{-1} at any NO_x level in Figure 10*a*. O_3 itself can influence HO_x and hence O_3 production through the reaction sequence (PO3D) and (R8). However, as was pointed out by *Fishman et al.* [1985], its immediate impact can be mitigated somewhat by affecting the NO balance through the reaction

(R26) $$O_3 + NO \rightarrow NO_2 + O_2$$

The decrease in O_3 photochemical production for NO_x levels > 5 ppbv in Figure 10*a* is due to a precipitous drop in peroxy radical concentrations for NO_x > 2 ppbv, as illustrated in Figure 10*b*. This behavior in the sum of RO_2 and HO_2 is largely a consequence of the NMHC to NO_x ratio that is characteristic of the emissions inventory and transport processes influencing the concentrations of these precursors. On the basis of the mean carbon numbers for each of the model NMHC classes [*U.S. EPA*, 1989] and assumed concentrations (based on average emissions) of other species such as ethane and propane not considered in the model, we calculate an NMHC to NO_x ratio between 7 and 1 (ppb C ppb^{-1} NO_x) with an average of 4 when NO_x > 10 ppbv between

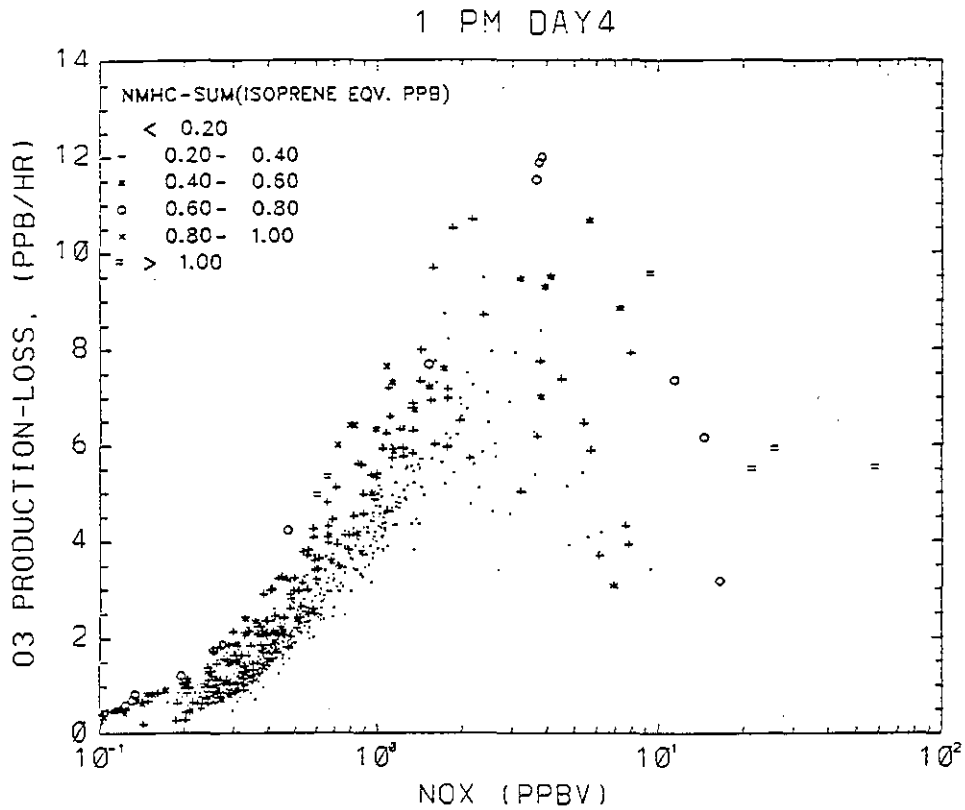

Fig. 10*a*. Scatter plot of O_3 production minus loss (ppbv h^{-1}) at 1 p.m. EST on July 7, 1986, for cloud-free and continental locations in the bottom model layer as a function of NO_x. Different symbols correspond to values of NMHC in OH reactivity-weighted units that are normalized to isoprene reactivity.

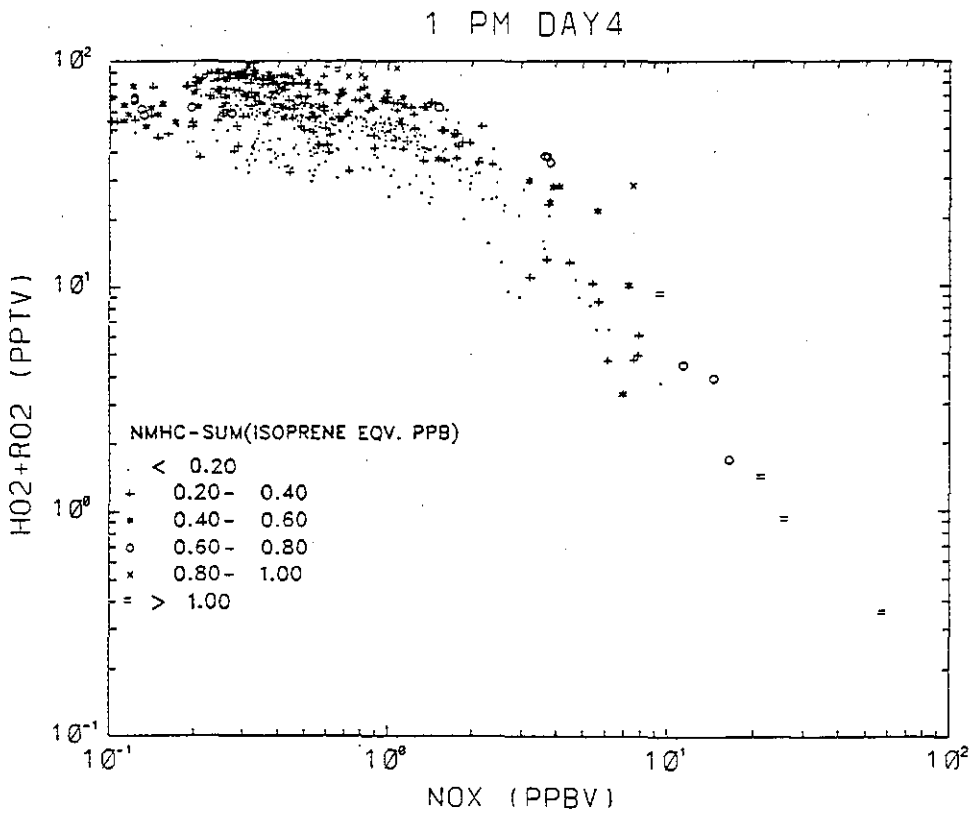

Fig. 10*b*. Scatter plot of HO_x+RO_2 (pptv) at 1 p.m. EST on July 7, 1986, for cloud-free and continental locations in the bottom model layer as a function of NO_x. Different symbols correspond to values of NMHC in OH reactivity-weighted units that are normalized to isoprene reactivity.

7 a.m. and 9 a.m. (EST). Thus the decrease in O_3 production at higher NO_x levels is consistent with EKMA type box model studies [*Dodge*, 1977; *Lin et al.*, 1988] in which low NMHC to NO_x ratios do not allow enough HO_2 and RO_2 formation to stay ahead of the odd-hydrogen loss through

(R29) $$OH + NO_2 \rightarrow HNO_3$$

Seinfeld [1988] also concluded that NMHC to NO_x ratios of 3 or 4 are characteristic of eastern U.S. urban counties, on the basis of the same emissions inventory, but these ratios are significantly lower than the median ratios of 7 to 15 that are observed for urban regions in the eastern United States [*Seinfeld*, 1988; *Altshuller*, 1989]. Possible causes of this discrepancy have been discussed by *Altshuller* [1989] and include the neglect of evaporative NMHC emissions in the NAPAP emissions inventory and the influence of the nocturnal inversion height in separating NO_x emissions from power plants with surface emissions of NMHC during early morning hours when the NMHC to NO_x ratios are measured. The effects of an underestimation in the anthropogenic or natural NMHC emissions on net O_3 formation, as well as a detailed analysis of the diurnal dependence of the NMHC to NO_x ratio, are beyond the scope of this study and are left for future work.

The model has also been used to study the budget of O_3 and its precursors for the same time period, with emphasis on the average large-scale picture of the processes affecting the various species. In this case we again average over the continental region within the model borders and also consider the horizontal flux of species off the Atlantic coast as well as to continental grid points along the model borders. The net changes due to vertical transport (advection, diffusion, and PBL mixing), photochemistry, emissions, and deposition are then summed over grid points and 24 hours to derive a layer average change for each individual process over 1 day. Layers can be summed or looked at individually to obtain insight on the average magnitude and importance of each process for different scales of vertical resolution. Results for O_3, NO_x, isoprene, and higher alkanes are shown in Figures 11-14 for the diurnal cycle beginning 2½ days after model initiation. We have chosen to present results for the bottom layer (0-75 m), the lowest 1800 m (bottom seven layers), and the 1800-3600 m layer. The average mixing ratios at the end of the diurnal cycle are also shown, with units of the accumulated diurnal changes given in ppbv d^{-1}.

As shown in Figure 11, the amount of O_3 in the bottom layer is largely controlled by deposition and photochemical production, although photochemical loss and vertical diffusion from above (primarily at night) each contribute ~30% to the net loss and source respectively. Averaging over the bottom 1800 m, photochemistry and flow out over the Atlantic determine the net balance with a turnover time of 1.5 days. The chemical production in figure 11*b* corresponds to a continental average production rate of 1.1×10^{12} molecule cm^{-2} s^{-1}. This value is somewhat lower than the 1.48×10^{12} molecule cm^{-2} s^{-1} due to anthropogenic NO_x emissions deduced by *Fishman et al.* [1985] from one-dimensional calculations based on summertime conditions in the eastern United States. Also, since 70% of the total NO_x emissions in the continental United States occur within our model domain, the production rate is consistent with the estimate of 1×10^{12} molecule cm^{-2} s^{-1} averaged over the United States during summer by *Liu et al.* [1987] due to anthropogenic NO_x emissions. About 25% of the O_3 formed below 1800 m is

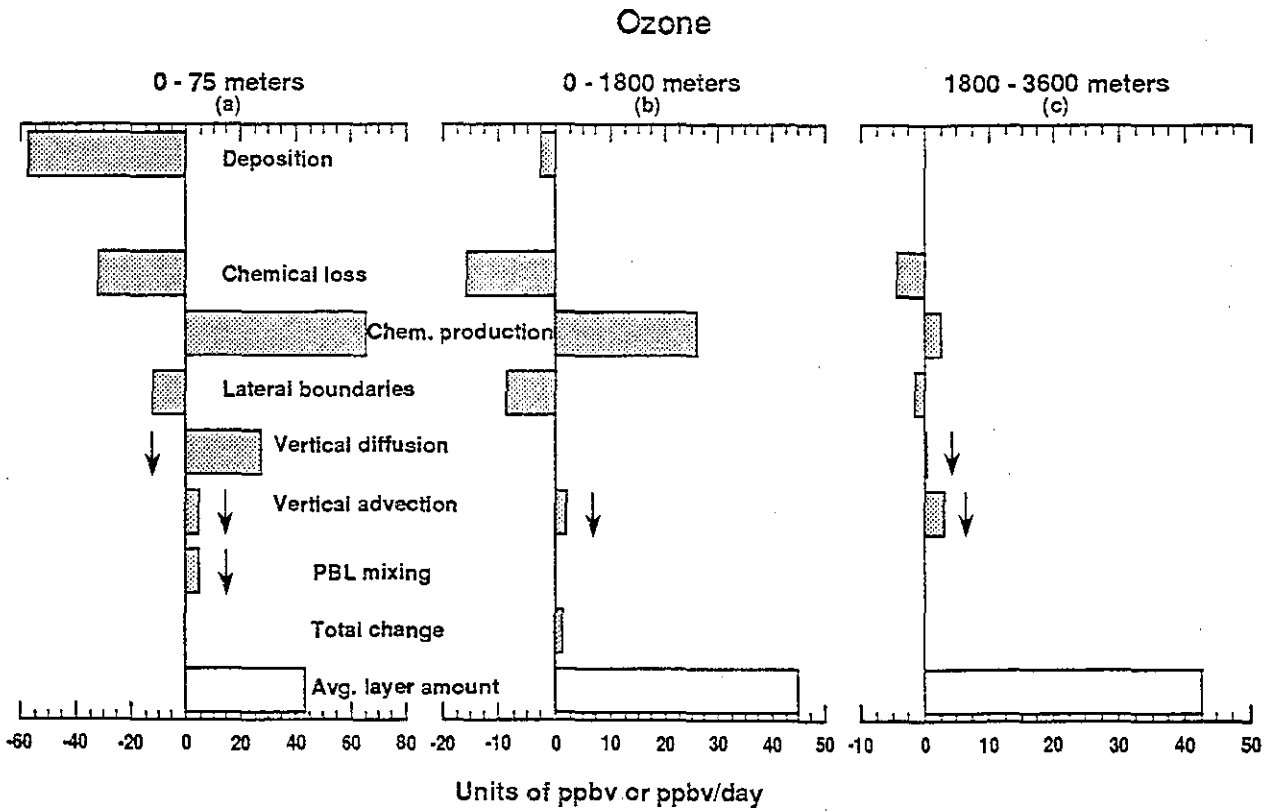

Fig. 11. The budget of O_3 over the diurnal cycle from 1200 UT on July 6, 1986, to 1200 UT on July 7, 1986, averaged over continental regions of the model domain. Budgets are shown for three height layers: (*a*) the surface layer, (*b*) the layer extending from 0 to 1800 m above the surface, and (*c*) the 1800 to 3600 m layer. Arrows indicate the direction of vertical flux affecting the layer.

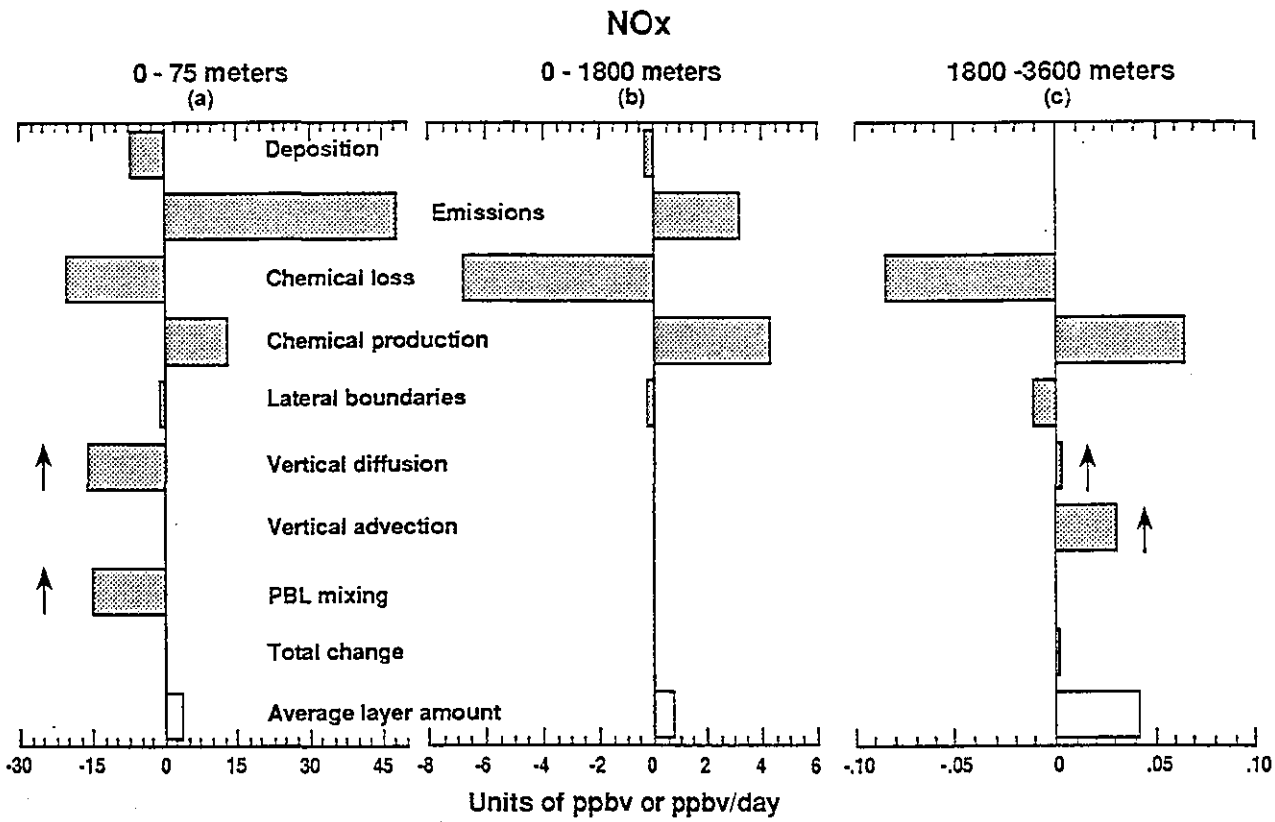

Fig. 12. The budget of NO_x over the diurnal cycle from 1200 UT on July 6, 1986, to 1200 UT on July 7, 1986, averaged over continental regions of the model domain. Budgets are shown for three height layers: (*a*) the surface layer, (*b*) the layer extending from 0 to 1800 m above the surface, and (*c*) the 1800 to 3600 m layer. Arrows indicate the direction of vertical flux affecting the layer.

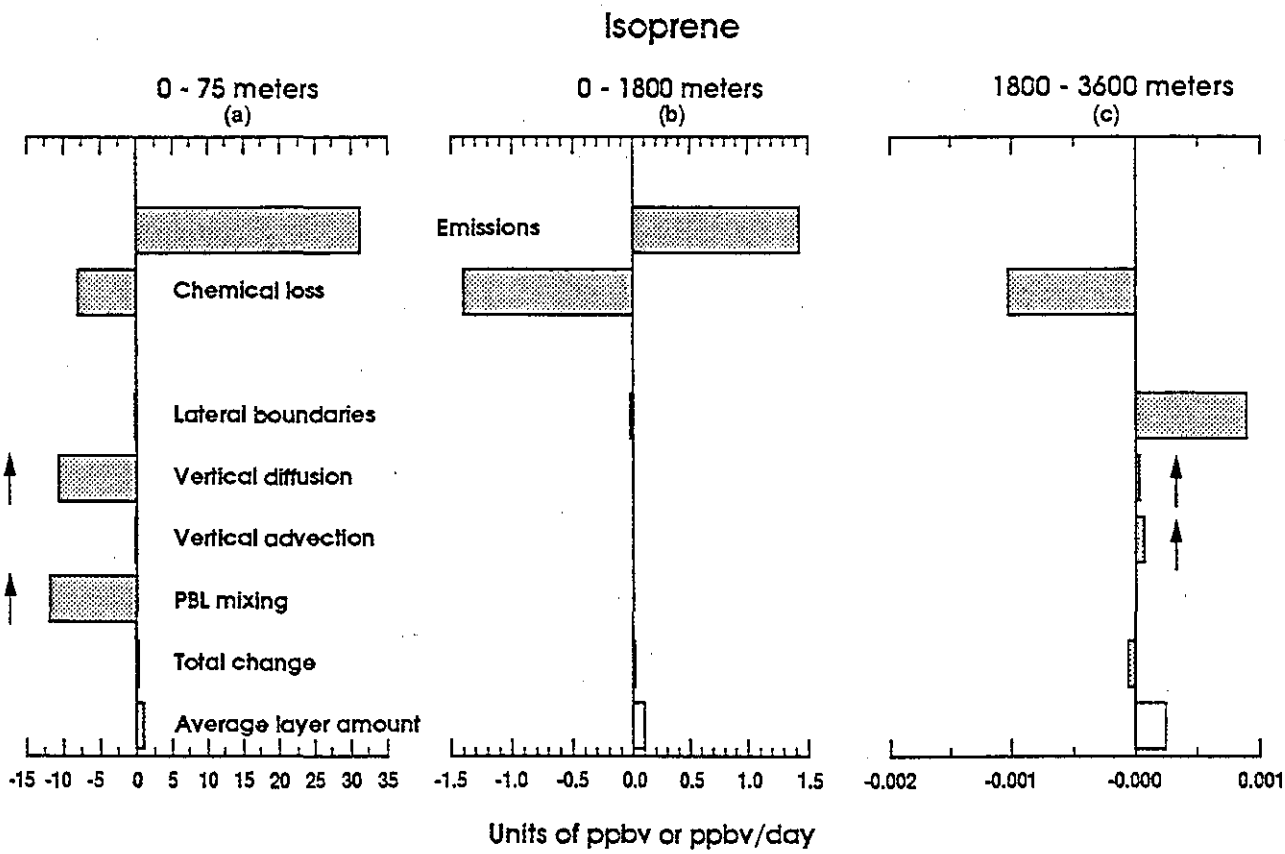

Fig. 13. The budget of isoprene over the diurnal cycle from 1200 UT on July 6, 1986, to 1200 UT on July 7, 1986, averaged over continental regions of the model domain. Budgets are shown for three height layers: (*a*) the surface layer, (*b*) the layer extending from 0 to 1800 m above the surface, and (*c*) the 1800 to 3600 m layer. Arrows indicate the direction of vertical flux affecting the layer.

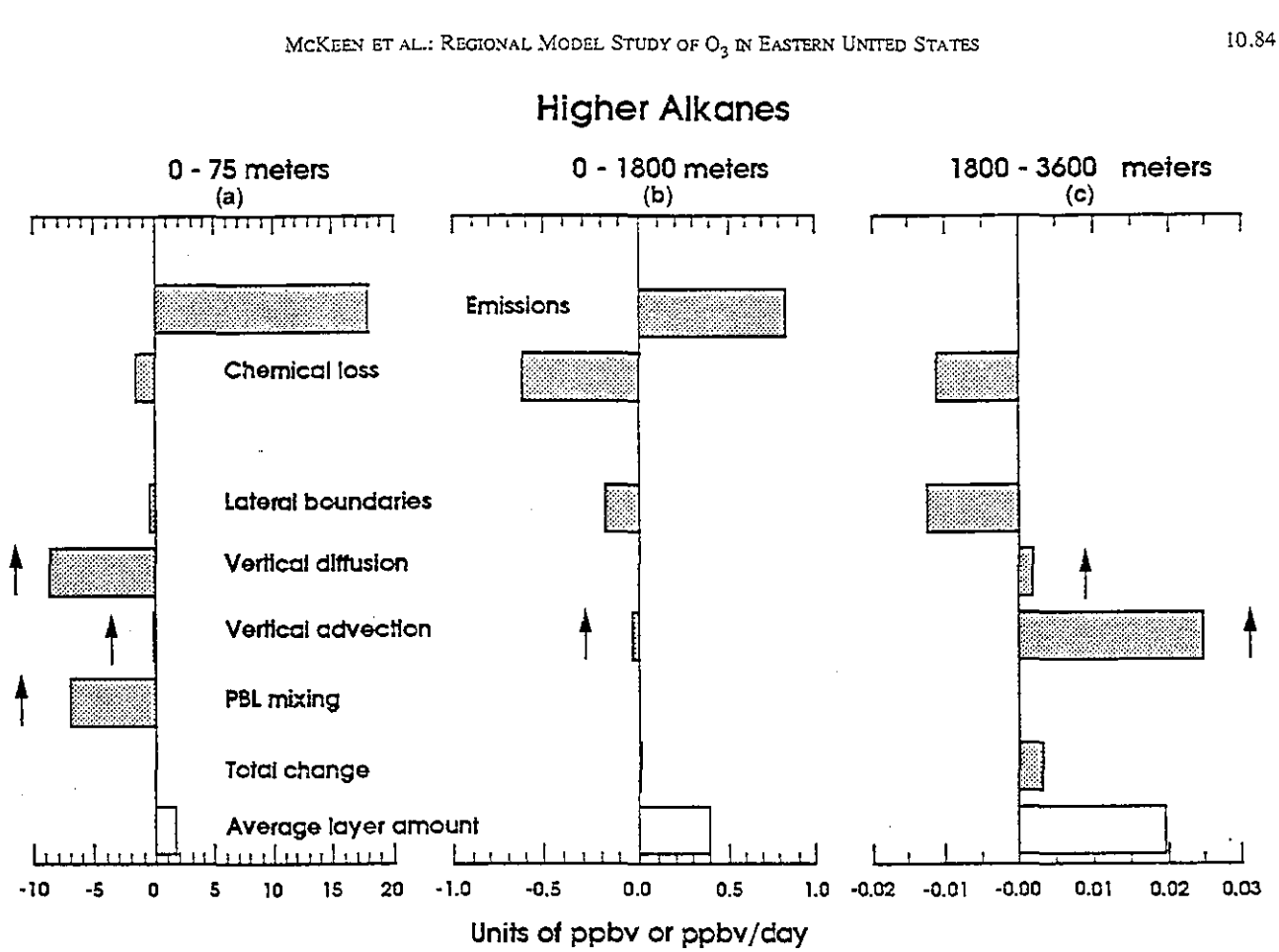

Fig. 14. The budget of higher-alkanes over the diurnal cycle from 1200 UT on July 6, to 1200 UT on July 7, 1986, averaged over continental regions of the model domain. Budgets are shown for three height layers: (*a*) the surface layer, (*b*) the layer extending from 0 to 1800 m above the surface, and (*c*) the 1800 to 3600 m layer. Arrows indicate the direction of vertical flux affecting the layer.

advected out over the Atlantic between 35° and 45° latitude. Within these height and latitude limits this corresponds to an average horizontal flux of 3.2×10^{14} molecule cm^{-2} s^{-1}. Between 1800 and 3600 m the turnover time increases to ~8 days, and vertical advection of O_3 from higher layers balances a net photochemical loss and a small loss out of the boundaries. The net downward motion associated with the high-pressure conditions of this study has only a minor influence in terms of downward advection of O_3 from the middle troposphere to the lowest 1800 m. However, these conditions are favorable to O_3 precursor buildup and consequently the large O_3 production evident below 1800 m.

NO_x, isoprene, and higher alkanes are controlled primarily by emissions and vertical mixing in the bottom layer. For NO_x the interconversion with PAN accounts for most of the photochemical production and loss terms. However, layer averaged PAN is essentially in equilibrium below 3600 m. The net photochemical NO_x loss is due to reaction with OH, except at the very bottom layer where 10% of the photochemical NO_x loss in Figure 12*a* is due to organic nitrate formation (4% for the 0-1800 m average). For the 0 to 1800 m layer, all three precursors are controlled primarily by emissions and chemical loss, with loss to the boundaries contributing about 25% to the relatively long-lived higher alkanes.

Transport of pollutants and their precursors such as NO_x and NMHCs to the upper troposphere is a major concern because of the potential for long-range transport. The photochemical lifetimes of pollutants such as O_3 and PAN becomes significantly longer at higher altitude, and concurrently, the wind speed increases with altitude. For the case shown in Figures 11-14, only 1% of the NO_x and 3.5% of the higher alkanes that are emitted near the surface are transported above 1800 m. The flux of PAN above 1800 m (not shown) is about 25% larger than that of NO_x, so ~2.25% of the emitted NO_y is transported above 1800 m. In the 1800-3600 m layer, NO_x and higher alkanes are transported by advection from below with turnover times of the order of a day, despite the general downward advection associated with the high-pressure conditions. However, the fluxes associated with the advection process are relatively small, so the precursor concentrations in this layer are low enough to effectively suppress O_3 production. Isoprene levels in this layer average about 0.3 pptv (parts per trillion by volume), due largely to the mixing ratios specified on the continental boundaries at this height (~2 pptv). Within the model, vertical diffusion coefficients above the PBL are set to fairly small values (1 m^2 s^{-1}), according to the background vertical diffusion coefficients recommended by *Zhang and Anthes* [1982]. Therefore the influence of vertical diffusion is expected to be small at all heights except close to the ground, where large gradients and higher vertical diffusion coefficients can be present. *Gidel* [1983] and *Chatfield and Crutzen* [1984] found that the most effective vertical transport is probably via convective clouds. Our choice of a high-pressure environment may lead to slower vertical transport relative to the average conditions in the summer. Alternatively, since subgrid-scale cumulus convection is ignored in the model formulation, these results represent a lower limit to the amount of precursor material that may actually be transported upward from below 1800 m. As was mentioned previously, the effects that subgrid-scale cumulus convection and

other mixing processes at the PBL boundary may have upon the transport of O_3 and its precursors between the PBL and the free troposphere are left for future work, when adequate parameterizations for these processes become available.

By looking at the total change over the 1-day time period in Figures 11-14, it is obvious that below 3600 m the model is nearly in steady state with respect to continental averages. The one exception is a 15% increase in higher alkanes for the 1800-3600 m layer, due to the fact that the characteristic transport between the PBL and the layers above is much longer than the 3 days the model has been run. A judicious choice in the initial condition accounts for the lack of change in the 1800-3600 m O_3, while isoprene and NO_x have relatively fast photochemistry that dominates the chemistry-transport coupling below 3600 m. The fact that there is no significant trend in O_3 and its precursors below 1800 m leads us to believe that the O_3 mixing ratios predicted on the third and fourth days are not influenced by the initial conditions or the time from initiation.

4. Summary and Conclusions

We have developed an Eulerian regional-scale three-dimensional model that incorporates results from a mesoscale meteorological model with a photochemical mechanism and a transport algorithm to simulate abundances of several key atmospheric species over a given 4-day time period. Because of the high temporal resolution of the predicted meteorological variables, a more fundamental treatment of boundary layer growth, and a much larger vertical extent, the model differs significantly from previous three-dimensional models used to study rural O_3 [*Liu et al.*, 1984; *Lamb*, 1983].

Model performance is tested by comparing model derived O_3 values during the afternoon to those observed by the EPA monitoring network on the same days. In this way, the spatial variability of O_3 between the two data sets over a large region can be compared. In general, the magnitude, location, and movement of the highest O_3 concentrations observed on July 6 and 7, 1986, are reproduced well by the model. Regions of low O_3 associated with flow from the Atlantic Ocean that is well removed from the model boundaries are also well simulated. The correlation coefficient between the two data sets increases as the model progresses, with a value of 0.58 (statistically significant above the 99.9% level) obtained on the last 2 days of the 4-day period. Although this correlation is less than what we would like, an analysis of the observed O_3 values over the 4-hour period used in the calculations reveals large temporal and spatial variations over a 60×60 km^2 area. These variations are presumably due to subgrid-scale features such as topography, location relative to anthropogenic sources, and micrometeorological factors the model is unable to resolve. The model tends to consistently overpredict O_3 in regions where cumulus clouds were observed to be present, presumably owing to the absence of a subgrid cumulus convective parameterization scheme within the model formalism. The model consistently underpredicts O_3 along the eastern U.S. seaboard, south of Long Island. This is also a region where observed NMHC to NO_x ratios are much higher than those given in the 1985 NAPAP emissions inventory. A sensitivity run with NMHC emissions increased by a factor of 4 eliminated much of the predicted versus observed O_3 discrepancy in this region. A comparison between model predicted NO_x and NMHC with relatively long term measurements provides a qualitative means of assessing the model's ability to predict these O_3 precursors. However, there are only a limited number of measurements of both NO_x and NMHC in rural areas. The 13 NO_x comparisons show that the model tends to underpredict the long term averaged observations, but tends to fall within the large uncertainty limits associated with most of the observed NO_x data. For the one measurement program operational during the simulation period, NO_x averages agree quite well. The six sets of observations used in the NMHC comparison show that the relative partitioning of the species used in the lumping scheme is reproduced fairly well, but that the absolute amount of anthropogenic NMHC predicted by the model is somewhat less than that observed. However, large variations within the observations and model data preclude a meaningful quantitative comparison.

An analysis of the O_3 photochemical terms for clear sky, continental areas shows that O_3 production is NO_x limited over much of the model domain, and that midday net O_3 production generally decreases as NO_x values increase above 5 ppbv. This decrease is mostly due to the suppression of peroxy radical formation due to the low NMHC to NO_x ratios inherent in the NAPAP emissions inventory. The net O_3 production for relatively high NO_x values has a large degree of variability due to ambient NMHC concentrations, water vapor, isoprene abundance, and oxidation intermediates such as CH_2O.

When results of the model are used to analyze individual processes with respect to diurnal and layer averages over the continent, it becomes apparent that the choice of a high-pressure period, and possibly the neglect of subgrid-scale cumulus transport within the model formalism, lead to very little transport of O_3 precursors above 1800 m. Although the average O_3 transport is downward at 1800 m because of the net advection associated with the high-pressure conditions, this flux is unimportant in comparison with the O_3 photochemically produced within the PBL. We calculate an O_3 turnover time of about 1.5 days due to O_3 production below 1800 m that is largely balanced by photochemical loss and transport out over the ocean.

While this study focuses on the large-scale regional aspects of O_3, its precursors, and its formation, the model results contain a vast amount of information on the various photochemical and physical processes affecting the chemistry at individual points. A companion paper (Trainer et al., manuscript in preparation, 1991) will consider a more detailed look at these processes for a particular location with extensive, simultaneous, high-quality measurements. It should be emphasized that the results presented here are basically from one simulation. In this sense, these results represent a baseline case, from which further improvements in the model can be compared.

Several aspects of the model formulation involve approximations and assumptions that contribute to the overall uncertainty in the O_3 predictions. In terms of the model's ability to accurately describe the dynamic meteorology, the omission of important vertical exchange processes (i.e., subgrid-scale cumulus mixing) may seriously impact synoptic-scale O_3 predictions. The testing and assessment of reliable cumulus convection parameterizations is therefore anticipated. With respect to computational procedures, the numerical algorithm used to transport individual species is known to have significant numerical diffusion associated with it. Although the dominant transport process affecting O_3 and its precursors in the lowest 1 km is from convective mixing within the PBL, further tests with advective transport algorithms that do not contain numerical diffusion are necessary to fully assess its impact. The dependence of the overall results on grid resolution is also another area of concern that we intend to address. With respect to the chemical mechanism used in this study, there are several aspects of the lumping procedure that need to be tested within the framework of

three-dimensional simulations to assess the uncertainties in the predictions of O_3 and its precursors. Currently, computational resource constraints prohibit a more robust treatment of the complex photochemistry associated with anthropogenic and natural NMHC. Despite the uncertainties introduced from all of the considerations presented above, the model contains the essential and important elements related to the transport and photochemistry of O_3. In this sense the results presented in this work can provide a reference for future studies of the budget and distribution of rural ozone.

Acknowledgments. This research has been funded as part of the National Acid Precipitation Assessment Program by the National Oceanic and Atmospheric Administration (NOAA). The authors gratefully acknowledge David Mobley, Joan Novak, Thomas Pierce, Mark Saeger, and Jim Reagan for supplying the NAPAP emission inventories and ozone observations. We would also like to thank Xuejun Du, Lee Anne Lestak, and John Pansewicz for their assistance in data set development and computer graphics.

REFERENCES

Altshuller, A. P., The role of nitrogen oxides in nonurban ozone formation in the planetary boundary layer over N. America, W. Europe and adjacent areas of ocean, *Atmos. Environ., 20*, 245-268, 1986.

Altshuller, A. P., Nonmethane organic compound to nitrogen oxide ratios and organic composition in cities and rural areas, *J. Air Pollut. Control Assoc., 39*, 936-943, 1989.

Anderson, D. E., and R. R. Meier, Effects of anisotropic multiple scattering on solar radiation in the troposphere and stratosphere, *Appl. Opt., 18*, 1955-1960, 1979.

Anderson, D. E., R. R. Meier, and J. B. Kumer, Improved model of Mie scattering contribution to tropospheric and stratospheric photodissociation fluxes, *Appl. Opt., 19*, 1230-1231, 1980.

Anthes, R. A., E.-Y. Hsie, and Y.-H. Kuo, Description of the Penn State/NCAR mesoscale model version 4 (MM4), *NCAR Tech. Note NCAR/TN-282+STR*, Natl. Cent. for Atmos. Res., Boulder, Colo., 1987.

Atherton, C. S., and J. E. Penner, The effects of biogenic hydrocarbons on the transformation of nitrogen oxides in the troposphere, *J. Geophys. Res., 95*, 14,027-14,038, 1990.

Atkinson, R., K. R. Darnall, A. C. Lloyd, A. M. Winer, and J. N. Pitts, Jr., Kinetics and mechanisms of the reaction of the hydroxyl radical with organic compounds in the gas phase, *Adv. Photochem., 11*, 375-488, 1979.

Atkinson, R., Kinetics and mechanisms of the gas-phase reactions of the hydroxyl radical with organic compounds under atmospheric conditions, *Chem. Rev., 85*, 69-201, 1985.

Atkinson, R., and A. C. Lloyd, Evaluation of kinetic and mechanistic data for modeling of photochemical smog, *J. Phys. Chem., 13*, 315-444, 1984.

Atkinson, R., A. C. Lloyd, and L. Winges, An updated chemical mechanism for hydrocarbon/NO_x/SO_2 photooxidations suitable for inclusion in atmospheric simulation models, *Atmos. Environ., 16*, 1341-1355, 1982.

Beck, S. M., et al., Operational overview of NASA GTE/CITE 1 airborne instrument intercomparisons: Carbon monoxide, nitric oxide, and hydroxyl instrumentation, *J. Geophys. Res., 92*, 1977-1985, 1987.

Blackadar, A. K., High resolution models of the planetary boundary layer, in *Advances in Environmental Science and Engineering*, vol. 1, edited by J. Pfafflin and E. Ziegler, pp. 50-85, Gordon and Breach, New York, 1979.

Blumenthal, D. L., J. A. McDonald, W. S. Keifer, J. B. Tommerdahl, M. L. Sager, and J. H. White, Three-dimensional pollutant distribution and mixing layer structure in the northeast U.S., Summary of the Sulfate Regional Experiment (SURE) aircraft measurements, *Atmos. Environ., 18*, 733-749, 1984.

Boatman, J. F., N. Laulainen, J. Ray, C. Van Valin, L. Gunter, R. Lee, D. Luecken, and K. Busness, Acid precursor concentrations above the northeastern United States during summer, 1987: Three case studies, *J. Geophys. Res., 95*, 11,831-11,846, 1990.

Brost, R. A., The sensitivity to input parameters of atmospheric concentrations simulated by a regional chemical-model, *J. Geophys. Res., 93*, 2371-2387, 1988.

Brost, R. A., P.L. Haagenson, and Y.-H. Kuo, Eulerian simulation of tracer distributions during CAPTEX, *J. Appl. Meteorol., 27*, 579-593, 1988.

Buhr, M. P., D. D. Parrish, R. B. Norton, F. C. Fehsenfeld, R. E. Sievers, and J. M. Roberts, Contribution of organic nitrates to the total reactive nitrogen budget at a rural eastern U.S. site, *J. Geophys. Res., 95*, 9808-9816, 1990.

Businger, J. A., J. C. Wyngaard, Y. Izumi, and E. F. Bradley, Flux-profile relationships in the atmospheric surface layer, *J. Atmos. Sci., 28*, 181-189, 1971.

Calvert, J. G., and S. Madronich, Theoretical study of the initial products of the atmospheric oxidation of hydrocarbons, *J. Geophys. Res., 92*, 2211-2220, 1987.

Cantrell, C. A., W. R. Stockwell, L. G. Anderson, K. L. Busarow, D. Perner, A. Schmeltekopf, J. G. Calvert, and H. S. Johnston, Kinetic study of the NO_3-CH_2O reaction and its possible role in nighttime tropospheric chemistry, *J. Phys. Chem., 89*, 139-146, 1985.

Carter, W. P. L., A. C. Lloyd, J. L. Sprung, and J. N. Pitts, Jr., Computer modeling of smog chamber data: Progress in validation of a detailed mechanism for the photooxidation of propane and *n*-butane in photochemical smog, *Int. J. Chem. Kinet., 11*, 45-101, 1979.

Chang, J. S., R. A. Brost, I. S. A. Isaksen, S. Madronich, P. Middleton, W. R. Stockwell, and C. J. Walcek, A three-dimensional Eulerian acid deposition model: Physical concepts and formulation, *J. Geophys. Res., 92*, 14,681-14,700, 1987.

Chatfield, R. B., and P. J. Crutzen, Sulfur dioxide in remote oceanic air: Cloud transport of reactive precursors, *J. Geophys. Res., 89*, 7111-7132, 1984.

Cox, R. A., A. E. J. Eggleton, R. G. Derwent, J. E. Lovelock, and D. E. Pack, Long-range transport of photochemical ozone in northwestern Europe, *Nature, 255*, 118-121, 1975.

Dlugokencky, E. J., and C. J. Howard, Studies of NO_3 radical reactions with some atmospheric organic compounds at low pressures, *J. Phys. Chem., 93*, 1091-1096, 1989.

Dodge, M. C., Effect of selected parameters on predictions of a photochemical model, *Rep. EPA-600/3-77-048*, U.S. Environ. Prot. Agency, Research Triangle Park, N.C., June 1977.

Drummond, J. W., D. H. Ehhalt, and A. Volz, Measurements of nitric oxide between 0-12 km altitude and 67°N to 60°S latitude obtained during STRATOZ III, *J. Geophys. Res., 93*, 15,831-15,849, 1988.

Dütsch, H. U., Vertical ozone distribution on a global scale, *Pure Appl. Geophys., 116*, 511-537, 1978.

Fahey, D. W., G. Hübler, D. D. Parrish, E. J. Williams, R. B. Norton, B. A. Ridley, H. B. Singh, S. C. Liu, and F. C. Fehsenfeld, Reactive nitrogen species in the troposphere: Measurements of NO, NO_2, HNO_3, particulate nitrate, peroxyacetyl nitrate (PAN), O_3, and total reactive odd nitrogen (NO_y) at Niwot Ridge, Colorado, *J. Geophys. Res., 91*, 9781-9793, 1986.

Fehsenfeld, F. C., M. J. Bollinger, S. C. Liu, D. D. Parrish, M. McFarland, M. Trainer, D. Kley, P. C. Murphy, D. L. Albritton, and D. H. Lenshow, A study of ozone in the Colorado mountains, *J. Atmos. Chem., 1*, 87-105, 1983.

Fehsenfeld, F. C., et al., A ground-based intercomparison of NO, NO_x, and NO_y measurement techniques, *J. Geophys. Res., 92*, 14,710-14,722, 1987.

Fehsenfeld, F. C., D. D. Parrish, and D. W. Fahey, The measurements of NO_x in the non-urban troposphere, in *Tropospheric Ozone*, edited by I. S. A. Isaksen, pp. 185-215, D. Reidel, Norwell, Mass., 1988.

Fishman, J., Vukovich, F. M., and E. V. Browell, The photochemistry of synoptic-scale ozone synthesis: Implications for the global tropospheric ozone budget, *J. Atmos. Chem., 3*, 299-320, 1985.

Fishman, J., V. Ramanathan, P. J. Crutzen, and S. C. Liu, Tropospheric ozone and climate, *Nature, 282*, 818-820, 1979*a*.

Fishman, J., S. Solomon, and P. J. Crutzen, Observations and theoretical evidence in support of a significant in-situ photochemical source of tropospheric ozone, *Tellus, 31*, 432-446, 1979*b*.

Geleyn, J. F., Some diagnostics of the cloud/radiation interaction in the ECMWF forecast model, in *Proceedings of Workshop on Radiation and Cloud-Radiation Interaction in Numerical Modeling*, pp. 135-162, European Centre for Medium Range Weather Forecasts, Reading, England, 1981.

Gery, M. W., G. Z. Whitten, J. P. Killus, and M. C. Dodge, A photochemical kinetics mechanism for urban and regional scale computer modeling, *J. Geophys. Res., 94*, 12,925-12,956, 1989.

Gidel, L., Cumulus cloud transport of transient tracers, *J. Geophys. Res., 88*, 6587-6599, 1983.

Gifford, F. A., Horizontal diffusion in the atmosphere: A Lagrangian-dynamical theory, *Atmos. Environ., 16*, 505-512, 1982.

Greenberg, J. P., and P. R. Zimmerman, Nonmethane hydrocarbons in

remote tropical, continental, and marine atmospheres, *J. Geophys. Res., 89*, 4767-4778, 1984.

Guicherit, R., and H. VanDop, Photochemical production of ozone in Western Europe (1971-1978) and its relation to meteorology, *Atmos. Environ., 11*, 145-155, 1977.

Hall, I. W., R. P. Wayne, R. A. Cox, M. E. Jenkin, and G. D. Hayman, Kinetics of the reaction of NO_3 with HO_2, *J. Phys. Chem., 92*, 5049-5054, 1988.

Haltiner, G. J., *Numerical Weather Prediction*, 317 pp., John Wiley, New York, 1971.

Heck, W. W., O. C. Taylor, R. Adams, G. Bingham, J. Miller, E. Preston, and L. Weinstein, Assessment of crop loss from ozone, *J. Air Pollut. Control Assoc., 32*, 353-356, 1982.

Hesstvedt, E., O. Hov, and I. S. A. Isaksen, Quasi-steady-state approximations in air pollution modeling: Comparison of two numerical schemes for oxidant prediction, *Int. J. Chem. Kinet., 10*, 971-994, 1978.

Hov, O., A one-dimension vertical model for ozone and other gases in the atmospheric boundary layer, *Atmos. Environ., 17*, 535-549, 1983.

Hov, O., and R. G. Derwent, Sensitivity studies of the effects of model formulation on the evaluation of control strategies for photochemical air pollution formation in the United Kingdom, *J. Air Pollut. Control Assoc., 31*, 1260-1267, 1981.

Hsie, E.-Y., R. A. Anthes, and D. Keyser, Numerical-simulation of frontogenesis in a moist atmosphere, *J. Atmos. Sci., 41*, 2581-2594, 1984.

Jacob, D. J., and S. C. Wofsy, Photochemistry of biogenic emissions over the Amazon forest, *J. Geophys. Res., 93*, 1477-1486, 1988.

Jet Propulsion Laboratory (JPL), Chemical kinetics and photochemical data for use in stratospheric modeling, Evaluation 8, *JPL Publication 87-41*, 196 pp., NASA, Pasadena, Calif., 1987.

Kelly, N.A., G. T. Wolff, and M. A. Ferman, Sources and sinks of ozone in rural areas, *Atmos. Environ., 18*, 1251-1266, 1984.

Kelly, T. J., R. L. Tanner, L. Newman, P. J. Galvin, and J. A. Kadlecek, Trace gas and aerosol measurements at a remote site in the northeast U. S., *Atmos. Environ., 18*, 2565-2576, 1984.

Killus, J. P., and G. Z. Whitten, Isoprene: A photochemical kinetic mechanism, *Environ. Sci. Technol., 18*, 142-148, 1984.

Kleinman, L. I., Photochemical formation of peroxides in the boundary layer, *J. Geophys. Res., 91*, 10,889-10,904, 1986.

Ko, M. K. W., K. K. Tung, D. K. Weisenstein, and N. D. Sze, A zonal mean model of stratospheric tracer transport in isentropic coordinates: Numerical simulations for nitrous oxide and nitric acid, *J. Geophys. Res., 90*, 2313-2329, 1985.

Lamb, B., A. Guenther, D. Gay, and H. Westberg, A national inventory of biogenic emissions, *Atmos. Environ., 21*, 1695-1705, 1987.

Lamb, R. G., A regional scale (1000 km) model of photochemical air pollution, 1, Theoretical foundation, *Rep. EPA-600/3-83-025*, U.S. Environ. Prot. Agency, Research Triangle Park, N. C., 1983.

Lamb, R. G., Diagnostic studies of ozone in the northeastern United States based on application of the regional oxidant model (ROM), in *The Scientific and Technical Issues Facing Post-1987 Ozone Control Strategies*, edited by G. T. Wolff, J. L. Hanisch, and K. Schere, pp. 239-256, Air & Waste Manag. Assoc., Pittsburgh, Pa., 1988.

Lelieveld, J., and P. J. Crutzen, Influence of cloud photochemical processes on tropospheric ozone, *Nature, 343*, 227-233, 1990.

Levy, H., II, Normal atmosphere: Large radical and formaldehyde concentrations predicted, *Science, 173*, 141-143, 1971.

Lin, X., M. Trainer, and S. C. Liu, On the nonlinearity of tropospheric ozone production, *J. Geophys. Res., 93*, 15,879-15,888, 1988.

Liu, M. K., R. E. Morris, and J. P. Killus, Development of a regional oxidant model and application to the northeastern United States, *Atmos. Environ., 18*, 1145-1161, 1984.

Liu, S. C., Possible effects on tropospheric O_3 and OH due to NO emissions, *Geophys. Res. Lett., 4*, 325-328, 1977.

Liu, S. C., D. Kley, M. McFarland, J. D. Mahlman, and H. Levy II, On the origin of tropospheric ozone, *J. Geophys Res., 85*, 7546-7552, 1980.

Liu, S. C., J. R. McAfee, and R. J. Cicerone, Radon 222 and tropospheric vertical transport, *J. Geophys. Res., 89*, 7291-7297, 1984.

Liu, S. C., M. Trainer, F. C. Fehsenfeld, D. D. Parrish, E. J. Williams, D. W. Fahey, G. Hübler, and P. C. Murphy, Ozone production in the rural troposphere and the implications for regional and global ozone distributions, *J. Geophys. Res., 92*, 4191-4207, 1987.

Lloyd, A. C., R. Atkinson, F. W. Lurmann, and B. Nitta, Modeling potential ozone impacts from natural hydrocarbons, 1, Development and testing of a chemical mechanism for the NO_x-air photooxidations of isopreneand α-pinene under ambient conditions, *Atmos. Environ., 17*, 1931-1950, 1983.

Logan, J. A., Nitrogen oxides in the troposphere: Global and regional budgets, *J. Geophys. Res., 88*, 10,785-10,807, 1983.

Logan, J. A., Ozone in rural areas of the United States, *J. Geophys. Res., 94*, 8511-8532, 1989.

Logan, J. A., M. J. Prather, S. C. Wofsy, and M. B. McElroy, Tropospheric chemistry: A global perspective, *J. Geophys. Res., 86*, 7210-7254, 1981.

Louis, J. F., A two-dimensional transport model of the atmosphere, Ph.D. thesis, 150 pp., Univ. of Colo., Boulder, 1974.

Lurmann, F. W., A. C. Lloyd, and R. Atkinson, A chemical mechanism for use in long-range transport/acid deposition computer modeling, *J. Geophys. Res., 91*, 10,905-10,936, 1986.

McNeal, R. J., J. P. Mugler, Jr., R. C. Harris, and J. M. Hoell, Jr., NASA Global Tropospheric Experiment, *Eos Trans. AGU, 64*, 561-562, 1983.

McRae, G. J., W. R. Goodin, and J. H. Seinfeld, Numerical solution of the atmospheric diffusion equation for chemically reacting flows, *J. Comput. Phys., 45*, 1-42, 1982.

Moortgat, G. K., R. A. Cox, G. Schuster, J. P. Burrows, and G. S. Tyndall, Peroxy radical reactions in the photo-oxidation of CH_3CHO, *J. Chem. Soc. Faraday Trans. 2, 85*, 809-829, 1989*a*.

Moortgat, G. K., B. Veyret, and R. Lesclaux, Kinetics of the reaction of HO_2 with $CH_3C(O)O_2$ in the temperature range 253. K-368. K, *Chem. Phys. Lett., 160*, 443-447, 1989*b*.

Morris, R., S. Reynolds, M. Yocke, and M.-K. Liu, The System Applications, Inc. regional transport model–current status and future needs, in *The Scientific and Technical Issues Facing Post-1987 Ozone Control Strategies*, edited by G. T. Wolff, J. L. Hanisch, and K. Schere, pp. 257-287, Air & Waste Manag. Assoc., Pittsburgh, Pa., 1988.

Mozurkewich, M., and J. G. Calvert, Reaction probability of N_2O_5 on aqueous aerosols, *J. Geophys. Res., 93*, 15,889-15,896, 1988.

Mueller, P. K., and G. M. Hidy, The Sulfate Regional Experiment: Report of findings, *Rep. EA-1901*, 3 vols., 395 pp., Elect. Power Res. Inst., Palo Alto, Calif., 1983.

Mueller, P. K., and J. G. Watson, Eastern regional air quality measurements, *Rep. EA-1914*, vol. 1, 192 pp., Elect. Power Res. Inst., Palo Alto, Calif., 1982.

National Academy of Sciences (NAS), Ozone and other photochemical oxidants, report, Washington, D. C., 1977.

Parrish, D. D., B. Huebert, R. B. Norton, M. J. Bollinger, S. C. Liu, P. C. Murphy, D. L. Albritton, and F. C. Fehsenfeld, Measurements of HNO_3 and NO_3^- particulates at a rural site in the Colorado mountains, *J. Geophys. Res., 91*, 5379-5393, 1986.

Perner, D., U. Platt, M. Trainer, G. Hübler, J. Drummond, W. Junkermann, J. Rudolph, B. Shubert, and A. Volz, Measurements of tropospheric OH concentrations: A comparison of field data with model predictions, *J. Atmos. Chem., 5*, 185-216, 1987.

Pickering, K. E., R. R. Dickerson, G. J. Huffman, J. F. Boatman, and A. Schanot, Trace gas transport in the vicinity of frontal convective clouds, *J. Geophys. Res., 93*, 759-773, 1988.

Rasmussen, R. A., R. B. Chatfield, and M. W. Holdren, Hydrocarbon species in rural Missouri air, Wash. State Univ., Pullman, 1977.

Reich, P. B., and R. G. Amundson, Ambient levels of ozone reduce net photosynthesis in tree and crop species, *Science, 230*, 566-570, 1985.

Research Triangle Institute, Investigation of rural oxidant levels as related to urban hydrocarbon control strategies, *Rep. EPA-450/3-75-036*, 352 pp., Research Triangle Park, N. C., 1975.

Roberts, J. M., The atmospheric chemistry of organic nitrates, *Atmos. Environ., Part A, 24*(2), 243-287, 1990.

Rood, R. B., Numerical advection algorithms and their role in atmospheric transport and chemistry models, *Rev. Geophys., 25*, 71-100, 1987.

Schere, K. L., Modeling ozone concentrations, *Environ. Sci. Technol., 22*, 488-495, 1988.

Schere, K. L., and R. A. Wayland, EPA regional oxidant model (ROM2.0): Evaluation on 1980 NEROS data bases, *Rep. EPA-600/3-89/057*, 370 pp., U.S. Environ. Prot. Agency, Research Triangle Park, N. C., 1989.

Seila, R. L., R. R. Arnts and J. W. Buchanan, Atmospheric volatile hydrocarbon composition at five remote sites in northwestern North Carolina, in *APCA-Specialty Conference: Transactions of. Environmental Impact of Natural Emissions*, edited by V. P. Aneja, pp. 125-140, Air Poll. Control Assoc., Pittsburg, Pa., 1984.

Seinfeld, J. H., Ozone air quality models: A critical review, *J. Air Pollut. Control Assoc., 38*, 616-620, 1988.

Sexton, K., and H. Westberg, Nonmethane hydrocarbon composition of urban and rural atmospheres, *Atmos. Environ., 18*, 1125-1132, 1984.

Sillman, S., J. A. Logan, and S. C. Wofsy, A regional scale model for ozone in the United States with sub-grid representation of urban power plant plumes, *J. Geophys. Res., 95*, 5731-5748, 1990.

Singh, H. B., J.R. Martinez, D. G. Hendry, R. J. Jaffe, and W. B. Johnson, Assessment of the oxidant-forming potential of light saturated hydrocarbons in the atmosphere, *Environ. Sci. Technol., 15*, 113-119, 1981.

Smagorinsky, J., S. Manabe, and J. L. Holloway, Jr., Numerical results from a nine-level general circulation model of the atmosphere, *Mon. Weather Rev., 93*, 727-768, 1965.

Smolarkiewicz, P. K., A simple positive definite advection scheme with small implicit diffusion, *Mon. Weather Rev., 111*, 479-486, 1983.

Smolarkiewicz, P. K., A fully multidimensional positive advection transport algorithm with small implicit diffusion, *J. Comput. Phys., 54*, 325-362, 1984.

Stockwell, W. R., A homogeneous gas phase mechanism for use in a regional acid deposition model, *Atmos. Environ., 20*, 1615-1632, 1986.

Trainer, M., E.-Y. Hsie, S. A. McKeen, R. K. Tallamraju, D. D. Parrish, F. C. Fehsenfeld, and S. C. Liu, Impact of natural hydrocarbons on hydroxyl and peroxy radicals at a remote site, *J. Geophys. Res., 92*, 11,879-11,894, 1987*a*.

Trainer, M., E. J. Williams, D. D. Parrish, M. P. Buhr, E. J. Allwine, H. H. Westberg, F. C. Fehsenfeld, and S. C. Liu, Models and observations of the impact of natural hydrocarbons on rural ozone, *Nature, 329*, 705-707, 1987*b*.

Turco, R. P., O. B. Toon, P. Hamill, and R. C. Whitten, Effects of meteoric debris on stratospheric aerosols and gases, *J. Geophys. Res., 86*, 1113-1128, 1981

U.S. Environmental Protection Agency (EPA), AIRS (Aeronometric Information Retrieval Systems) Users guide, volume 1 (of 7), internal report, National Air Data Branch, Research Triangle Park, N. C., Dec., 1987.

U. S. EPA, The 1985 NAPAP emissions inventory (version 2): Development of the annual data and modelers' tapes, *Rep. EPA-600/7-89-012a*, 692 pp., Natl. Tech. Info. Serv., Springfield, Va., 1989.

Vukovich, F. M., W. D. Bach, Jr., B. W. Crissman, and W. J. King, On the relationship between high ozone in the rural surface layer and high pressure systems, *Atmos. Environ., 11*, 967-983, 1977.

Wallington, T. J., R. Atkinson, and A. M. Winer, Rate constant for the gas phase reaction of OH radicals with peroxyacetyl nitrate (PAN) at 273 and 297 K, *Geophys. Res. Lett., 11*, 861-864, 1984.

Wang, W.-C., and N. D. Sze, Coupled effects of atmospheric N_2O and O_3 on the Earth's climate, *Nature, 268*, 589-590, 1980.

Weinstock, B., and H. Niki, The carbon-monoxide balance in nature, *Science, 176*, 290, 1972.

Wesley, M. L., and B. B. Hicks, Some factors that affect the deposition rates of sulfur dioxide and similar gases on vegetation, *J. Air Pollut. Control Assoc., 27*, 1110-1116, 1977.

Westberg, H. H., K. J. Allwine, and E. Robinson, Measurement of light hydrocarbons and studies of oxidant transport beyond urban areas, in 1974 Lawrenceville Study, contract 68-02-1232, Wash. State Univ., Pullman, 1975.

Whitby, K. T., The physical characteristics of sulfur aerosols, *Atmos. Environ., 12*, 135-159, 1978.

Williams, E. J., D. D. Parrish, and F. C. Fehsenfeld, Determination of nitrogen-oxide emissions from soils–Results from a grassland in Colorado, United States, *J. Geophys. Res., 92*, 2173-2179, 1987.

Williams, E. J., D. D. Parrish, M. P. Buhr, F. C. Fehsenfeld, and R. Fall, Measurements of soil NO_x emissions in central Pennsylvania, *J. Geophys. Res., 93*, 9539-9546, 1988.

Winer, A. M., J. W. Peters, J. P. Smith, and J. N. Pitts, Response of commercial chemiluminescent NO-NO_2 analyzers to other nitrogen containing compounds, *Environ. Sci. Technol., 8*, 1118-1121, 1974.

World Meteorological Organization (WMO) and NASA, Atmospheric Ozone 1985, Assessment of our understanding of the processes controlling its present distribution and change, *Rep. 16*, Global Ozone Res. and Monit. Proj., Geneva, 1986.

Wofsy, S. C., J. C. McConnell, and M. B. McElroy, Atmospheric CH_4, CO and CO_2, *J. Geophys. Res., 77*, 447, 1972.

Zhang, D., and R. A. Anthes, A high resolution model of the planetary boundary layer–sensitivity tests and comparisons with SESAME-79 data, *J. Appl. Meteorol., 21*, 1594-1609, 1982.

E.-Y. Hsie, S. C. Liu, S. A. McKeen, R. Tallamraju, and M. Trainer, Aeronomy Laboratory, Environmental Research Laboratories, NOAA, 325 Broadway, Boulder, CO 80303.

(Received March 15, 1990;
revised December 31, 1990;
accepted January 2, 1991.)